Development of enhanced multi-spot structured illumination microscopy with fluorescence difference

EDWARD NICHOLAS WARD

Development of enhanced multi-spot structured illumination microscopy with fluorescence difference

Edward N. Ward

Abstract

This project sets out to design and construct a novel super-resolution technique for biological imaging: enhanced multi-focal structured illumination microscopy; merging the fields of structured-illumination and point-spread function engineering. Computer simulations demonstrate the theoretical potential of this technique and suggest at least 1.4 times increase over existing structured illumination methods.

Building on this, new pattern projection techniques based on holography are developed to project the required illumination patterns over an extended field of view. In addition, new techniques based on graphical-processor unit programming are developed for the post-processing and reconstruction of multi-focal structured illumination data.

Finally, these techniques are tested in the imaging of a range of biological structures in both living and fixed cells. While the holographic projection and post-processing techniques proved successful, the gains achieved with enhanced multi-focal structured illumination microscopy were limited. While there is a measured gain in resolution – and a potential improvement in depth sectioning – these advantages are not apparent on all structures. Finally, the relative merits of the techniques over existing methods are discussed and potential future directions are suggested.

Declaration

The work described herein was undertaken at the Department of Chemistry, Durham University, between September 2015 and November 2018. All of the work is my own, except where specifically stated otherwise. No part has previously been submitted for a degree at this or any other university.

Statement of copyright

Contents

List of figures and tables

Abbreviations used

AO:	Adaptive Optics
APD:	Avalanche Photo-Diode
CCD:	Charge Coupled Device
CMOS:	Complementary Metal–Oxide Semiconductor
CPU:	Computer Processing Unit
CW:	Continuous Wave
DAQ:	Data Acquisition
DM:	Deformable Mirror
DMD:	Digital Micromirror Device
DS:	Direct Search
dSTORM:	direct Stochastic Optical Reconstruction Microscopy
EMCCD:	Electron Multiplying Charge Coupled Device
eMSIM:	enhanced Multi-spot Structured Illumination Microscopy
FFT:	Fast Fourier Transform
FOV:	Field of View
FRC:	Fourier Ring Correlation
FWHMa:	Full-Width Half-Maxima
FWHMi:	Full-Width Half-Minima
GAA:	Gerchberg Saxton with Adaptive Additive
GFP:	Green Fluorescent Protein
GPU:	Graphical Processing Unit
GS:	Gerchberg Saxton
GUI:	Graphical User Interface
IFTA:	Iterative Fourier Transform Algorithm
ISM:	Image Scanning Microscopy
IVR:	Intramolecular Vibrational Relaxation
JRL:	Joint Richardson-Lucy
LC:	Liquid Crystal
LSCM:	Laser Scanning Confocal Microscopy
MLE:	Maximum Likelihood Estimation
MRAF:	Mixed Region Amplitude Freedom
MSIM:	Multi-spot Structured Illumination Microscopy

MTG:	Mito-Tracker Green
NA:	Numerical Aperture
OTF:	Optical Transfer Function
PA-GFP:	Photo-Activatable Green Fluorescent Protein
PALM:	Photo-Activated Localisation Microscopy
PBS:	Phosphate-Buffered Solution
PIFP:	Pattern-Illuminated Fourier Ptychography
PMT:	Photo-Multiplier Tube
PSF:	Point-Spread Function
PSIM:	Plasmonic Structured Illumination Microscopy
RESOLFT:	Reversible Saturable Optical Fluorescence Transitions
SIM:	Structured Illumination Microscopy
SLAM:	Switching Laser Mode Microscopy
SLM:	Spatial Light Modulator
SMLM:	Single-Molecule Localisation Microscopy
SNR:	Signal to Noise Ratio
SSIM:	Saturated Structured Illumination Microscopy
STED:	Stimulated Emission Depletion
STORM:	Stochastic Optical Reconstruction Microscopy
SWFM:	Standing Wave Fluorescence Microscopy
TEM_{00}	zero-order Transverse Electromagnetic Mode

Acknowledgements

Firstly, I would like to thank my wonderful supervisor Robert Pal and his family, whose support and friendship made all of this work possible. I would also like to thank Andrew Beeby and Lars Palssön for their help throughout this work, and Roy Quinlan whose guidance through my master's degree was invaluable.

Thanks also go to the amazing workshop team's Bryan Denton, Kelvin Appleby, Omer Ekinoglu, Neil Holmes and Paul White, whose technical skills and help in the design and construction was vital.

I would also like to thank all the members of 078 throughout the years: George, Abbie, Holly, Daniel, Ian, Frida, Hannah, Bhavini, Jamie, Sam, Kathleen and Lewis for making every day in the lab a joy.

A special thanks goes to my friends Alex, Ben and all of the Joyce-Gibbons family who made my weekends and evenings out of the lab so great.

I would like to thank my family, Alison, Tom and Amelia for helping to get me to where I am now.

Finally, I would especially like to thank my wonderful wife, Keita, who has helped me every step of the way and made every day worthwhile.

1. Optical microscopy

Summary: *this chapter aims to offer an introduction to the field of optical microscopy to provide a context for the work completed throughout the project. It will cover the background and history of the field and describe the issue of the diffraction limit in biological imaging. The most popular existing super-resolution methods will also be described to provide a motivation for the work completed.*

1.1 Introduction

Since the invention of the first compound light microscope almost 400 years ago, the general design has changed very little.[1] At its heart, every microscope consists of two key lenses: a powerful objective lens responsible for the majority of the magnification, and a tube or eyepiece lens that focuses the magnified image into the eye or onto an imaging camera. The distance between these two lenses is kept relatively constant, and the focus is altered by changing the distance between the sample and the objective lens. While modern microscopes achieve high magnification using complex compound objective lenses, the basic principle remains the same.

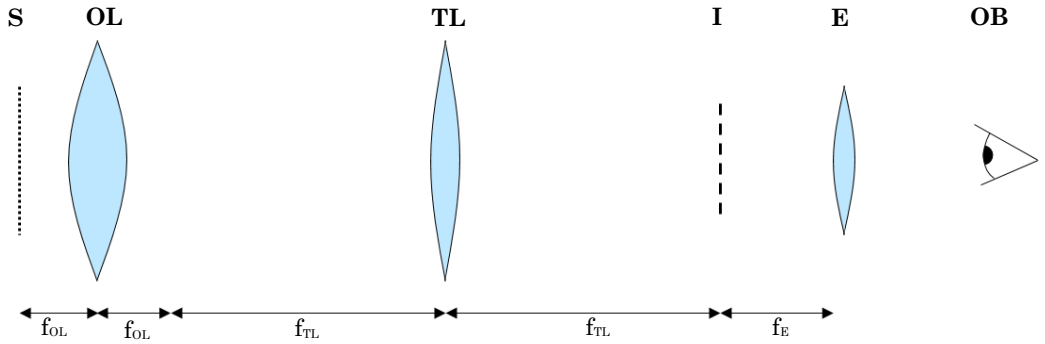

Figure 1.1: Optical diagram for a simple light microscope.

A sample, **S**, is placed at a distance f_{OL} from the objective lens, **OL**. A tube lens, **TL**, is then placed at a distance $f_{OL} + f_{TL}$ from the objective lens. A magnified image of the sample is generated at the conjugate image plane, **I**. If the sample is being imaged using a camera, the sensor is placed at this plane. If the sample is to be viewed by an observer **OB**, then an eyepiece lens is placed a distance f_E from the image plane. f_{OL}, f_{TL} and f_E denote the focal lengths of the objective, tube and eyepiece lenses respectively.

1.1.1 Fluorescence microscopy

Possibly the most significant advancement in optical microscopy was the introduction of fluorescent probes for use as labels in biological imaging. In the early 1940s, fluorescent stains for biological tissues first appeared,[2] and by the 1990s, the first genetically modified fluorescent proteins were being used as protein tags.[3] Figure 1.3 shows the process of fluorescent excitation and emission. By illuminating the sample with higher energy, shorter wavelength photons, electrons in the fluorescent molecules absorb this energy and move into an excited singlet state.

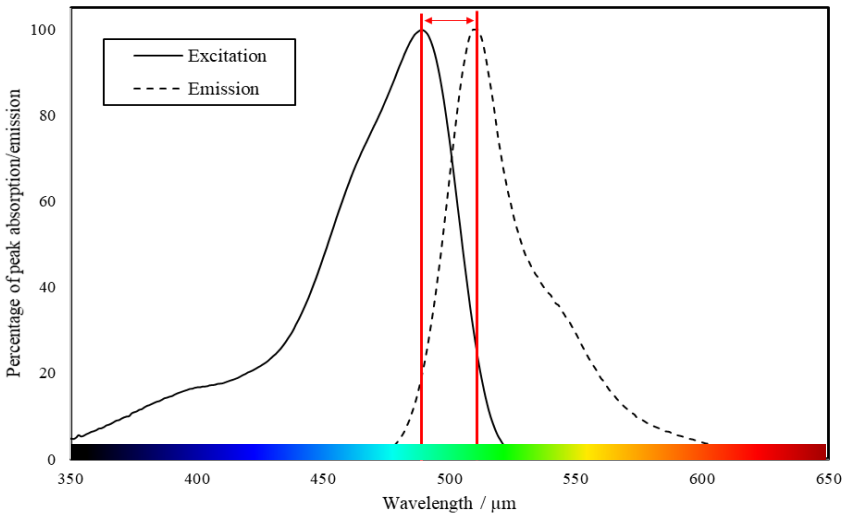

Figure 1.2: Absorption-emission spectra for green fluorescent protein.

The solid line indicates the absorption spectra, a measure of how well the fluorophore will be excited by any particular excitation wavelength. The dashed line indicates the emission spectra which describes the typical range of wavelengths emitted. The Stokes' shift, indicated by the red lines is a measure of the shift between the excitation and emission. Typically, larger Stokes' shifts are preferable when selecting a fluorophore as separating the emitted signal from scattered excitation light is easier.

After undergoing Intramolecular Vibrational Relaxation (IVR) within the excited singlet state, they then transition back into the ground state, emitting the energy as longer wavelength light. The difference between the wavelengths of the light absorbed and emitted is termed the Stokes shift (see figure 1.2). Since biological structures often lack strong innate

fluorescence (autofluorescence) at visible excitation wavelengths, fluorescent stains can be easily distinguished in the sample.

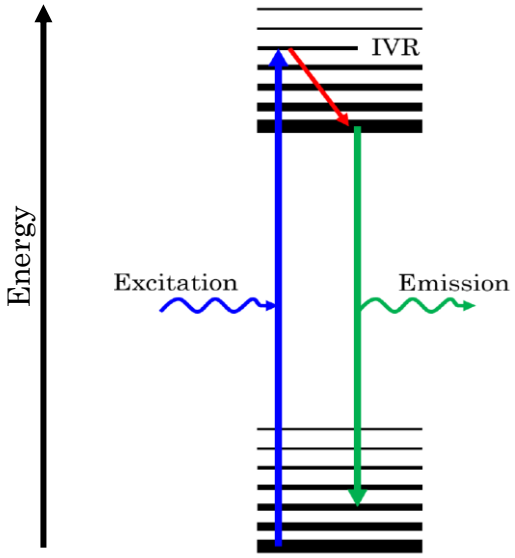

Figure 1.3: Jablonski diagram.

Jablonski diagram showing energy transitions in fluorescent molecules. Under linear excitation (blue line), the fluorophore moves to an excited singlet state, before undergoing intramolecular vibrational relaxation (IVR) to a lower energy level (red line). From there, it can then emit light of a longer wavelength through fluorescence (green line).

This means that by labelling specific structures with fluorescent probes, their localisation and movement can be easily measured in a sample even if they may be obscured when using traditional light microscopy. This is demonstrated in figure 1.4 where the mitochondrial network can be more easily distinguished that in brightfield, transmitted-light microscopy.

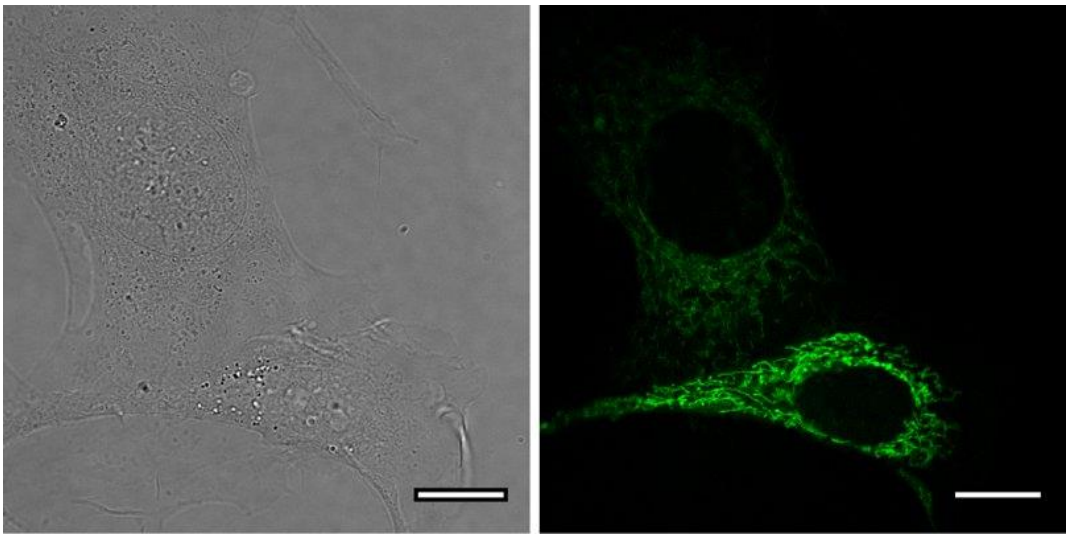

Figure 1.4: Comparison of bright-field and fluorescence microscopy.

Left: mouse fibroblast cells imaged under brightfield microscopy. While many of the features of the cell are visible, the fine structures of the cell are obscured. Right: fluorescence imaging of the mitochondria, which have been stained with a fluorescent dye. While other features of the cell are now not visible, the fine structure of the mitochondrial network can now be studied. Cells were fluorescently labelled with mito-tracker green and excited with 488 nm excitation light and emission collected from 500-550 nm. Scale bar is 15 μm. Images courtesy of Robert Pal.

Since every fluorophore has a unique excitation and emission profile, it is also possible to use multiple fluorophores simultaneously. To achieve this, each fluorophore is excited by a specific wavelength, generated using band-pass filters or laser lines. The signal from the different fluorophores are separated using a combination of long-pass filters and dichroic mirrors. For biological imaging, this multicolour labelling allows for different structures to be distinguished and imaged simultaneously. Figure 1.5 shows an example of multicolour labelling where the cell nucleus, mitochondria and actin cytoskeleton are all independently labelled. The versatility of fluorescence microscopy and ongoing advancements in labelling and imaging has made optical microscopy an exceptionally powerful tool for

biologists.

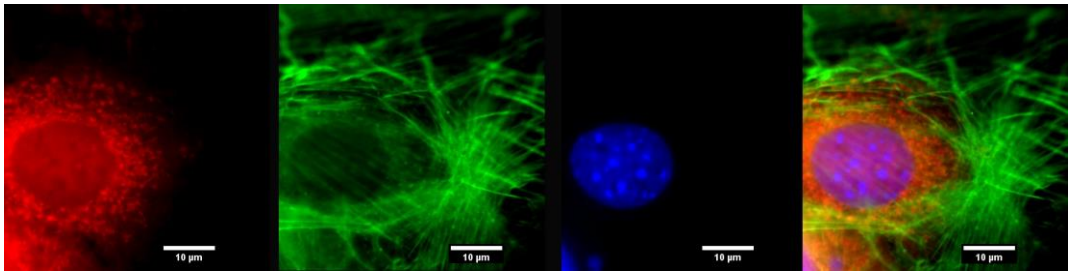

Figure 1.5: Example of multicolour labelling in biological imaging.

Mouse fibroblast cells stained simultaneously with three common fluorescent dyes. Images were taken under widefield illumination with a mercury discharge lamp. Scale bar is 10μm. Far left: The red dye, Mito-tracker red, which selectively binds to the mitochondria. Centre left: The green dye Alexa-fluor 488 phalloidin attached to the plant toxin phalloidin which selectively binds filamentous actin. Centre right: The blue dye, DAPI, which stains DNA in the cell nucleus. Far right: Merged colour image. Merging the individual colours in one picture allows for simple analysis of the relative positions and interactions of the structures in the cell.

The rise of fluorescence microscopy was aided by the development of Laser Scanning Confocal Microscopy (LSCM).[4] In addition, as one of the most popular tools I fluorescence imaging, LSCM has come to be a benchmark technique for comparison of other imaging modalities.

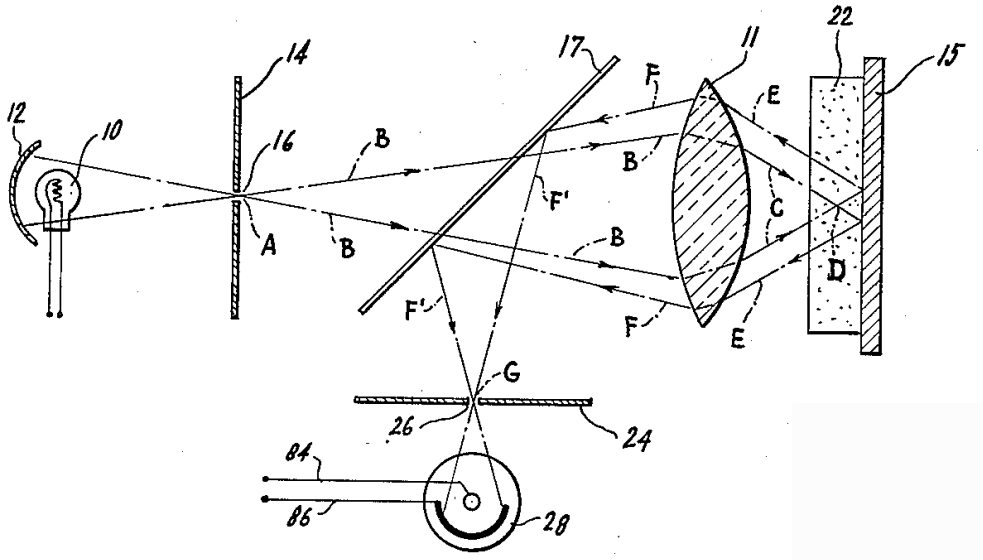

Figure 1.6: Original diagram from the patent of the first microscope.

Section of a figure for Marvin Minsky's original patent for the confocal imaging setup.[4] A light source (18) is focused to a point in the sample (15). Fluorescence from this point is focused through a pinhole (26) and onto a point detector (28). In this setup the sample image is built up by scanning the sample across the focal point and measuring the signal at each position.

LSCM generates an image by using a single point detector to measure the intensity of each pixel in the image sequentially. A pair of synchronised galvanometric mirrors raster scans a diffraction-limited spot laterally across the region of interest. In the first confocal setup, (figure 1.6) a pinhole was placed in front of an incoherent source to provide the illumination. In modern systems, the excitation source used is often a coherent laser as this provides very narrow excitation bandwidths, permitting highly selective fluorescent excitation. The light collected from the excitation spot is the collected through the objective lens and the signal is recorded using a pointilistic detector. The pointillistic detectors (shown in figure 1.8) are usually either a Photon Multiplier Tube (PMT) or Avalanche Photo-Diode (APD), though hybrid detectors, which combine the two technologies into a single detector, are becoming increasingly popular.[5] The confocality of LSCM comes from the use of a pinhole in the detection arm of the optical pathway to provide improved optical sectioning. Light gathered from the illuminated pixel is focused to a point

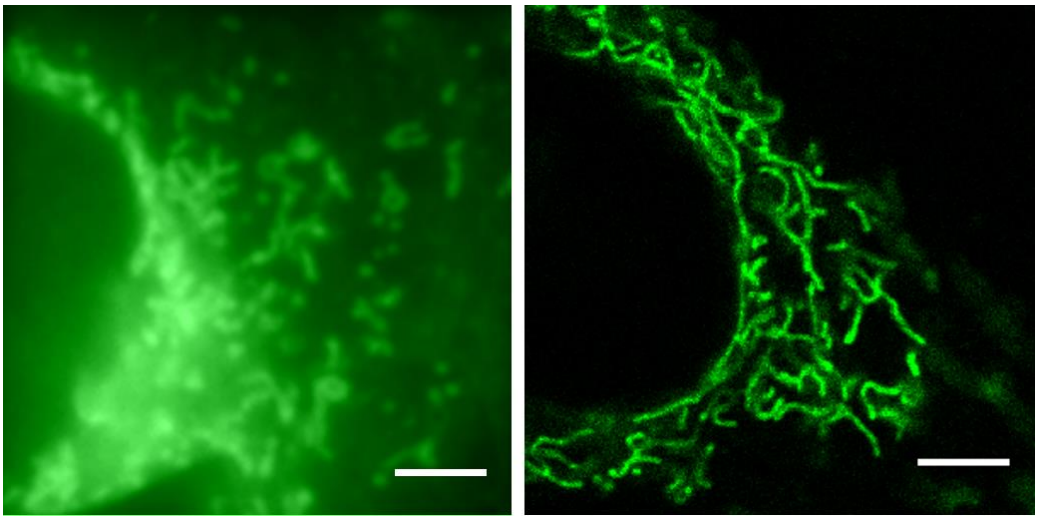

Figure 1.7: Comparison of widefield and confocal imaging.

False-colour images of mouse fibroblast cells imaged with green-fluorescent labelled mitochondria Left: Widefield image. Right: Confocal image. The advantage of confocal imaging is apparent in the clarity of the image as only a small slice through the sample is being image. The difference is particularly noticeable in the region to the left of the image where there is a significant number of labelled mitochondria above and below the focal plane. Mitochondria were stained with mito-tracker green and excited with 488 nm light. Widefield emission was collected after 510 nm long-pass filter. Confocal emission was collected over 500 nm to 550 nm. Scale bar 5 μm. Confocal image courtesy of Robert Pal.

after the scan mirrors. Only light from the focal plane of the objective will focus through the pinhole, excluding light from outside the focal plane. The advantage of this can be seen in figure 1.7, comparing the similar regions of a sample imaged with widefield and confocal microscopes. This means that the pixel imaged represents a 3D volume (voxel), making each image equivalent to a thin section through the sample. By acquiring many images at different known axial heights, 3D maps of the structures can be reconstructed from the stacks of images.

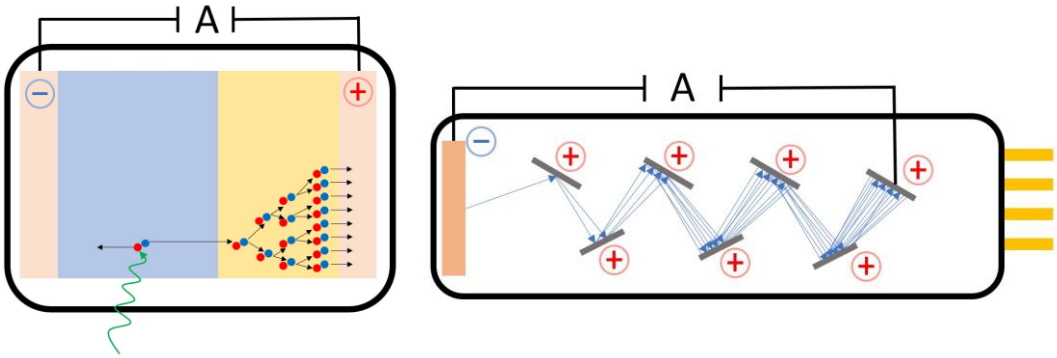

Figure 1.8: Diagrams showing PMT and APD.

Left: APD. Light incidents on a semi-conductor layer generating an electron-hole pair. The electron is accelerated towards another semi-conductor layer, the avalanche region (yellow) by a high voltage applied across the APD. Once in the avalanche region it goes on to generate more pairs in a cascade. The signal is generated when the electrons reach the anode and is measured as a current through A. Right: PMT. Light incidents on a photocathode (orange) generating a photo-electron (blue arrow). The electron is accelerated down the tube by a high voltage across the tube, indenting on a series of dynodes (grey). At each dynode, more photo-electrons are released and accelerated down the tube, amplifying the current. The final signal is measured as a current through A

1.1.2 The diffraction barrier

The resolution of optical microscopy is fundamentally limited by the diffraction limit of light. There are several available methods to describe the resolution of an imaging system, with different criteria being used in different fields. Under the assumption of imaging with a circular aperture (i.e. a circular lens) there are three principle criteria to define the resolution limit: the Rayleigh criterion; the Sparrow criterion; and the Abbe criterion. Figure 1.8 shows an example of the diffraction limit when imaging two point sources. Numerically the values for the diffraction limit can be calculated from the wavelength of the imaged light and the Numerical Aperture (NA) of the imaging lens; a measure of the amount of a light the lens can gather from the source (shown in figure 1.9).

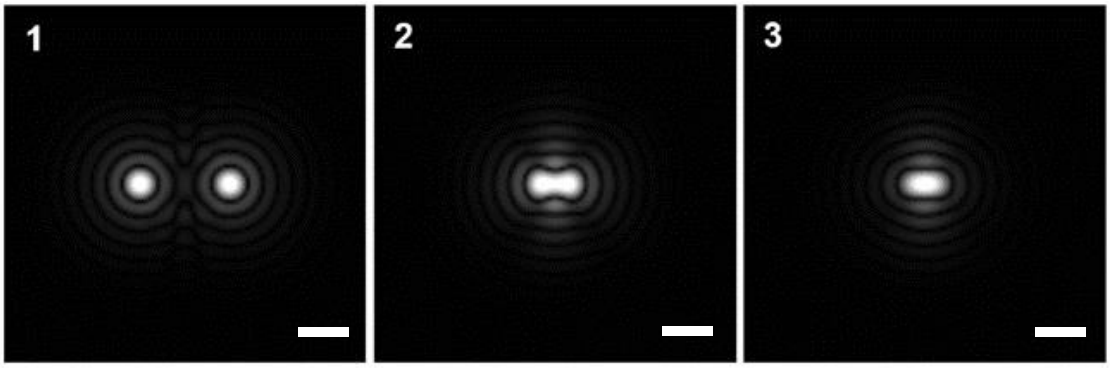

Figure 1.9: Definition of the resolution limit.

Resolution limits in optical microscopy. PSFs were calculated for an emission wavelength of 532 *nm* and an imaging lens with NA = 1.2. Scale bar is 800 *nm*. **1**: Two well-resolved point sources. **2**: Two point sources at the resolution limit as defined by the Raleigh criterion. **3**: Two point sources at the resolution limit of the Sparrow criteria

The Rayleigh criterion defines the resolution limit as the minimal distance between two point sources before the first minima of one imaged point source overlaps with the maxima of the second point source. For the lateral resolution this can be calculated as:

$$d_{x,y} = 0.6\frac{\lambda}{\mathrm{NA}}, \qquad \text{Eq. 1.1}$$

and in the axial direction as:

$$d_z = \frac{2\lambda n}{\mathrm{NA}^2} \qquad \text{Eq. 1.2}$$

where λ is the imaged wavelength and n is the refractive index of the imaging medium. The NA of the imaging system is defined as:

$$\mathrm{NA} = n \cdot \sin(\theta)\,, \qquad \text{Eq. 1.3}$$

where, again, n is the refractive index and θ is the half-angle of the cone of light that can be accepted by the lens (see figure 1.10).

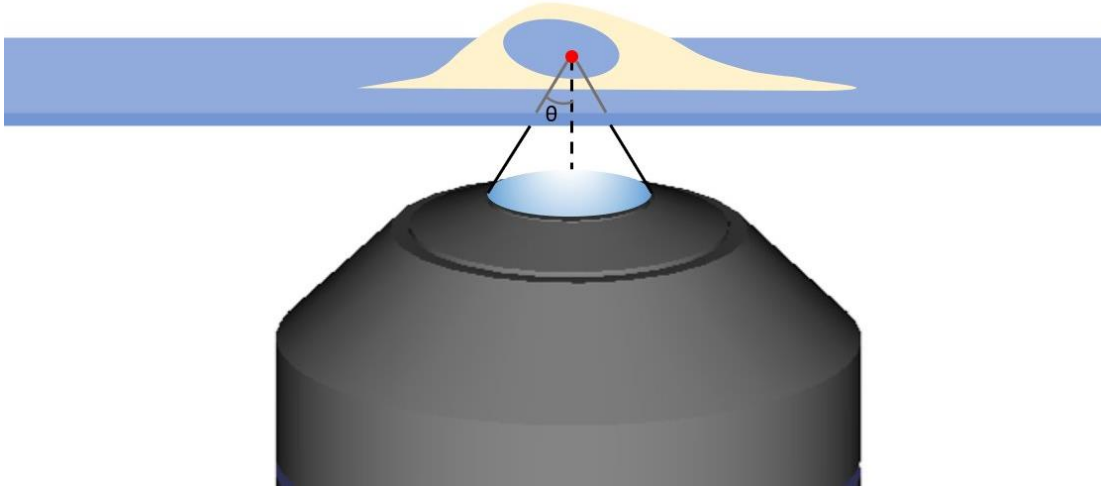

Figure 1.10: Half-angle of an oil-immersion objective.

The half-angle, θ, is half the angle of the maximum cone of light that can be collected by an imaging lens from a point in the sample.

The Sparrow criterion is narrower than the Rayleigh criterion and defines two point sources as resolved if there is intensity variation between the two maxima. Figure 1.9 shows two point sources at the limit of the Sparrow criterion which in the lateral direction is calculated as:

$$d_{x,y} = 0.47\frac{\lambda}{\mathrm{NA}}, \qquad \text{Eq. 1.4}$$

noticeably smaller than the Rayleigh criterion. However, the Sparrow criterion is more commonly applied to astronomical imaging where the resolution of point sources is more useful than the separation of larger structures.

The final resolution criterion – the Abbe diffraction limit – is the criterion most commonly discussed in optical microscopy. The Abbe limit describes two point sources as resolved when there is no overlap between the Full Width Half Maxima (FWHMa) of the central maxima of the imaged point sources.

This relationship between resolving power and NA was first formally defined by Ernst Abbé in 1873. For lateral resolution it is given by:

$$d_{x,y} = \frac{\lambda}{2\mathrm{NA}}, \qquad \text{Eq. 1.5}$$

and for axial resolution is defined as:

$$d_z = \frac{2\lambda}{\mathrm{NA}^2} \qquad \text{Eq. 1.6}$$

The diffraction barrier can be alternatively represented by directly considering the image formation model. In 2D widefield fluorescence microscopy, the intensity (I) at a point ($\vec{r_i}$) in the acquired image is a function of the equivalent point ($\vec{r_s}$) in the sample plane,

$$I(\vec{r_i}) = \left(S(\vec{r_s}) \cdot E(\vec{r_s})\right) \otimes PSF(\vec{r_s}). \qquad \text{Eq. 1.7}$$

Here, $S(\vec{r_s})$ represents the distribution of fluorophores in the sample; $E(\vec{r_s})$ is the excitation intensity at the point $\vec{r_s}$; and $PSF(\vec{r_s})$ is the Point-Spread Function (PSF) of the imaging system. The transformation $\vec{r_s} \rightarrow \vec{r_i}$ describes the magnification and rotation of the image of the sample. For simplicity, the magnification is taken as 1 and the rotation as 0, i.e. $\vec{r_i} = \vec{r_s} = \vec{r}$. Hence equation 1.4 becomes:

$$I(\vec{r}) = \left(S(\vec{r}) \cdot E(\vec{r})\right) \otimes PSF(\vec{r}). \qquad \text{Eq. 1.8}$$

The PSF is the blurring factor of the system which can be thought of as the paintbrush with which the final image is drawn. Figure 1.11 shows a calculated PSF for a typical microscope diffraction-limited microscope. Given the small size of the side-lobes, the PSF is typically approximated to a Gaussian function with a FWHMa defined by the Abbe resolution ceriterion. By considering a point-emitter in the sample plane, i.e. when $S(\vec{r})$ is a delta function, equation 1.8 becomes:

$$I(\vec{r}) = \left(\delta(\vec{r}) \cdot E(\vec{r})\right) \otimes PSF(\vec{r}). \qquad \text{Eq. 1.9}$$

Under uniform illumination (i.e. $E(\vec{r}) = 1$ for all $\vec{r}$), the image recorded is simply $PSF(\vec{r})$. This means that single emitters appear as PSFs in the images acquired, which experimentally allows for direct measurement of the PSF by imaging a sub-diffraction point source.

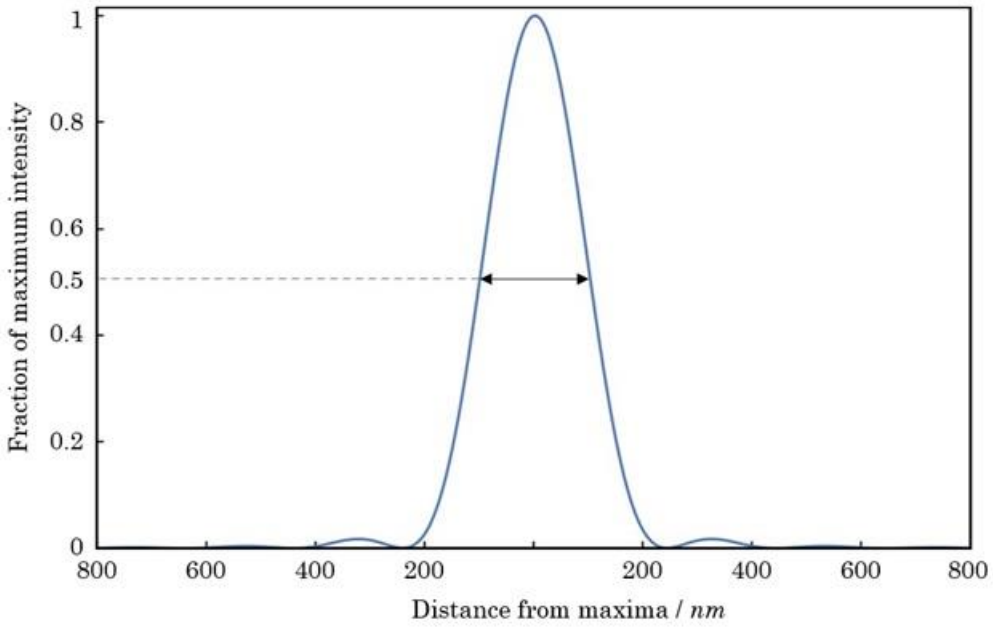

Figure 1.11: FWHMa of a PSF.

FWHMa of a calculated PSF. PSF was calculated for an objective lens with 1.35NA circularly polarised 532 *nm* light. The FWHMa is indicated by black arrows. Given the low intensity of the sidelobes, the PSF is usually approximated to a Gaussian centred at $r = 0$.

The image formation model can also be represented in frequency space by taking the Fourier transform of equation 1.5. The Fourier transform of the acquired image $\tilde{I}(\vec{k})$ is defined as a function of spatial frequencies $\vec{k}$ and is given by:

$$\tilde{I}(\vec{k}) = (\tilde{S}(\vec{k}) \otimes \tilde{E}(\vec{k})) \cdot OTF(\vec{k}). \qquad \text{Eq. 1.10}$$

Here the dot-product and convolution have been swapped according to the definition of the Fourier transform. $OTF(\vec{k})$ is the Optical Transfer Function (OTF) of the imaging system, equivalent to the Fourier transform of the PSF. In frequency space, the acts as a low-pass spatial frequency filter, blocking higher spatial frequencies associated with higher image resolution. In 2D frequency space, the OTF takes the form of a disc where the width is indirectly proportional to the FWHMa of the PSF and the resolution of the imaging system.

1.2 Breaking the diffraction barrier

While sub-diffraction electron microscopy is available, optical techniques are generally preferable if the structures being imaged can be resolved optically. Unfortunately, a wide number of biological processes and structures exist below the optical diffraction limit. For centuries, this limited the application of optical microscopy to studying larger biological structures, typically the size of organelles. At the turn of the millennium, the diffraction limit in optical microscopy was finally broken, a landmark achievement recognised by the 2014 Nobel Prize in Chemistry. This was jointly awarded to Profs. Stephan Hell, Eric Betzig and William E. Moerner for their development of two techniques capable of super-resolution imaging.[6] Since then, the field of super-resolution microscopy has grown rapidly and ongoing developments are building an increasingly powerful arsenal of tools for biologists.

1.2.1 STED microscopy

One of the earliest techniques used to break the barrier was Stimulated Emission Depletion (STED) microscopy for which Stefan Hell was awarded one third of the 2014 Nobel prize in Chemistry[7,8] In STED, two lasers are focused to a point in a sample (Figure 1.12). The first is a traditional Gaussian PSF excitation spot, as used in LSCM. The second beam is modified such that it forms a ring shape in the focal plane where the size of the central minima can be below the diffraction limit. This can either be achieved using a spiral phase plate or through azimuthal polarisation.[9] The wavelengths of the lasers are chosen such that the excitation Gaussian will excite all the fluorophores in the spot, and the ring-shaped beam will stimulate emission of the fluorophores outside of the central minima.[10] By stimulating the emission of photons at a wavelength that is not being detected, signal is only gathered from fluorophores fluorescing inside the central minima.

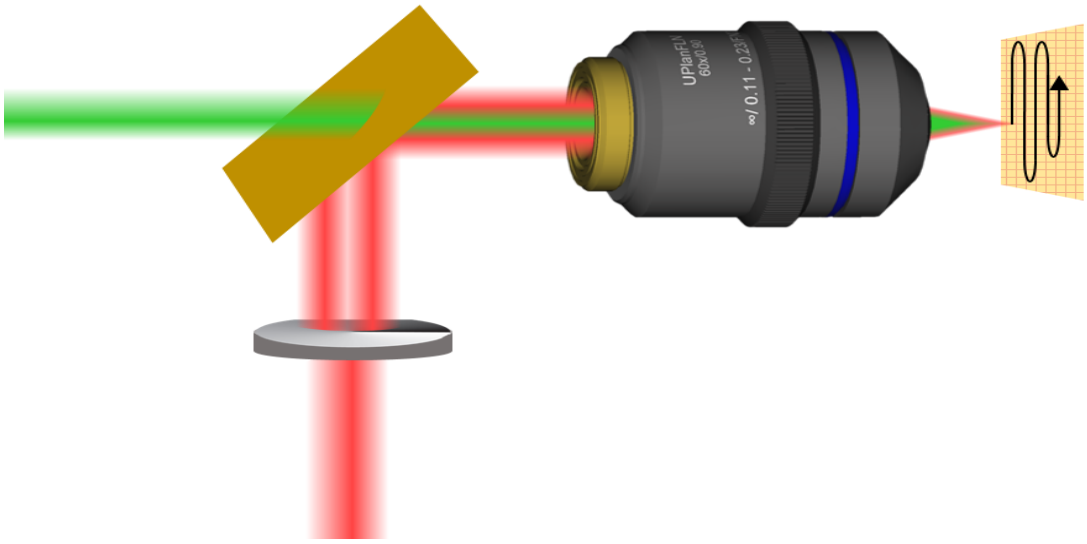

Figure 1.12: Method of illumination in STED microscopy.

STED. A Doughnut shaped depletion beam (red) is generated by passing a Gaussian beam through a spiral phase plate. This is coaxially merged with a Gaussian shaped excitation beam using a dichroic mirror before entering an objective lens. An image is built up by collecting the emission from the focal point of the beams in pixel-by-pixel fashion. This can be done either by scanning the sample through the excitation spot or by scanning the position of the beam focus in the sample using a pair of scan mirror placed after the dichroic mirror.

This effectively reduces the size of the excitation spot that is raster scanned through the sample thereby increasing resolution.

Figure 1.13 shows a comparison of confocal and STED microscopy imaging the mammalian cytoskeleton. In this way, the effective excitation spot has now been reduced. This smaller excitation spot is then raster scanned across the sample, and a super-resolution image is built up using a high sensitivity point detector. While the axial resolution remains unaltered, the lateral resolution in STED is now given by:

$$d = \frac{\lambda}{NA\sqrt{(1+I/I_S)}}. \qquad \text{Eq. 1.11}$$

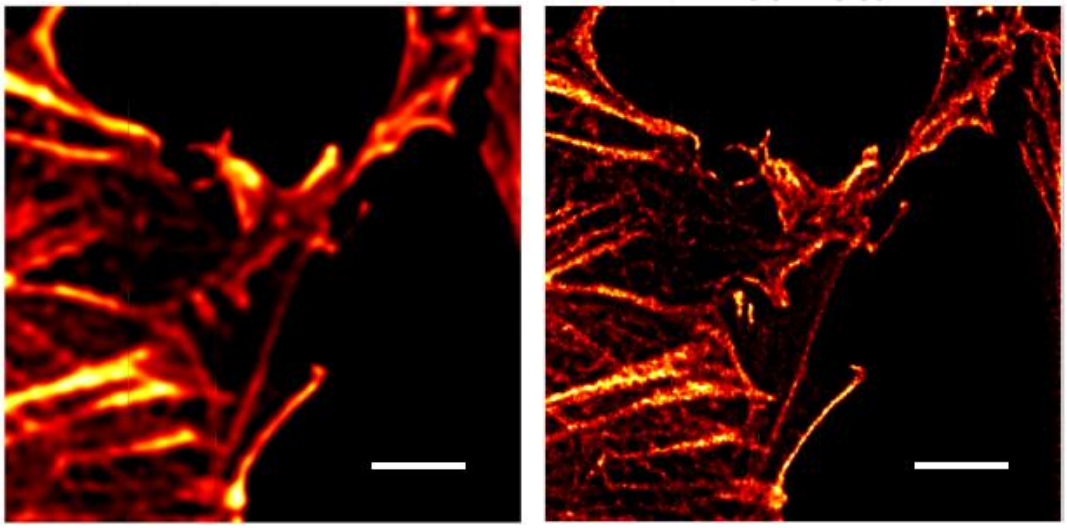

Figure 1.13: Confocal vs STED microscopy.

Comparison of confocal (left) and STED (right) microscopy imaging of the actin cytoskeleton. Cell was stained with ATTO647-phalloidin, scale bar is 2 μm. Image courtesy of Howard Vindin, CC BY-SA 4.0

Here, λ is the depletion wavelength, I is the intensity of the depletion beam and I_s is the saturation intensity of the fluorophore being used, i.e. the depletion beam intensity required to halve the fluorescent response. As an early super-resolution method, STED was a significant improvement on diffraction-limited imaging, although the improved resolution came at the cost of system constraints. The first major constraint was the limited number of available fluorophores. For STED to occur, the fluorophore must have a sufficiently high depletion cross section. In other words, the probability of undergoing stimulated-emission relaxation must be sufficiently high to deplete the excitation within the doughnut. The second constraint on STED is the sample's resilience to photodamage under the excitation and depletion light. Given the low probability of stimulated emission, the depletion beam intensity is typically orders-of-magnitude higher than required for conventional fluorescence microscopy. Such high-intensity beams are often prohibitively phototoxic, limiting live-cell imaging.

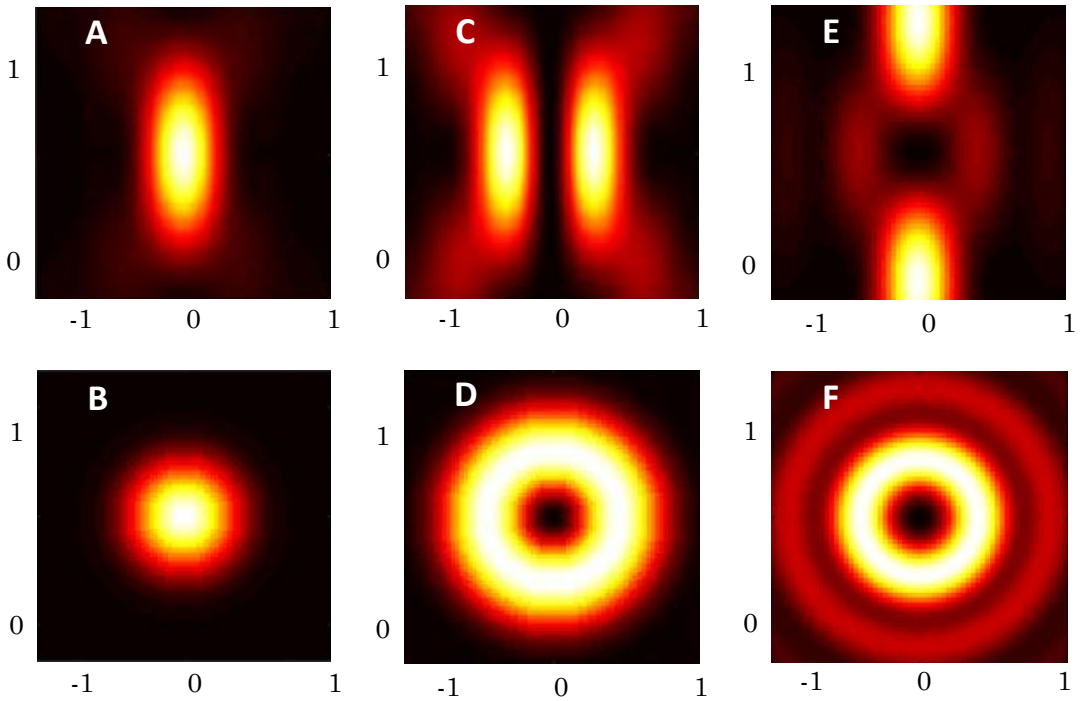

Figure 1.14: Sections through PSFs used in STED microscopy.

Units are in wavelengths and calculated for an objective NA of 1.4. Top row: x-z section through PSFs used in 2D and 3D STED. Bottom row: x-y section through PSFs at the origin. A&B: unmodified PSFs. C&D: depletion beam used in 2D STED. E&F: depletion beam used in 3D STED.

Considering the possible resolution, the key limitation of this early STED method is the axial resolution, which is equivalent to diffraction-limited imaging. There were two early innovations to improve on the axial resolution of STED. The first of these was the combination of STED with 4pi microscopy. [11–13] In this technique, two opposing objectives are focused onto the same plane of the sample, and simultaneously used for excitation and detection. With this method, axial resolution can be significantly improved, although at the cost of system complexity. This combination of 4pi microscopy and STED, known as isoSTED, has enabled resolutions down to 30 nm in all directions. The second method to improve on axial resolution was the use of more complicated phase profiles to generate a depletion beam that is also hollow in the axial direction (figure 1.14).[14] This allows for the effective excitation PSF to be shrunk isotropically, enabling 3D super-resolution. Since this requires only a single objective lens, it offers a much simpler optical setup than isoSTED, although with a reduced increase in lateral resolution.

Other advances in STED have revolved around the light sources used for excitation and depletion. Traditionally, the high depletion powers required meant that a pulsed laser source was used for depletion, and as a result, synchronised pulsed excitation was also needed. The lack of common pulsed sources in the visible wavelength range generally restricts this to fluorophores emitting in a narrow band of the far-red region (>600 nm). In biological imaging, this is particularly problematic if labelling more than one target, although developing technologies based on supercontinuum laser sources aim to address this by broadening range of available excitation and depletion wavelengths.[15,16]

There has also been some interest in using continuous wave (CW) rather than pulsed light sources for STED imaging. Since there is a much broader range of wavelengths available from CW sources, multi-colour labelling is considerably easier and widens the range of usable fluorophores. The downside to CW STED is the higher depletion powers needed. In pulsed

STED, all the power of the depletion beam is concentrated in the time when the fluorophores are excited, whereas in CW STED this power is spread out, meaning an excited fluorophore is exposed to comparatively less depletion power. To counter this, the average beam power in CW STED must be several times that of pulsed STED to achieve the same resolution increase.[17] CW STED does have the advantage that since fluorescence emission is not contained to just a short peak, fluorescent signal is increased. This allows for slightly lower pixel dwell times which can help reduce photodamage to the samples. One final approach is to combine pulsed excitation with CW-depletion.[18] CW STED with time-gated detection and pulsed excitation offers some improvement in contrast over CW-excitation CW-depletion, since any fluorescence that cannot be supressed by the depletion beam is reduced. However, the gains over pulsed-excitation pulsed-depletion are minimal, and as such, this technique is limited to only a few systems and has not been made available commercially.

1.2.2 Single-molecule imaging

Along with Stefan Hell for the development of STED microscopy, the 2014 Nobel Prize was shared with Eric Betzig and William E. Moerner, who together developed the first localisation-based super-resolution techniques.[19,20] Using Moerner's technique to image single molecules, Betzig built up super-resolved images of cells from the coordinates of all detected fluorophores in what is termed a pointillistic method. The principle behind localisation microscopy is that, although it appears as an Airy disc on the detector, a single fluorophore is actually a point source at

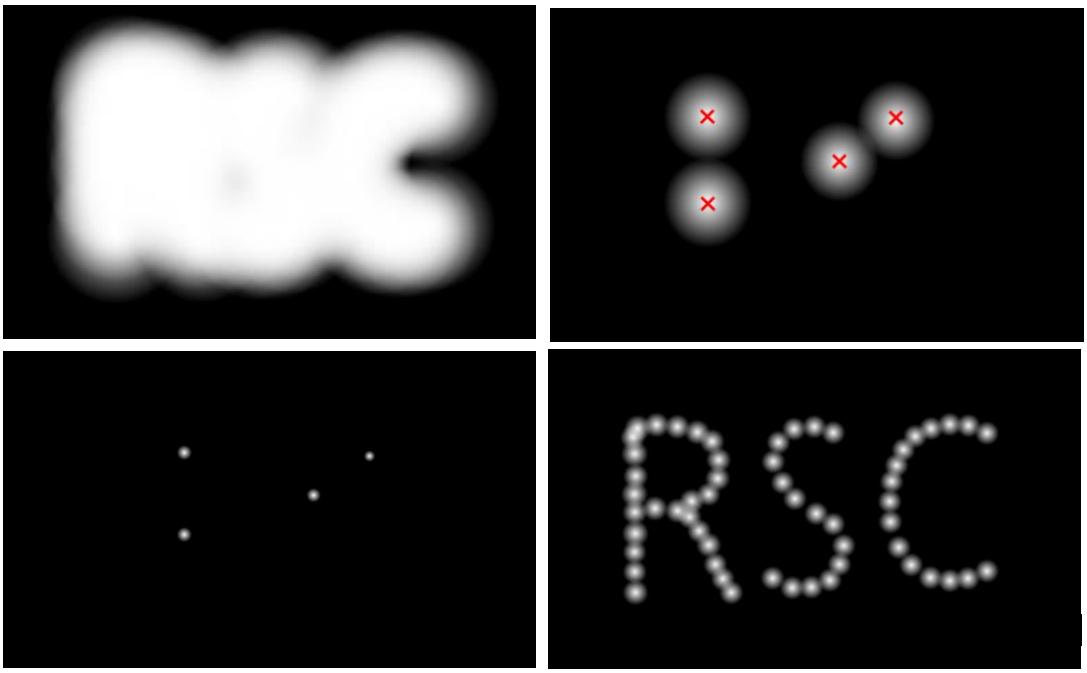

Figure 1.15 Principles of single-molecule localisation microscopy.

Top left: Diffraction-limited image. Top right: Diffraction-limited image of the same sample with only a few fluorophores active. Bottom left: Artificial PSFs are added to a model image at the coordinates of the localised diffraction-limited fluorophores. Bottom right: Final image is built up by repeating the steps with different fluorophores active in each frame.

the centre of this spot with fixed coordinates within the sample. In standard wide-field microscopy, identifying single and close-together fluorophores is impossible due to the overlap of their emission PSFs. However, if only a few fluorophores are emitting at any one time, they can be localised as point sources by finding the centre of the Airy disc, approximated to a Gaussian spot in the acquired images. This is shown in Figure 1.15 By reversibly switching off most of the fluorophores in a sample, the remaining active fluorophores can be localised to sub-pixel resolution and assigned coordinates in the final image (assuming sufficient distance between active molecules). By repeating the process and activating a different series of fluorophores each time, a map of all the fluorophores in the sample can be constructed from the measured coordinates. In this reconstructed image, the size of a fluorophore in the image is determined by the number of photons that were collected from it. The resolution of Single-Molecule Localisation Microscopy (SMLM) is determined by the accuracy of the fluorophore localisation, itself dependent

on the total number of photons from the fluorophore which can be detected before it is turned off. This is represented by the size of the spots which are added to the final reconstructed image. The lower bound on the variance of these Gaussian spots is given by:

$$\mathrm{V} = 2\frac{\sigma_a^2}{N}\left(1 + 4\tau + \sqrt{\frac{2\tau}{1+4\tau}}\right), \qquad \text{Eq. 1.12}$$

where $\tau = 2\pi\sigma_a^2 b/(Na^2)$ and $\sigma_a^2 = \sigma^2 + a^2/12$. N is the number of photons collected; b is the background (expected number of photons per pixel); a is the pixel size; and σ_a is the width of the spot on the camera.[21] The factor of 2 is introduced to account for noise in Electron-Multiplying Charge-Coupled Device (EMCCD) cameras. Typically, as a lower bound on the variance, equation 1.12 underestimates the achieved resolution in SMLM which can be more formally quantified using more sophisticated methods such as Fourier ring correlation (see chapter 3).

SMLM was first achieved with Photo-Activation Localisation Microscopy (PALM)[19]. This used a Photo-Activatable-GFP variant (PA-GFP) which naturally exists in a non-fluorescent off state. PA-GFP can be switched to a fluorescent state by activation with 405 nm light. With brief, low intensity 405 nm illumination it is possible to activate only a fraction of PA-GFP, which will then fluoresce with 561 nm excitation. Assuming a sufficiently low density of activated PA-GFP, those fluorescent proteins can then be isolated and localised. The activated PA-GFP is then permanently switched off by photobleaching with excessive 561 nm excitation, and the process can be repeated until all PA-GFP particles have been localised and bleached.

Shortly after PALM, Stochastic Optical Reconstruction Microscopy (STORM)[22] was developed as another way to localise fluorophores. In its first implementation, Rust et al. used the cy3-cy5 dye pair as the label. During imaging, cy5 is first forced into a stable off state by high intensity 633 nm light. If the two fluorophores are sufficiently close together, cy3 excited by 532 nm light then reversibly activates the cy5 emitter. The

activated cy5 then fluoresces at 633 nm emission before returning to its dark state. The activating 532 nm illumination is pulsed at a low intensity to ensure that at any one time, only a small subset of the cy5 emitters are fluorescing. As with PALM, if there is sufficient distance between the active emitters, they can then be localised. STORM has the advantage over PALM in that the photoswitching is reversible, so imaging can be repeated to study time-varying systems (assuming minimal movement of fluorophores during each image acquisition).

It was later found that organic fluorophores can switch themselves between light and dark states without an activator fluorophore. This switching forms the basis of the related technique direct-STORM (dSTORM).[23,24] To generate the stable off state, dSTORM uses the chemical reduction of excited fluorophores in their triplet state to a dark state anion. This process of spontaneous quenching can be enhanced with the addition of a thiol into the imaging medium. The fluorescent state can be recovered by subsequent oxidation of the dark state anion and can be enhanced by addition of an oxidising agent or illumination with 405 nm light. Most dSTORM studies control the relative concentrations of a thiol and an oxidising agent while varying the 405 nm light intensity to optimise the number of fluorophores active at any one time. This direct switching is a property of most organic fluorophores and greatly increases the number of available dyes to facilitate multi-label imaging.

Currently PALM, STORM and dSTORM provide the best resolutions of any nanoscopic technique, with measurements $< 1\,nm$ being made.[25] As with all super-resolution methods, SMLM has its limitations and there is a trade-off for this very high resolution. Primarily, separating the fluorophore temporally means that imaging can be incredibly slow, limiting applications in live-cell imaging. The phototoxicity associated with the bleaching and high intensities required for PALM further limits its use in live-cell studies. Recently, temporal resolution has been increased with more sophisticated methods to localise fluorophores. For example,

statistical methods increase the density of active fluorophores that can be isolated, thus reducing the number of frames that must be acquired.[26]

1.3 Motivation for this work

Although there is continual development in the field of super-resolution microscopy, there is still no one-size-fits-all solution for biological imaging. Often, there is a trade-off between resolution improvement and suitability for live-cell imaging. This project hopes to bridge the gap between these very high-resolution techniques and another super-resolving technique, Structured Illumination Microscopy (SIM), which is the subject of chapter 2. SIM is an excellent candidate for super-resolution live-cell imaging, although it lacks the higher resolutions possible with STED and SMLM. In this project, a novel SIM technique is developed to improve on the resolution enhancement possible with SIM while retaining its performance of live-cells

2. Structured-illumination microscopy

Summary: *this chapter will introduce the concept of structured illumination microscopy as a super-resolution technique. Building on a description of the theory behind the technique, it will outline key advances in the field, including new image reconstruction techniques and methods for enhancing resolution increase.*

2.1 Introduction

Structured Illumination Microscopy (SIM) describes a range of techniques that improve resolution by extracting more spatial information from the sample than diffraction-limited imaging.[27,28] Early resolution improvements in this field came by illuminating the sample with laterally-modulated light to increase resolution in the sample plane. SIM is best described by considering the image formation model. Recalling equation 1.5:

$$I(\vec{r}) = \big(S(\vec{r}) \cdot E(\vec{r})\big) \otimes PSF(\vec{r}) \,, \qquad \text{Eq. 2.1}$$

the image acquired, $I(\vec{r})$, is a function of the sample structure, $S(\vec{r})$, the excitation pattern, $E(\vec{r})$, and the PSF of the imaging system. The simplest SIM methods use sinusoidal striped pattern excitation. In this case, the function $E(\vec{r})$ becomes:

$$E(\vec{r}) = E_0\big(1 + \cos\big(\vec{k}_0 \cdot \vec{r} + \varphi\big)\big) \,, \qquad \text{Eq. 2.2}$$

where $\vec{k}_0$ is the spatial frequency of the sine pattern and φ is the phase. Substituting this into equation 2.1 and taking the Fourier transform we get:

$$\tilde{D}\big(\vec{k}\big) = E_0[\tilde{S}\big(\vec{k}\big) + 0.5\tilde{S}\big(\vec{k}+\vec{k}_0\big)e^{i\varphi} + 0.5\tilde{S}\big(\vec{k}-\vec{k}_0\big)e^{-i\varphi}] \cdot OTF\big(\vec{k}\big) \qquad \text{Eq. 2.3}$$

Looking at equation 2.3, the detected Fourier spectrum is now a linear superposition of three zones of the frequency space of the sample structure. The relative intensities of the frequency components are dependent on the phase of the excitation pattern. This means that three separate images, each with a phase shift of $^{2\pi}/_{3}$ in the pattern, are needed to separate out these signals. This process will, assuming the excitation frequency is diffraction-limited, double the resolution of the reconstructed image in the direction of the vector of the sinusoidal excitation pattern, $\vec{k}_0$. To achieve isotropic resolution doubling, this process must be repeated at least three times with different directions of excitation patterns. Figure 2.1 shows the steps of image formation in SIM.

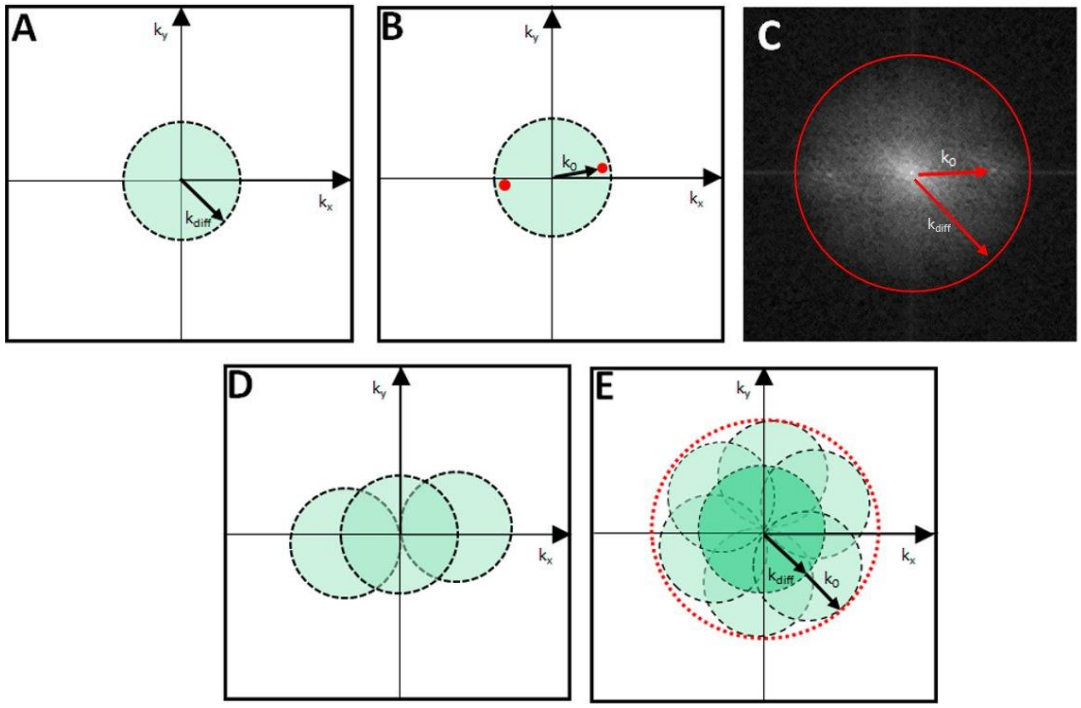

Figure 2.1: SIM methodology visualised in frequency space.

A: In diffraction-limited imaging, only a small region (dashed circle) of frequency space can be observed. This region is defined by a cut-off frequency, k_{diff}, proportional to the resolution limit. **B:** Under striped-pattern illumination, the frequency components of the excitation pattern, k_0, are chosen to be as close to the diffraction limit as possible, to maximise resolution increase. The observed region of frequency space now contains frequency components from outside the supported region. **C:** Real image data of B. **D:** After shifting the phase of the pattern, the different regions of frequency space can be isolated and moved into the correct place in the image. **E:** Repeating the process for multiple pattern directions allows isotropic for resolution increase, i.e. resolution increase in all directions. The new frequency cut-off is shown by the red circle and is the sum of k_{diff} and k_0. Adapted from Ward et al. 2017 [37]

In this example, the simplest case of exciting the sample with a unified striped pattern has been used. It has also been demonstrated that the SIM technique can be repeated with many different excitation patterns, including: regular, evenly-spaced spots; *pseudo*-random speckle patterns; and – surprisingly – unknown, irregular patterns in a process called blind SIM.[29] With proponents of each of these techniques claiming its benefits, currently the most popular technique remains the classic striped pattern, as this still achieves the best resolution for the number of pictures acquired.[30]

2.2 Image reconstruction for structured illumination microscopy

For striped-pattern SIM, each acquired image only contains three well-defined regions of frequency space and separating them is a relatively simple process. Since this process takes place exclusively in frequency space, it is defined as a 'Wiener filter', a term used to describe any deconvolution technique which operates in frequency space. Other examples of Wiener filters are those used in the more general field of deconvolution microscopy, which has become one of the most popular ways to improve image quality in diffraction-limited imaging. One example of a popular deconvolution technique is in 3D widefield imaging where a sequence of images, known as a z-stack, is acquired of the same region of the sample at different focal planes. Z-stacks are used to study the 3D structures of biological samples, for example measuring the height of cells in the axial direction along the axis of the imaging system. The 3D nature of excitation light in widefield microscopy means that when any image of a sample is taken it will contain light from fluorophores above and below the plane being imaged. In the final image this manifests as out-of-focus blurring, leading to a low axial resolution and poor depth sectioning. In this case, deconvolution microscopy attempts to improve the depth sectioning of 3D z-stacks by using knowledge from the images of different

planes simultaneously. For example, if a fluorophore is known to be in focus in one of the images in the stack, any out-of-focus light it produces which appears in images of other planes can be removed. This removal of out-of-focus blur greatly increases the depth sectioning ability of widefield microscopes, making results comparable with those from confocal systems. The obvious disadvantage is that for the highest quality images, z-stacks must be taken, meaning repeated imaging of the sample is required.

2.3 Advances in structured illumination microscopy

From its early implementations SIM has undergone significant advances in to address both and this next section aims to summarise the key innovations in the field.

2.3.1 Increasing axial resolution in structured illumination microscopy

Addressing the issue of axial resolution in SIM was one of the earliest developments in the field. Before lateral SIM, using light structured in the axial direction – in the form of standing waves – had previously been used to improve axial resolution.[31] This technique, Standing Wave Fluorescence Microscopy (SWFM), involved illuminating the sample with two opposing objectives and aligning one of the maxima of the standing wave with the focal plane of the imaging objective. The axial resolution was now not defined by the 3D excitation PSF of the focusing lens but by the period of the standing wave. For blue excitation light this gives an axial resolution of $50nm$ compared to the $700nm$ resolution possible in diffraction-limited microscopy. The obvious downside of this is the requirement to have two, high NA objective close to the sample plane meaning its use was limited in biological imaging to thin, non-scattering samples. 3D structured illumination was first achieved by using three-beam interference at the objective in place of the two-beam interference

commonly used in 2D SIM.[32] Three-beam interference remains the most popular method for pattern generation as converting from 2D to 3D SIM systems is relatively simple.

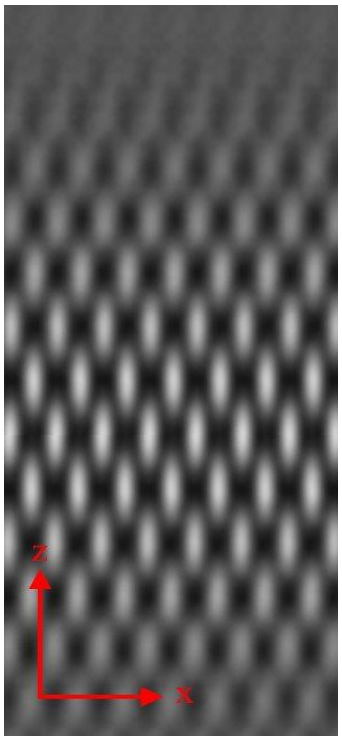

Figure 2.2: Axially structured illumination.

Cross section through axially structured light generated by three-beam interference.

Using 3D SIM, a lattice structure is introduced into the excitation light and there is spatial frequency mixing between the light and the sample structure in all directions. A cross section through this lattice light pattern is shown in Figure 2.2. Since each image acquired now has frequency information from five regions of frequency space, five phase shifts in the pattern are required at each angle to separate the frequency information. In total, this means 25 images of the same region of a sample must be taken for each reconstructed slice through the samples. With high speed cameras this gives imaging times roughly equivalent to those for LSCM. The lateral resolution in 3D SIM remains the same as 2D SIM but the axial resolution is now improved proportionally to the axial frequency of the light pattern. With the three-beam interference method, the frequency of the axial pattern is still diffraction-limited meaning again a doubling of resolution is possible. This isotropic resolution increase, combined with the compatibility of the SIM technique with live-cell imaging, makes 3D SIM one of the most popular super-resolution techniques in biological imaging.

Consequently, the vast majority of commercial SIM systems are now capable of both 2D and 3D SIM. The main disadvantage of 3D is the stability of the 3D excitation pattern. As with all forms of SIM, precise knowledge of the excitation pattern is vital and any distortions in the ideal pattern detrimentally affects image quality. This problem is worse in 3D SIM where pattern fidelity (i.e. pattern spacing) must be maintained across the entire Field Of View (FOV) in all three direction. As such, 3D SIM it limited in its ability to image deep into samples or through optically dense targets. Because of this, for deeper imaging the potential axial resolution increase is lost and using a diffraction-limited confocal technique is often preferable.

2.3.2 Increasing lateral resolution in structured illumination microscopy

As is clear in equation 2.3, the possible resolution increase is directly proportional to the spatial frequencies in the excitation pattern. Traditionally, this is the maximum frequency allowed by the excitation OTF which limits the resolution increase to double that of a wide-field microscope. To increase the resolution further, it is necessary to introduce higher spatial frequencies into the excitation pattern. The two most successful methods employed to achieve this are Saturated-SIM (SSIM)[33] and Plasmonic-SIM.[34] SSIM, which is also sometimes categorised as a Reversible Saturable Optical Fluorescence Transitions (RESLOFT) technique, enhances the resolution of SIM using the non-linear optical properties of fluorophores to simulate a high frequency illumination. Under low excitation intensities, fluorophores exhibit a linear response to excitation, that is the emission is directly proportional to illumination intensity. However, once a fluorophore has been excited, it remains in the excited state for a short period of time before transitioning back down to a lower level. Because of this delay, there is a critical limit to the number of

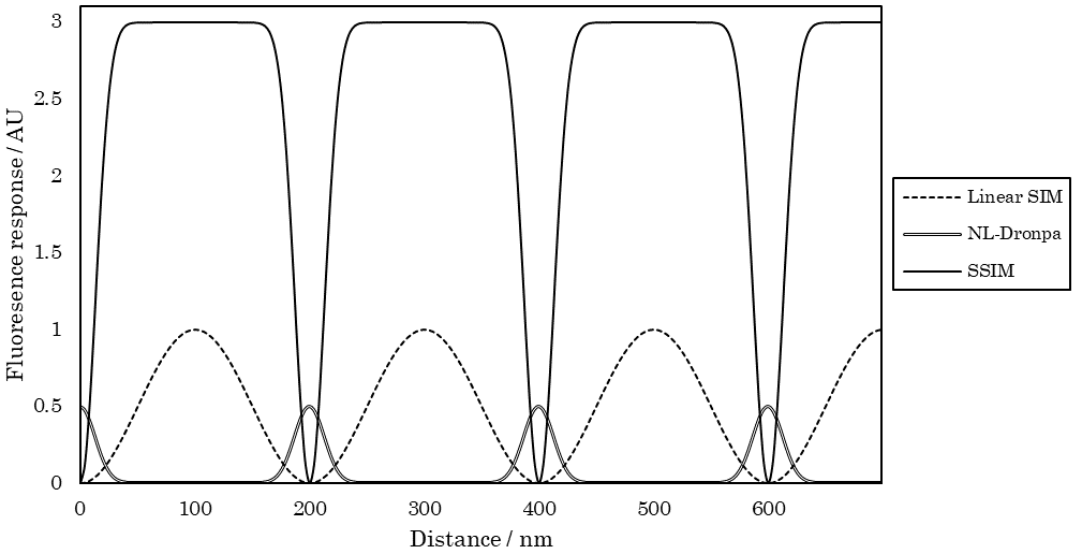

Figure 2.3: Fluorescent response in non-linear SIM.

Fluorescent response of fluorophores under different illumination schemes. The dashed curve shows the typical response of fluorophores to low intensity illumination where emission is proportional to illumination intensity. The solid curve shows the response under intense illumination with a pattern of the same period as in the linear case. At the high intensity regions of the excitation light, the fluorescent response saturates and squares off. The double line shows the fluorescent response of fluorophores in the NL-DRONPA scheme. The FWHM of the effective excitation maxima has been reduced which is the sources of the higher spatial frequencies.

photons per unit time that a fluorophore can emit as, under sufficient illumination intensity, the population of fluorophores is now entirely in the excited state. This saturation of the excited state presents as a squaring of the fluorescence response to striped excitation patterns, shown in figure 2.3. This squaring of the response is defined in Fourier space as an introduction of higher spatial frequencies into the excitation pattern, specifically harmonics of the original sinusoidal pattern. As with conventional SIM, the sample is exposed to these excitation patterns at different phases and orientations, and the resolution is improved by deconvolution of the acquired images. However, in SSIM there are spatial frequencies from more than three regions of the sample's frequency space (Figure 2.4) so many more phase-shifted images must be taken to extract the information. Furthermore, since a greater region of frequency space is sampled, more pattern rotations must also be used to achieve isotropic resolution increase. In the original SSIM implementation 9 phase shifts

and 12 rotations were needed requiring a total of 108 exposures for a single image, reducing temporal resolution. This, combined with the high excitation powers required for saturation, makes SSIM very susceptible to photobleaching and movement of the sample. In addition, the high levels of phototoxicity associated with a saturated excitation state makes live-cell imaging virtually impossible.

Furthermore, although this technique allows a theoretically infinite resolution, photobleaching typically limits resolution increase to only a few times greater than SIM.[35]

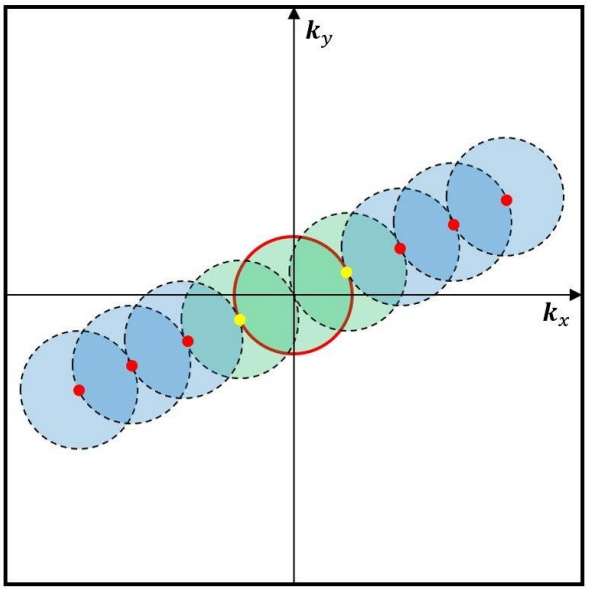

Figure 2.4: SSIM Visualised in frequency space.

As with regular SIM the first three regions (green) are sampled by the basic frequencies of the striped pattern (yellow spots). The squaring of the striped pattern by saturation introduces harmonics into the excitation pattern (red spots) shifting further regions of frequency space (blue) into the range of the detection OTF (red ring).

Another way to introduce the higher frequencies into the illumination pattern is with photoswitchable fluorophores, specifically the GFP related fluorescent protein, Dronpa.[33,36] This protein fluoresces brightly at 488 *nm* excitation before moving to a dark state. It remains in this dark state until switched on by UV light at 405 *nm*. By using a low power sinusoidal UV illumination and bright 488 *nm* excitation, the dark state is saturated and fluorescent response is limited to only regions with sufficient UV

illumination. The peaks in the effective excitation pattern have a smaller FWHM than those in the diffraction-limited patterns which, like SSIM, contains higher frequency components than classically allowed. The advantage of SIM using Dronpa is that the dark state can be saturated with a much lower illumination intensity than is required to saturate emission in SSIM. This reduces photo-bleaching and photo-toxicity making the technique more suitable for live-cell imaging. Currently the biggest issue with the use of Dronpa in SIM is that it requires fluorophore emission to remain the same before and after switching. In reality there is loss of intensity after many cycles and this gradual reduction in emission means the effective excitation patterns differ from the ideal patterns required. As such, future improvements in this technique are likely to revolve around the development and discovery of more suitable fluorophores.

2.4 Image scanning microscopy

As well as improvements in the resolving power of SIM, there have been many developments in the implementation of the basic SIM procedure. A prominent example of this is Image Scanning Microscopy (ISM), a variant of SIM using a single PSF as the patterned illumination.[37][38][39] By definition, this diffraction-limited PSF contains all the spatial frequencies permitted by the objective (i.e. the OTF). As with all patterned illumination, the spatial frequency components of the sample are mixed with those of the excitation pattern, meaning high spatial frequencies of the sample are moved into the range of the detection OTF. In ISM all the spatial frequencies in the excitation PSF are responsible for shifting the higher spatial frequencies of the sample into the observable region. Given that the maximum frequency in the excitation pattern is the maximum frequency supported by the excitation OTF – like other SIM techniques – this limits the resolution improvement to double that of diffraction-limited imaging.

ISM was initially not considered a SIM technique and was first applied to LSCM where, the source of the super-resolution information was conceptualised as the result of and overlap of the detection and emission PSFs. Theoretically, when using an infinitely small pinhole in LSCM, the image formation model from equation 2.1 becomes:[40]

$$I(\vec{r}) = S(\vec{r}) \otimes [PSF_{ex}(\vec{r}) \cdot PSF_{det}(\vec{r})] \quad \text{Eq. 2.4}$$

Comparing this with equation 2.1, this is equivalent to acquiring an image of the sample under uniform illumination and with the effective PSF now the product of the excitation (PSF_{ex}) and detection (PSF_{ex}) PSFs. Given that the FWHM of the product of the two PSFs is smaller than that of either one, the effective PSF is now smaller than in diffraction-limited microscopy resulting in a higher resolution image. Using this theory, the super-resolution information can be collected simply by reducing the size of the pinhole to approximate the image formation model described by equation 2.4. However, the amount of light discarded by this method makes it impractical to implement as any resolution improvement is countered by the decrease in Signal to Noise Ratio (SNR). ISM was developed as a means to gather the information without the closed pinhole. In ISM, the point detector in a LSCM is replaced with an array detector (camera) and an image from the camera is acquired at every scan position. The super-resolution image is then recovered through the process of 'pixel reassignment'.[40] Pixel reassignment involves shrinking the image acquired on the camera and then placing this image into a running total image which becomes the final super-resolution image. Since pixel reassignment is extracting the super-resolution information from the product of the excitation and emission PSFs, the shrink factor chosen depends on the Stokes' shift of the fluorophore used and helps determine the magnitude of the resolution increase.[40]

2.5 Multi-focal Structured Illumination Microscopy

Multi-focal (or multi-spot) Structured Illumination Microscopy (MSIM) was originally developed as a parallelised version of ISM.[41] MSIM offers several advantages over ISM, most importantly the increase in temporal resolution. Image acquisition speed in LSCM is already limited by its scanning nature and, given that the array detectors are less sensitive than the PMTs / APDs typically used, scan times for ISM must be reduced in order to reach a sufficient pixel dwell time. The slow scanning nature of ISM results in imaging times of around two minutes for a 20µm x 20µm area. MSIM attempts to overcome the slow imaging times by parallelising the approach, using multiple excitation spots simultaneously and shifting the grip pattern over the image.

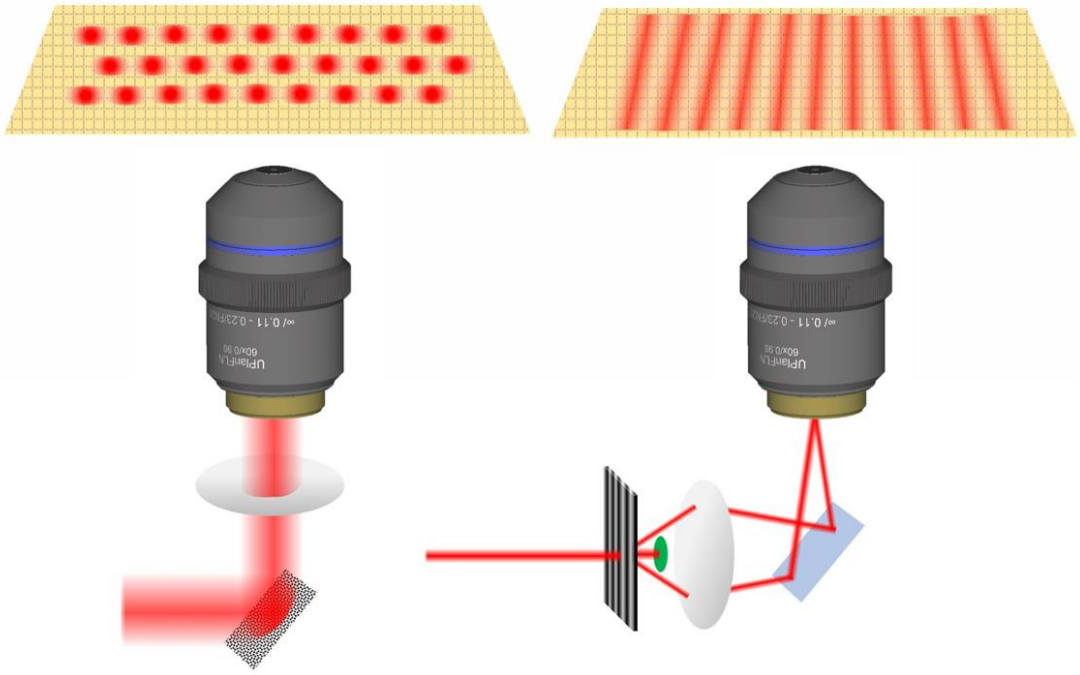

Figure 2.5: Pattern projection techniques in SIM.

Left: MSIM pattern projection achieved using a SLM. An expanded beam illuminates an SLM placed in conjugate image plane to the sample. At the sample plane (magnified above the setup) the image of the SLM appears as bright excitation spots corresponding to 'on' pixels on the SLM. Right: For striped pattern SIM a diffraction grating is used to split up an incoming beam. The 1st order diffracted beams are focussed into the objective. The sample plane, the interference pattern generated by the two beams produces a striped excitation pattern. For 2D SIM the 0th order diffracted beam is blocked from entering the objective. In 3D SIM, three beam interference is needed and the 0th order is allowed to pass into the objective.

In MSIM, the multi-spot grid patterns can be generated either with a spatial light modulator (SLM) or a microlens array.[42,43] Based on the microlens approach, a modified version of this spinning disc method has recently been developed where the ISM pixel reassignment happens all-optically.[44]

2.5.1 Image reconstruction in multi-spot structured-illumination microscopy

In its first incarnation, image reconstruction in MSIM was carried out through pixel reassignment to offer a $1/\sqrt{2}$ resolution increase followed by post-processing to extract the full doubling of resolution.[41] In the pixel reassignment method, the locations of the individual excitation spots are calculated and a region of the whole image around each spot is extracted, shrunk and added into a running total image which becomes the final super-resolution image.

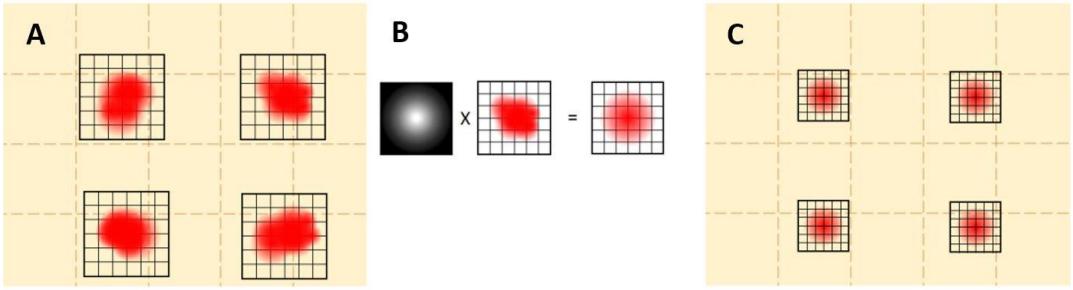

Figure 2.6: Pixel reassignment in MSIM.

A: In the raw image captured, the location of the excitation spots is determined and a region of the image around this point is extracted. B: The extracted images are digitally pinholed by remove out-of-focus light from around the excitation spot. C: The pinholed image is shrunk at inserted into the running total super-resolution image. Adapted from Ward et al. 2017 [37]

However, an alternative approach is to represent MSIM as a structured-illumination technique, where the excitation pattern is the convolution of a 2D delta-comb (III_T) with the excitation PSF, i.e.

$$E(\vec{r}) = \mathrm{III}_T \otimes PSF_{ex}(\vec{r}) \qquad \text{Eq. 2.5}$$

Where the period of the delta-comb (T) represents the spacing of the spot pattern. Combining this with the generalised image formation model (equation 2.1) gives a final predicted image of:

$$I(\vec{r}) = \big(S(\vec{r}) \cdot \mathrm{III}_T \otimes PSF_{ex}(\vec{r})\big) \otimes PSF_{det}(\vec{r}) \qquad \text{Eq. 2.6}$$

Unlike striped-pattern SIM however, there exists no direct way to recover the structured illumination information in frequency space. As such, MSIM requires the development of novel deconvolution approaches to reconstruct the final super-resolution image from the raw data. One such method is the family of reconstruction algorithms known as Maximum Likelihood Deconvolution (MLD)[45] or Maximum Likelihood Estimation (MLE), a term also used to describe different but related techniques in the deconvolution of non-SIM images. Briefly, the principle behind MLD/MLE is to find an estimate of the sample image which best matches the acquired data under the known imaging conditions. The advantage of MLD/MLE over direct deconvolution in SIM is that consideration of imaging noise can be built directly into the reconstruction model, rather than having to be applied separately after reconstruction. To achieve this, the image formation model described by equation 2.1 is modified to be:

$$I(\vec{r}) = \big(S(\vec{r}) \cdot E(\vec{r})\big) \otimes PSF(\vec{r}) + n(\vec{r}), \qquad \text{Eq. 2.7}$$

where the terms for the final image, excitation pattern, sample and *PSF* remain the same, but an additional term for the image noise $n(\vec{r})$ is added. This noise term represents all noise present in the image, the majority of which is Gaussian noise from camera readout and Poisson noise associated with low photon counts. Maximum likelihood approaches are inherently statistical approaches to image reconstruction, and as such, make use of probability distributions to describe the likelihood of acquiring images. To best represent the image formation model, the mixed noise probability distribution is used to account for Gaussian and Poisson noise.[46][45] For this distribution, the probability of making an observation is given by:

$$P(I|\mu,\sigma^2) = \frac{e^{-(\mu+\sigma^2)}(\mu+\sigma^2)^{\mu+\sigma^2}}{(\mu+\sigma^2)!}. \quad \text{Eq. 2.8}$$

Here, P is the probability of making the observation (i.e. acquiring the image *I)*, given the expected observation μ. σ^2 is the variance of the Gaussian read-out noise. For fluorescence microscopy, the expected image, μ, can be calculated using the image formation model (equation 2.1) given an estimate for the sample structure $S(\vec{r})$, the known excitation pattern $E(\vec{r})$ and the *PSF* of the system. In SIM microscopy, where there are multiple images acquired, it is possible to combine all of the observations to calculate a probability of an estimated sample $S(\vec{r})$ being the origin of the observations. This is achieved using Bayes' theorem for combining probabilities:[45]

$$P(S|I_1, I_N \dots I_N) = \frac{P(I_1, I_2 \dots I_N|S) \cdot P(S)}{P(I_1, I_2 \dots I_N)}. \quad \text{Eq. 2.9}$$

Image deconvolution is the process of maximising this probability, obtaining the most likely estimate of $S(\vec{r})$ to give the images $I_1, I_2 \dots I_N$. In statistics, maximising the probability can alternatively be considered as minimising the negative logarithm. Taking the negative logarithm of equation 2.9 gives a two-term error function:

$$-\ln P(S|I_1, I_2 \dots I_N) = -\ln P(I_1, I_2 \dots I_N|S) - \ln P(S). \quad \text{Eq. 2.10}$$

This can be represented as $E = L + F$. When taking the negative logarithm of equation 2.9, the term for $P(I_1, I_2 \dots I_N)$ is ignored since it does not depend on the sample structure. The first term, $L = -\ln P(I_1, I_2 \dots I_N|S)$ can be calculated by simply taking the sum of the negative logarithms of equation 2.8 for each of the acquired images $I_1, I_2 \dots I_N$ and expected images $\mu_1, \mu_2 \dots \mu_N$:

$$L = \sum_i^N [(\mu_i + \sigma^2) - (I_i + \sigma^2) \ln (\mu_i + \sigma^2) + \ln \Gamma(\mu_i + \sigma^2 + 1). \quad \text{Eq. 2.11}$$

The second term of the error function, $F = -\ln P(S)$ is known as the 'regularisation function' and requires knowledge of the true sample structure. Image deconvolution in diffraction-limited imaging is inherently

an ill-posed problem as the frequency cut-off of the OTF means that some information is lost irretrievably. Because of this, the exact value for F is impossible to determine. However, a regularisation term is required to prevent the deconvolution breaking down while trying to recover zero-signal from outside the pass-band of the OTF. The choice of the regularisation function differs between deconvolution techniques, and with non-iterative deconvolution, F is usually taken to be a user-defined constant representing how much true high-resolution information was captured, essentially placing a limit on the deconvolution. To date, the deconvolution algorithms used for SIM are all of the iterative type and use a gradient descent method to find the minimum of the error function. The gradient descent method uses the derivative of the error function to generate an iteratively-updated estimate of the sample structure. The new estimate of the sample is given by:

$$S^{k+1} = S^k - \beta^k \frac{\partial E}{\partial S^k}, \qquad \text{Eq. 2.12}$$

where the value for β^k varies depending on the iterative algorithm. To simplify calculation in iterative deconvolution, the regularisation function in equation 2.10 is set to $F = 0$. To avoid the issue of breakdown when recovering zero-signal outside of the OTF, the deconvolution is limited by ending the iterations at a set point after the image has been sufficiently restored (but before breakdown). The regularisation term also serves another purpose in the error equation: providing information about the sample itself. Because of this, setting $F = 0$ also adds the constraint that in iterative deconvolution, the sum of the illumination patterns must be equivalent to uniform illumination to give an approximation to the underlying sample. Substituting the image formation model (equation 2.1) into equation 2.11 and taking the derivative gives:

$$\frac{\partial \mathrm{E}}{\partial \mathrm{S}} = 1 - \sum_{i=1}^{N} \left(\frac{I_i + \sigma^2}{\mu_i + \sigma^2} \otimes OTF \cdot E_i \right) \qquad \text{Eq. 2.13}$$

where again the summation is over the N illumination patterns.

2.5.2 Pattern-illuminated Fourier Ptychography

The first MLD deconvolution algorithm used was Pattern-illuminated Fourier Ptychography (PiFP).[47] PiFP works by setting the constant β^k in equation 2.12 to 1 and breaking down the update process into three steps as follows:

Step 1: Generate a temporary value, equivalent to the estimated image that would be acquired given the known illumination pattern, E^n, and the k^{th} estimate of the sample structure,

$$y_k^n = PSF \otimes (E^n \cdot S_k) \,. \qquad \text{Eq. 2.14}$$

Step 2: Generate an updated temporary value, y'^n_k, by comparing the Fourier transform of the predicted image $\mathcal{F}(y_k^n)$ with the Fourier transform of the actual acquired image $\mathcal{F}(I^n)$,

$$\mathcal{F}\left(y'^n_k\right) = \mathcal{F}(y_k^n) + \mathrm{OTF} \cdot \left(\mathcal{F}(I^n) - \mathcal{F}(y_k^n)\right) \,. \qquad \text{Eq. 2.15}$$

Step 3: After moving back into real-space, generate an updated estimate of the sample structure,

$$S_{k+1} = S_k + \frac{E_n}{(\max(E_n))^2} \cdot \left(y'^n_k - S_k \cdot E_n\right) \,. \qquad \text{Eq. 2.16}$$

Steps 1-3 are then repeated for each of the n illumination patterns. There is some debate over whether it is better to follow this procedure, updating the estimate S_k for every pattern, or to combine the information from all of the patterns simultaneously to update the sample estimate. It is proposed that updating the sample estimate based on the information in only one of the acquired images would make the process more susceptible to noise, although there is no evidence of this to-date.[48] It should also be noted that a newer version of the PIFP algorithm is proposed using an

update step with a varying value of β^k which varies with each update iteration to speed up convergence.[49]

2.5.3 Joint Richardson-Lucy Deconvolution

The joint Richardson-Lucy (JRL) algorithm was originally proposed for combining multiple images of the sample under the presence of Poisson noise,[50] but was more recently applied to combining images from SIM microscopes to reconstruct a super-resolution image.[51] The JRL algorithm is derived by setting the constant β^k in equation 2.12 equal to S_k giving:

$$S_{k+1} = S_k \cdot \sum_{n=1}^{N} \left(\frac{I_i + \sigma^2}{\mu_i + \sigma^2} \otimes OTF \cdot E_i \right) . \qquad \text{Eq. 2.17}$$

This variant of the JRL algorithm, based on the mixed-noise model (equation 2.7), is a more recent version than that initially used to reconstruct SIM data.[51] This is predicted to behave better in biological imaging as it is less affected by Gaussian and Poisson noise. The inclusion of the σ^2 also makes the algorithm more stable as it prevents unwanted artefacts in reconstruction for pixels where $\mu_i \ll I_i$.

2.6 Summary

This work focusses on developing a novel structured illumination technique based on the MSIM principle. Given that, for image reconstruction, MSIM requires significantly more pattern shifts the advantages over striped pattern SIM are not immediately apparent. However, the performance of MSIM rapidly overtakes that of striped-pattern SIM when imaging deeper into tissues. Typically, striped pattern SIM is limited to only a few μm into the sample as the striped patterns rapidly decay and are lost to out-of-focus signal. In contrast, the digital pinholling employed in MSIM means that this out-of-focus signal can be rejected allowing the pattern to be resolved deeper into tissues. This was demonstrated in the first MSIM implementation where SIM was possible 40 μm into a sample, nearly ten times deeper than possible using striped-pattern SIM.[41]

3. Enhanced multi-spot structured illumination microscopy

Summary: *this chapter introduces the concept of enhanced multi-spot structured illumination microscopy as a super-resolution technique. Through discussion of point-spread function engineering and difference microscopy, it will explain the theory behind the enhanced technique and present the results of simulated imaging.*

3.1 Introduction

Based only on single PSF excitation and generalised MLD, MSIM offers a versatile platform on which to develop more sophisticated imaging methods. For this project, a new technique, termed enhanced-MSIM (eMSIM), was developed by combining the field of PSF engineering with MSIM. PSF engineering is the process of altering the properties of a focusing system to change the distribution of light at the focal point. Applied to MSIM, this allows for precise engineering of the excitation pattern, and exploration of such excitation patterns on resolution improvement. To this end, eMSIM was developed to increase the resolution improvement of MSIM, and to provide a basis for further work exploring PSF engineering for SIM.

3.1.1 Point-spread function engineering

Excluding aberrations, the PSF of any focusing system can by modified by changing either the polarisation[52–55], phase[56,57] or amplitude[58] of the focused beam. During previous discussion of the excitation PSF, its description has been considered to be the Fourier transform of the OTF, i.e. the Fourier transform of the sum of all of the spatial frequencies supported by the focusing lens (microscope objective). While this is true for

the incoherent detection PSF, the excitation PSF varies from this model, as it is affected by the properties of the focused excitation beam. Assuming uniform illumination of the objective lens, and ignoring the effects of phase and polarisation, the Fourier transform model is accurate and often serves the purpose of describing the focal spot.

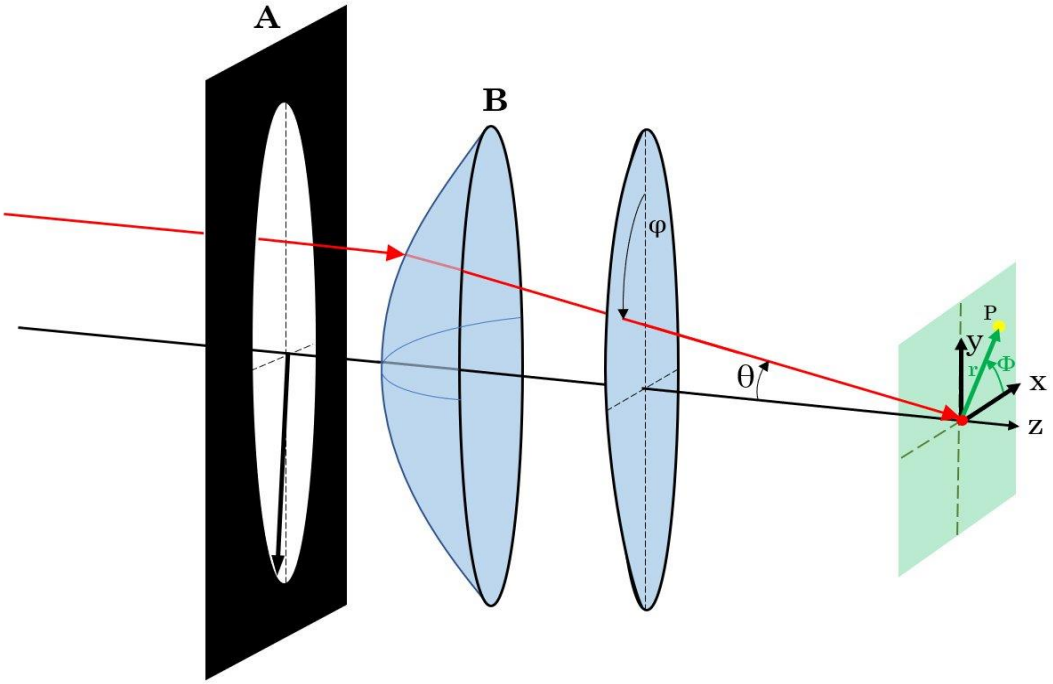

Figure 3.1: Coordinate system for calculating the Debye integral.

Collimated light enters the imaging system (objective lens) at the normal to the aperture **A** before being diffracted by a focusing element and focused to a point along the axis of the lens. The surface at **B** is termed the 'reference sphere' and is a portion of a sphere centred at the focus of the lens (red spot) with radius equal to the focal length of the lens. The Debye integral calculates the magnitude of the electric field at a point $P(r,\Phi,z)$ whose position is given in cylindrical coordinates relative to the centre of the focus of the incident beam. The integral is taken over the values of θ and φ which define all the portions of the beam that are focused. The resolution limit of the system is defined by the maximum permissible value for θ, or equivalently the radius of the aperture **A**.

However, for a more detailed model of the PSF, the phase, polarisation and beam intensity profile at the back of the lens must be considered. To do this, a vectoral approach must be taken, breaking down the electric field of the focused light into three orthogonal components, with the total intensity being the square of the sum of the components, i.e. $\vec{I} = \vec{E}^2 = |\vec{E}_x|^2 + |\vec{E}_y|^2 + |\vec{E}_y|^2$. The individual components of the electric field are calculated using the Debye diffraction integral with the coordinate system shown in figure 3.1. Using this, the electric field components of $\boldsymbol{E}$, at a point

$P(r, \Phi, z)$, relative to the focal point of the lens, is calculated using the Debye integral:

$$\begin{bmatrix} \vec{E}_x \\ \vec{E}_y \\ \vec{E}_z \end{bmatrix} = \int_{\varphi=0}^{2\pi} \int_{\theta=0}^{\alpha} \mathrm{A}(\theta, \varphi)\mathrm{P}(\theta, \varphi)\sqrt{\cos\theta} \begin{bmatrix} \vec{p}_x \\ \vec{p}_y \\ \vec{p}_z \end{bmatrix} \times \exp[ik(r\sin\theta\cos(\varphi - \Phi) + z\cos\theta)]\sin\theta \ \mathrm{d}\varphi\mathrm{d}\theta \qquad \text{Eq. 3.1}$$

Here $\mathrm{A}(\theta, \varphi)$ and $\mathrm{P}(\theta, \varphi)$ are, respectively, the amplitude and phase of the incident beam at a point on the 'reference sphere'. The $\sqrt{\cos\theta}$ term is the apodisation of the objective lens, assuming it satisfies the sine condition. k is given by $k = n2\pi/\lambda$ where n is the refractive index of the imaging medium and λ is the wavelength of light. The resolution limit of the lens is represented by an upper limit of the value for θ, given by $\arcsin(\mathrm{NA}/n)$. The matrix $[p_x; p_y; p_z]$ describes the polarisation vector of the incident beam in the (θ, φ) coordinate system and changes depending on the polarisation of the incoming beam.

In optics, PSF engineering has been used extensively in a number of fields ranging from cold atom-trapping[59] to astronomy[60]. In microscopy, PSF engineering has also been applied to a number of techniques, altering both the excitation and detection PSFs. The most obvious example of PSF engineering is STED microscopy (chapter 2) where the PSF is engineered to form a doughnut, used as the depletion beam. This is generated either by applying a phase change to the beam, i.e. altering $\mathrm{P}(\theta, \varphi)$ in equation 3.1, or through using an azimuthally polarised beam[9], i.e. choosing a value for $[p_x; p_y; p_z]$ such that the focal spot has a central zero-intensity minima. Another prominent example of PSF engineering is 3D SMLM techniques using engineered detection PSFs.[61,62]

3.1.2 Difference microscopy

Difference microscopy, also known as Fluorescence Emission Difference (FED)[63] or Switching Laser Mode (SLAM)[64] microscopy, describes a range of super-resolution techniques, conceptually similar to STED microscopy. Where STED microscopy uses a doughnut beam to quench fluorescence outside of a small focal volume, 2D-FED microscopy aims to achieve the same effect by comparing the images acquired under different sample illumination schemes. To achieve this, the sample is raster scanned twice, firstly with a Gaussian and then with a doughnut beam. At every scan position, the difference between the measured signals mimics fluorescence emission only in the central dark spot. The final super-resolution image is reconstructed by performing a weighted subtraction of the image acquired under doughnut illumination from that acquired under Gaussian illumination, i.e.

$$I_{FED}(\vec{r}) = I_{Gauss}(\vec{r}) - \alpha I_{Doughnut}(\vec{r}). \qquad \text{Eq. 3.2}$$

The weighting factor, α, determines the strength of the subtraction, with higher resolution achieved with a higher value of α. In practice, the value of α must be chosen to give the highest possible resolution without introducing unwanted artefacts. Often, this choice depends on properties of the imaging system. In ideal imaging conditions, where the system perfectly reflects theoretical models, very large values of α (i.e. $\alpha > 1$), could be used to give the highest resolutions. In practice, however, imaging systems deviate from this ideal model through the introduction of aberrations. For example, aberrations which deform the shape of the doughnut PSF can lead to an off-centre minimum in the doughnut. This, in turn, would result in subtraction of fluorescent signal from the centre of the excitation PSF, reducing SNR and effectively amplifying low resolution and out-of-focus signal. While proper alignment and high-quality optics can minimise these effects, the varying optical properties of biological samples mean ideal imaging conditions can rarely be met. Because of this, artefacts from subtraction will always be present in the subtracted image. Choosing

a lower value of α is a method of reducing the impact aberrations on the final image and in biological imaging values of α are typically in the range $0.3 - 0.6$.

3.1.3 Theory of enhanced multi-spot structured illumination microscopy

While FED microscopy offers a resolution improvement over diffraction-limited systems, there is inherent structured-illumination information that is lost during FED image reconstruction. eMSIM offers an improvement over MSIM in two key ways. The first way is making the structured-illumination information obtained under illumination by the doughnut PSFs available for resolution enhancement. The extra structured-illumination information over MSIM can be seen through analysis of the two PSFs used in FED. By evaluation of the Debye integral (equation 3.1), doughnut PSFs were calculated for left circularly-polarised excitation light with a spiral phase. Gaussian PSFs were generated by performing the Debye integral for left circularly-polarised light with no phase change imposed. The choice of handedness of the polarisation affects the minima of the doughnut PSF, and must be chosen to ensure a zero at the centre of the focus.[9] The polarisation must be matched to the direction of the spiral phase added to the beam. Left-handed polarisation was used to match the anticlockwise direction of the spiral phase $\mathrm{P}(\theta, \varphi)$ in equation 3.1. As such, the polarisation matrix was taken as:

$$\begin{bmatrix} p_x \\ p_y \\ p_z \end{bmatrix} = \begin{bmatrix} \cos\theta + 1 + (\cos\theta - 1)\exp i2\phi \\ i(\cos\theta + 1) - i(\cos\theta - 1)\exp i2\phi \\ -2\sin\theta \exp i\phi \end{bmatrix} \qquad \text{Eq. 3.3}$$

The cross sections of these PSFs are shown in figure 3.2. Looking at the cross sections, the Full-Width Half Minima (FWHMi) of the doughnut is smaller than the FWHMa of the Gaussian beam. This means the internal edges of the doughnut are steeper than the outer edges of the Gaussian.

As in SSIM, steeper edges in the excitation pattern result in more structured-illumination information being made available.

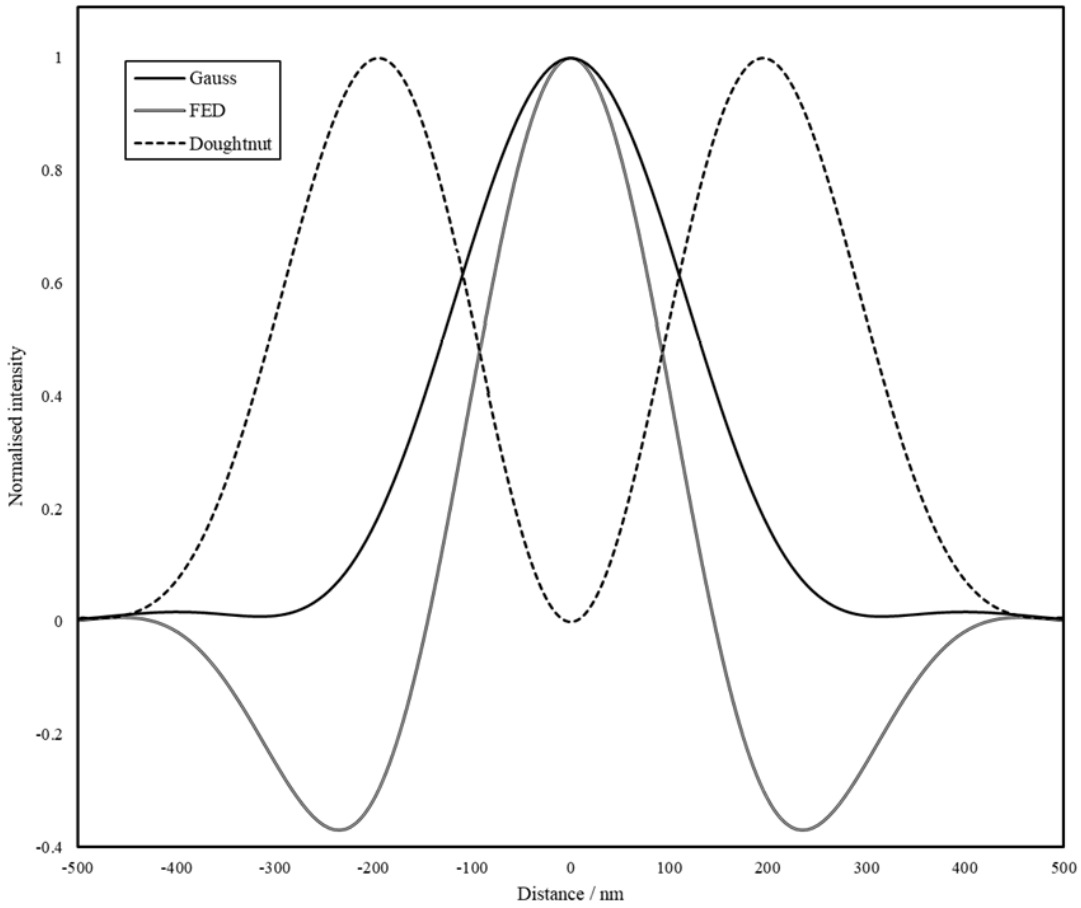

Figure 3.2: Profiles of the doughnut and Gaussian PSFs.

x-y sections through doughnut and Gaussian excitation PSFs. PSFs were calculated for a wavelength of 488 *nm*, objective NA of 1 and refractive index 1.518. Solid line: Gaussian PSF. Dashed line: Gaussian PSF. Double line: FED PSF calculated with a subtraction factor $\alpha = 0.5$. Green arrow shows the FWHMa of the doughnut PSF. Red arrow shows the FWHMa of the Gaussian PSF.

The second way eMSIM offers an improvement over MSIM is in the initial estimate of the sample structure. With MSIM, the acquired diffraction-limited image acts as the approximation used in image deconvolution. While in theory this is sufficient to extract the super-resolution information, in practice, using the diffraction-limited approximation limits the ability of the reconstruction algorithm. Starting from a better estimate of the sample will always result in an improved

MLD reconstruction. In contrast, eMSIM uses the super-resolution FED image as an initial estimate of the sample structure.

3.2 Simulated eMSIM imaging

To verify the efficacy of the eMSIM technique, simulated imaging was carried out *in silico*. Such *in silico* tests allowed for the testing of the technique in a controlled environment. As well as this, they offer a chance to develop the image processing software needed for eMSIM in an artefact-free environment where the true structure is known. This is preferable to real-world tests as resolution improvement can be more precisely measured and the result compared to the underlying structure to ensure that any resolution improvements seen are genuine.

3.2.1 Defining the point-spread function

The first step of simulating an imaging system is to define the properties of that system: for eMSIM image simulations, this involves defining the excitation and detection PSFs.[9] Determining the excitation PSFs was achieved by evaluating the Debye integral in MATLAB assuming left-circularly polarised light, matched to the direction of the spiral phase change to ensure a central zero. Incoherent detection PSFs were calculated using the Born Wolf model,[65] implemented in the PSF generator ImageJ add-on.[66] PSFs were generated for an objective NA = 1.4, and excitation and emission wavelengths 488 nm and 515 nm respectively, simulating the common fluorophore Alexa-Fluor 488. The PSFs were assumed to be constant across the pattern as is expected for high quality objectives and the limited FOVs simulated.

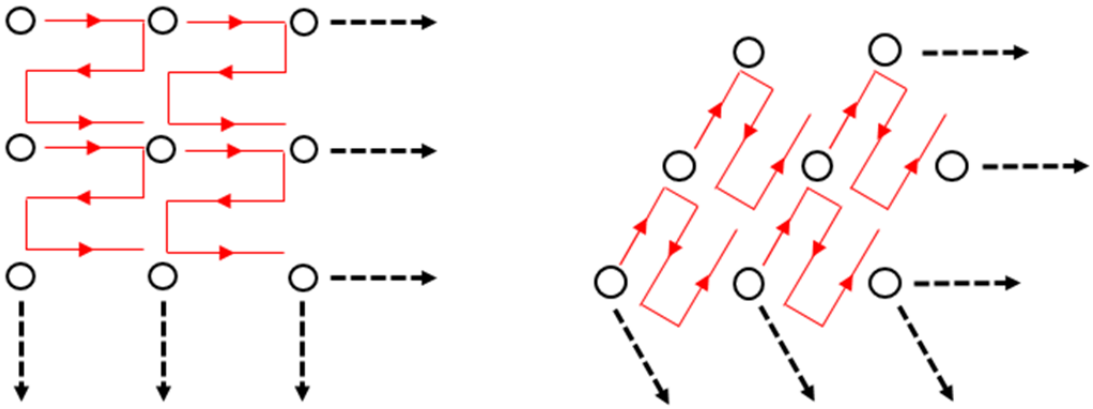

Figure 3.3: Square and diamond excitation patterns.

Left: square grid pattern. Right: diamond grid pattern. While the diamond grid allows for equal spot spacing, determining the spot separation is computationally more challenging.

3.2.2 Building excitation patterns

The ideal excitation patterns were generated by inserting model PSFs at regular intervals in the excitation image. From one pattern, the stack of shifted frames was generated by shifting the first frame by regular intervals. For these ideal patterns, uniform illumination was guaranteed by separating the PSFs by the number of pixels equal to the number of shifts in each direction. In MSIM, there are two different pattern separations commonly used: square and diamond patterns (See figure 3.3). During early testing, both of these styles of pattern were tested, and no noticeable difference was found between either their performance or the minimum PSF separation that could be used. Because of this, square patterns were chosen to simplify pattern estimation in later work.

3.2.3 Building model data

Using the image formation process detailed in equation 2.1, raw data was generated by multiplication of the sample with the excitation pattern and subsequent convolution with the detection PSF. To more accurately

represent imaging systems, Gaussian and Poisson noise were added to the simulated images. To speed up this step, the program was parallelised to run on the Graphical Processor Unit (GPU). Performing all possible steps of the image processing on the GPU in total offered over a 60 times speed improvement over the same processing running on the CPU.

3.2.4 Recovering super-resolution image

As discussed in Chapter 2, there are a number of available methods to reconstruct the final super-resolution information. Pixel reassignment, JRL and PIFP were all tested as reconstruction techniques. For pixel reassignment, the first step was to extract the co-ordinates of the maxima from the excitation pattern. It is important to extract the co-ordinates from the ideal pattern rather than the data as the local maxima in the raw data will not necessarily align with the location of the excitation spot. Since pixel reassignment is based on the theory of overlapping excitation and emission PSFs, the shrinking must occur around the centre of the excitation PSF. The process used to find the maxima is shown in figure 3.4

This basic process to find peaks in noisy data is based on the earliest algorithms developed to rapidly process SMLM images. An alternative approach to extracting these coordinates would be to save the location of each inserted PSF when the patterns are first generated. While this may be more computationally efficient, the above method can be run exclusively on the GPU. When run on the GPU, computation time is roughly 20ms per image and the whole process contributes negligibly to total processing time.

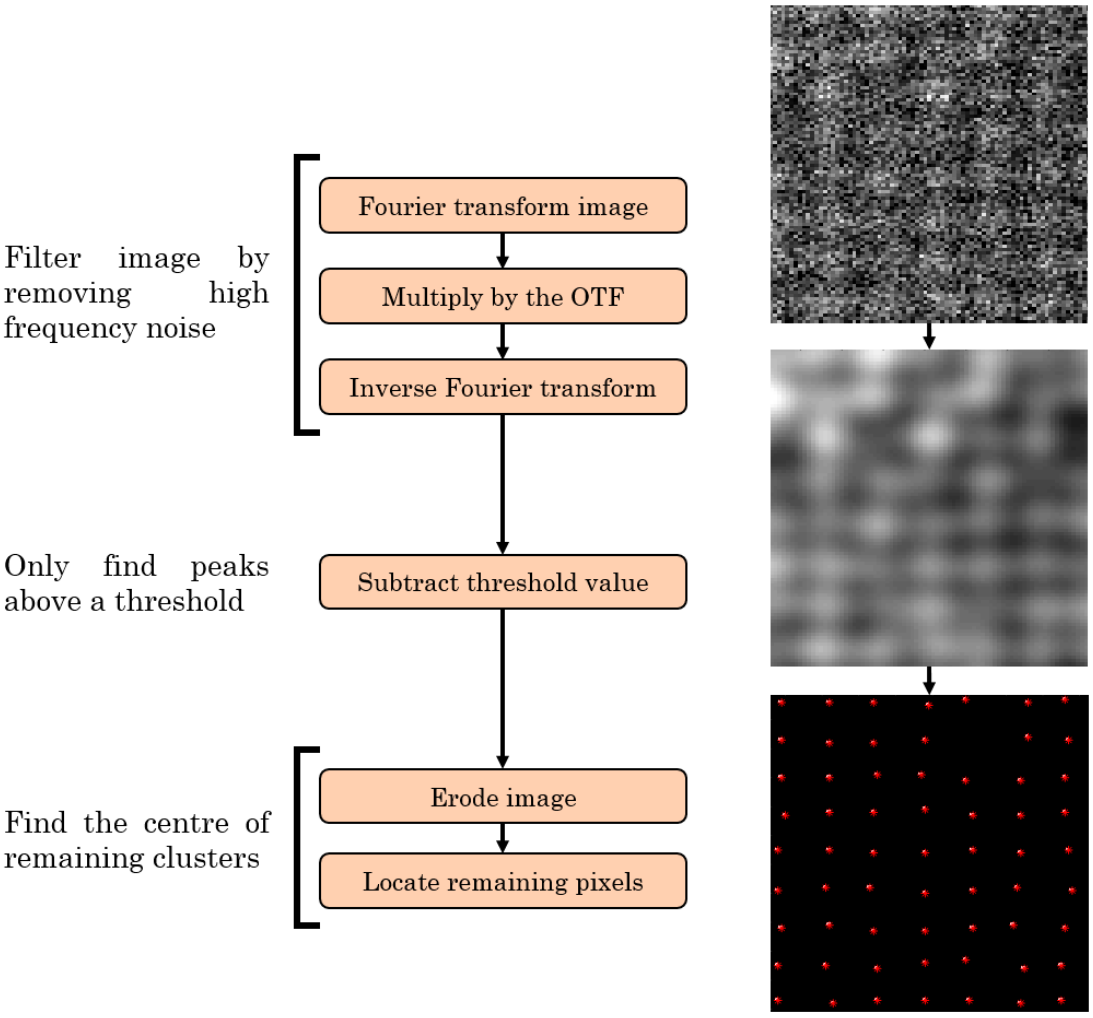

Figure 3.4: Workflow for peak finding program.

Left: Diagrammatic workflow with steps for algorithm. Right: Intermediate results. In the first step, the raw image (top right) is filtered to remove high frequency noise. Next, a background is subtracted to prevent unwanted low intensity peaks (middle right). Finally, the local maxima in the image are found through image erosion, i.e. clusters of high intensity pixels are reduced to a single pixel. The location of these pixels is then extracted (bottom right).

From these local maxima, the pixel reassignment (and pinholing in real-world data) can be performed. To achieve this, a small square of pixels is extracted at the coordinates found by the maxima program. This small image is then optionally multiplied by a pinhole and downsized by a pre-determined scale factor. The smaller image is then inserted into a running total image at the same coordinates from which it was extracted. Since each step of this process depends on the previous step, and since spots cannot be processed in parallel, the code cannot be accelerated using the GPU and as such, takes several minutes to run on the CPU.

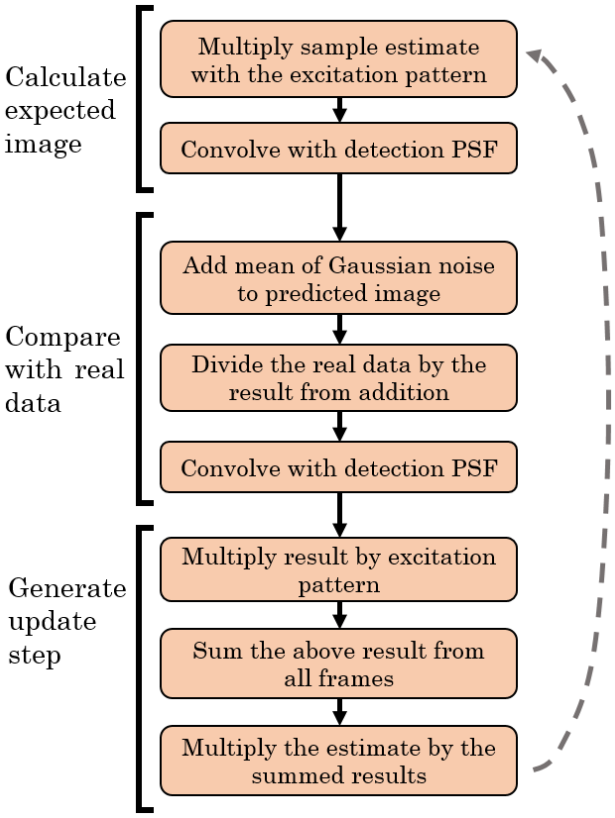

Figure 3.5: Workflow for JRL algorithm.

The first step of the JRL process is to calculate the expected image through convolution of the estimate of the sample with the detection PSF. Next, a comparison is made with the acquired data, and from this comparison, an update step is generated and applied to the estimate of the sample. This process is iterated either for a fixed number of loops or until a stopping criterion (e.g. magnitude of applied update) is reached.

For the iterative deconvolution methods JRL and PIFP, GPU processing was possible in parts of the code. While the individual iterations depended on previous ones, the update step at each iteration could be calculated in a parallelised fashion, computing the contributions to the step from each

image simultaneously. Because of this, JRL and PIFP had significantly improved performance over pixel reassignment.

Looking at equations 2.14-2.16 which defines the PIFP process, the estimate of the image is changed after every frame that is processed. This means that it cannot be accelerated by processing frames in parallel. Because of this, the PIFP process also requires a large number of variables to be stored in each iteration, making the code more complex and increasing memory requirements. Given the modest memory capacity of the GPU used, this meant that the PIFP algorithm also had to be performed on the CPU, greatly extending computation time. On average, a PIFP iteration took five times as long as a JRL iteration for a 512x512 image although the difference in iteration time further increased for larger image sizes.

3.3 Results

During simulated imaging, three resolution targets were used to demonstrate resolution improvement: a Siemens star, a resolution bar target and point emitters. In addition to real space image analysis, Fourier analysis was used to provide a quantitative measure of resolution. Analysing super-resolution techniques in frequency space has the advantage that measurements are less susceptible to noise or variation of resolution across the FOV. As the resolution limit is governed by extent of the OTF in frequency space, resolution can be quantified as the highest spatial frequency the imaging technique can recover from the sample.[67] To measure this, two images of the same region are captured, and the correlation of their Fourier transforms is measured.[68] This measurement is calculated as a function of distance from the centre of the OTF in frequency space from[68]:

$$\mathrm{FRC}(r) = \frac{\sum_{x,y\in r} F_1(x,y)\cdot F_2^*(x,y)}{\sqrt{\sum_{x,y\in r}|F_1(x,y)|^2 \sum_{x,y\in r}|F_1(x,y)|^2}} \,. \qquad \text{Eq. 3.4}$$

Here, r is the distance from the centre of the OTF. The sum is taken over all pixels in the Fourier transforms – with coordinates (x, y) – that lie on the ring at a distance r from the centre of the OTF. $F_1(x, y)$ and $F_2(x, y)$ are the complex Fourier transforms of the two images acquired. As the underlying sample frequencies are the same for both images, high correlation between the two Fourier transforms indicates that spatial frequencies at this distance from the centre of the OTF have been well recovered. As the distance from the centre of the OTF increases, the correlation between the two Fourier transforms reduces, as random noise (which is different for both images) has an increasing contribution to the measured spatial frequencies. This is shown in figure 3.6. The extent of the OTF, and therefore the resolution limit, can be considered as the maximum distance from the centre before the correlation falls below a certain value. This value is a function of the number of pixels that lie on the ring at the measured radius, and represents the deviation in the correlation that would be expected for random pixel values. This is calculated as

$$\sigma = \frac{\mathrm{S}}{\sqrt{N_r/2}}, \qquad \text{Eq. 3.5}$$

where S is the deviation factor and N_r is the number of pixels that lie on the ring at the distance r from the centre of the OTF. The values for S are chosen to determine the extent that the FRC curve must stay above the random correlation. Typically, vales of 3 and 5 are chosen and the correct value is a subject of dispute.[68] An example of this is shown in figure 3.7. As the FRC is often quite noisy, it is calculated at rings with a thickness of ± 2 pixels in the Fourier transform. A spline fit is then applied to the FRC curve to calculate, with sub-pixel resolution, the point at which the sigma curve crosses the FRC. From this value, the resolution limit is calculated as the inverse of the spatial frequency according to the definition of the Fourier transform.

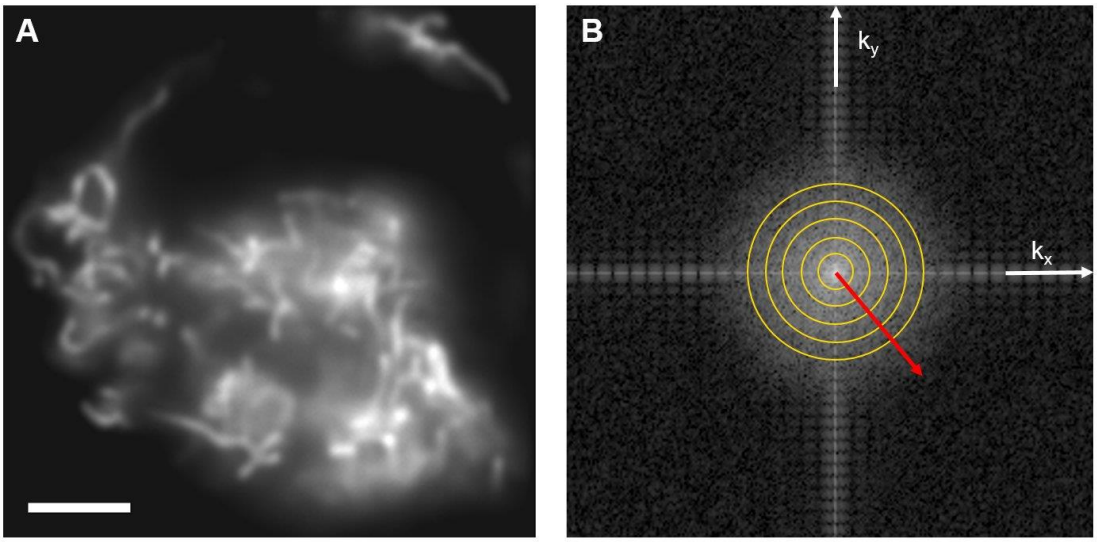

Figure 3.6: Method for measuring resolution in frequency space.

A: Example diffraction-limited image of fluorescently tagged mitochondria in fibroblast cells. Scale bar is 5 μm. B: 2D Fourier transform of A. The yellow lines show rings of constant radius from the central point, i.e. the lowest spatial frequency in the image. For each ring around the centre, the correlation between the Fourier transforms of two images of the same sample is measured. As the intensity of the OTF drops off, random noise contributes increasingly to the values of the Fourier transform. This can be seen in the Fourier transform of a single image (above) as a drop in intensity as the distance from the centre point increases. The vertical and horizontal lines along the axes of the Fourier transform are artefacts resulting from the square boundary of the image. As this is constant in both images, it contributes negligibly to the FRC measurement.

3.3.1 Reconstruction techniques

The first step of simulations was to test the reconstruction techniques used. Figure 3.7 shows FRC curves for the reconstructions: pixel reassignment (as is used in ISM); PIFP; JRL; and a sequential combination of JRL and PIFP deconvolution. The reconstructions were performed on the Siemens star to calculate the FRC curves. eMSIM data was generated using PSFs calculated for 488 nm excitation and a subtraction weighting of 0.5. Overall, PIFP on its own was the worst-performing reconstruction method used. Furthermore, while pixel reassignment outperformed PIFP,

it was found that a sequential combination of PIFP and JRL provided the optimal results, in agreement with previous work.[45]

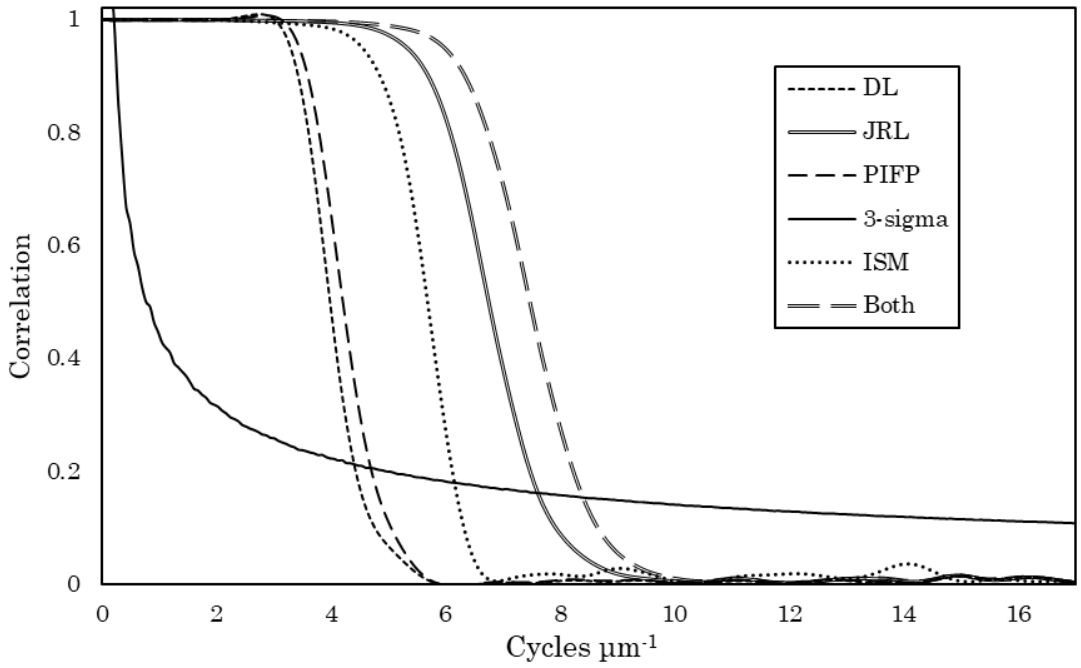

Figure 3.7: FRC measurements of reconstruction methods.

Tight dash: diffraction-limited image. Large dash: MSIM reconstruction using PIFP. Dotted line: ISM reconstruction using pixel reassignment. Double line: JRL reconstruction. Double dash: Combination approach using JRL seeded with PIFP. Solid line: 3σ resolution criterion curve. Reconstruction used 10 PIFP iterations and 3 JRL iterations.

3.3.2 Resolution improvement in eMSIM

The final stage of testing was to make a comparison of resolution improvements in MSIM/eMSIM. Figure 3.8 shows imaging results of a bar target in a medium noise environment. The simulated data was generated using PSFs calculated for 488 *nm* excitation and a subtraction weighting of 0.5. Viewing the target, both MSIM and eMSIM have offered an improvement over diffraction-limited imaging. This is more apparent on the image of the smallest bars. eMSIM has been able to resolve the three smallest bars, as well as give better definition of the number 6. An improvement in contrast and brightness is apparent when looking at the wider targets. For example, the square block on the wider image and the upper part of the 2 on the zoomed image are both brighter and clearer in the eMSIM reconstructions compared to the MSIM images.

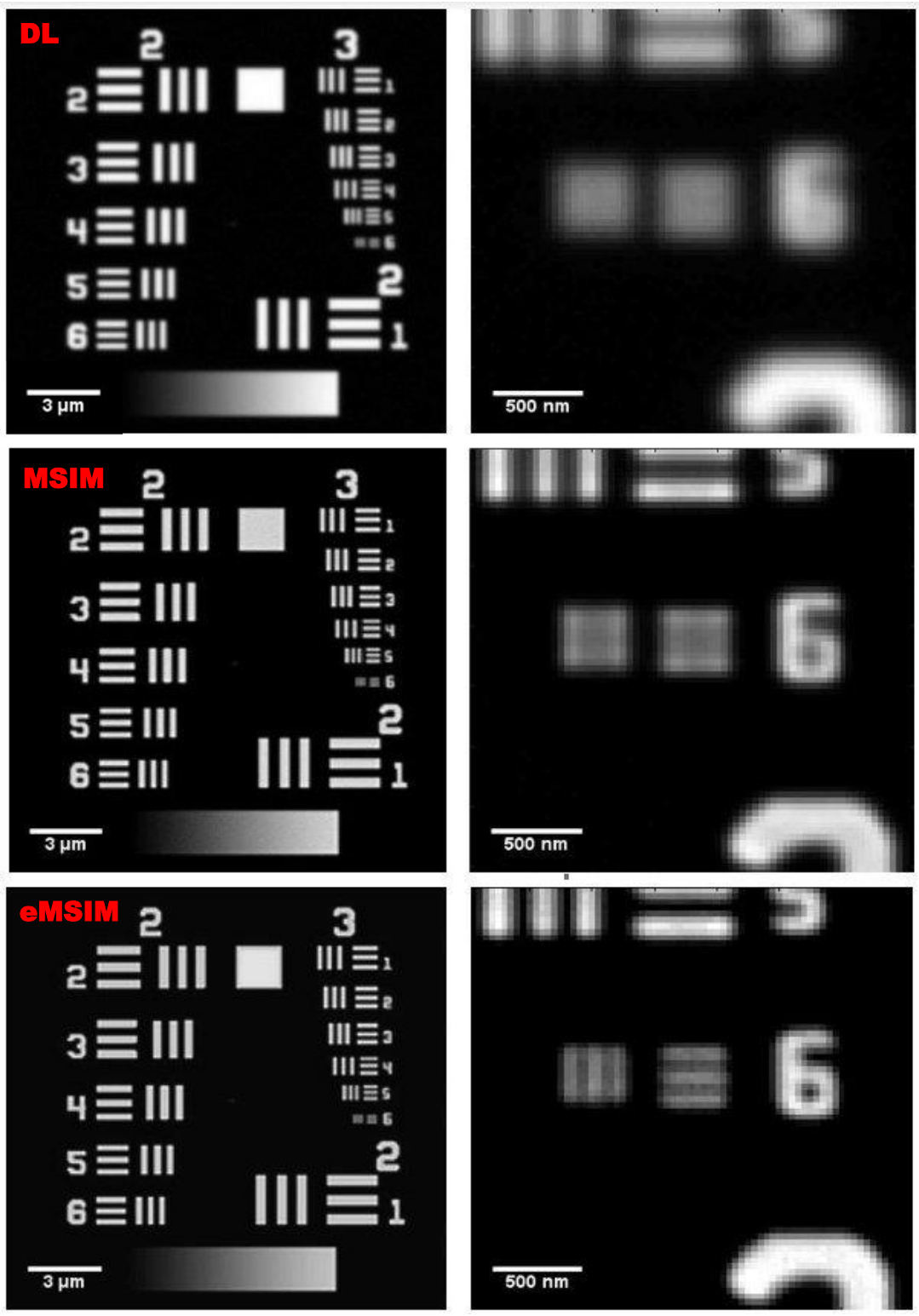

Figure 3.8: Bar target.

Top pane: Diffraction-limited image acquired under low noise levels and zoomed image of smallest resolution bars. Middle pane: MSIM image and zoom of smallest bars. Bottom pane: eMSIM image and zoom of smallest bars. Images were simulated assuming illumination with 488 *nm* excitation and objective NA of 1.4 Adapted from Ward et al. 2018

Figure 3.9 shows the results of MSIM/eMSIM imaging on the Siemens star. The simulated data was generated using PSFs calculated for 488 *nm* excitation and a subtraction weighting of 0.55. The Siemens star is formed from radial spokes which decrease in thickness towards the centre of the target. The resolution is estimated from the minimum separation of the spoke which can still be resolved.

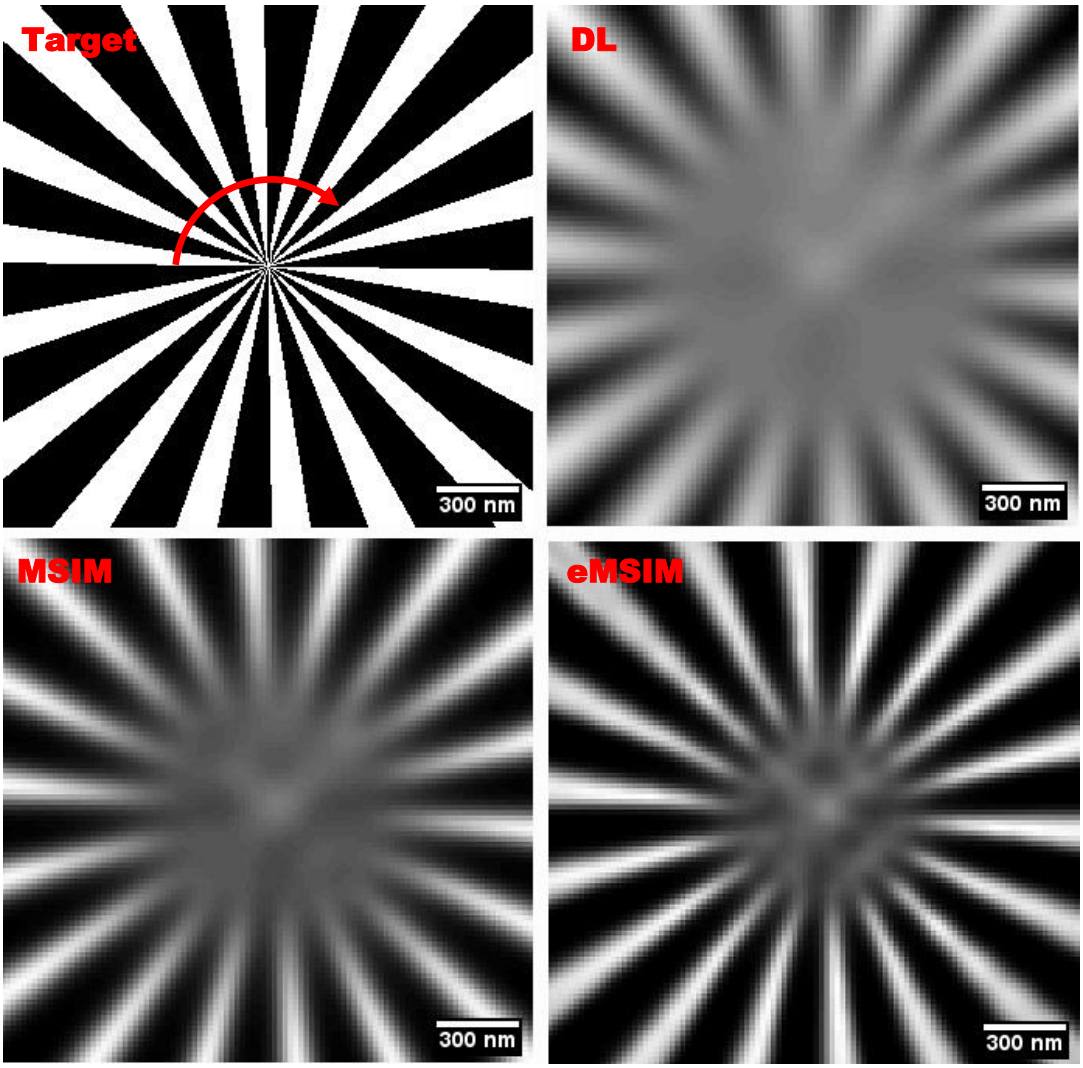

Figure 3.9: Siemens star.

Top left: Ground-truth sample used. Top right: Diffraction-limited image. Lower left: simulated. Lower right: eMSIM image. The spokes are clearer closer to the centre in the eMSIM image, suggesting increased resolution over MSIM. Also visible is the increased brightness and contrast of eMSIM over MSIM. The red line shows the path of the intensity profile measurements used to estimate the resolution.

From the images, eMSIM has resolved closer into the target than both MSIM and diffraction-limited imaging. Line profile measurements were taken at the minimum distance from the centre at which eMSIM was able

to resolve the spokes by the Abbe criteria (i.e. a halving in intensity between the maxima and minima). The red line on the target indicates the direction and path used for the intensity measurement shown in figure 3.10. From the intensity profile measurements, eMSIM has resolved spokes with an 80 *nm* separation.

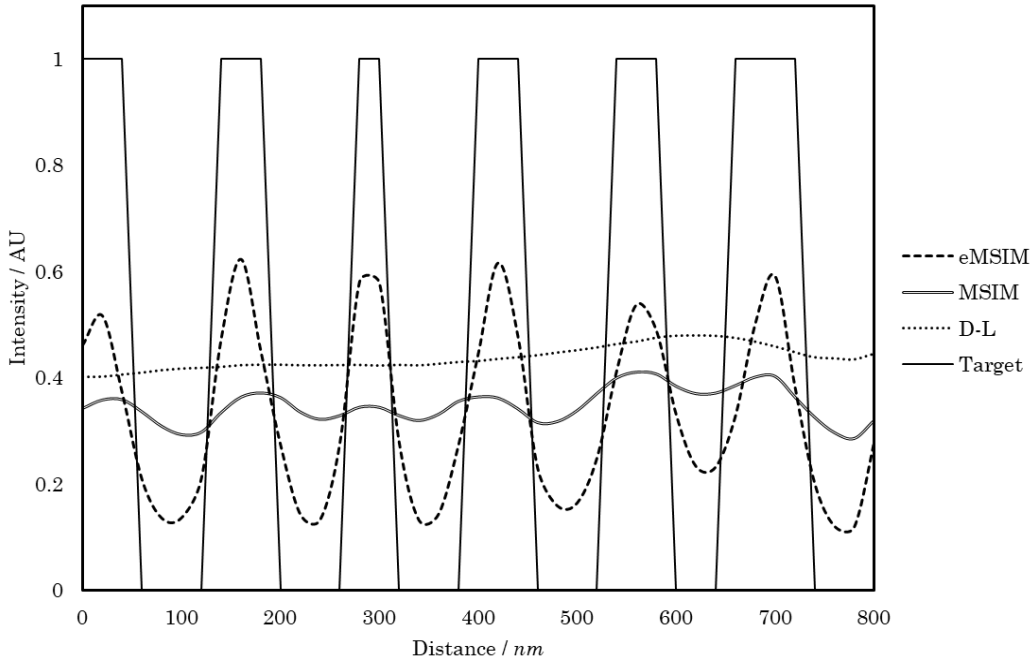

Figure 3.10: Siemens star intensity plot.

The lines show the relative intensities along the red lines on figure 3.8. At this distance from the centre, eMSIM has been able to resolve the spokes of the star pattern where MSIM has not. The minimum resolved distance between the spokes on the target was 80 *nm*.

For measurements at increasing distance from the centre, the resolution of MSIM was estimated as 120 *nm* and diffraction-limited imaging as 200 *nm*. These estimated resolutions are below those theoretically possible according to the Abbe limit, as a result of the simulated noise degrading the images. The impact of noise can further be assessed by comparing the FRC curves for the imaging techniques (figure 3.11).

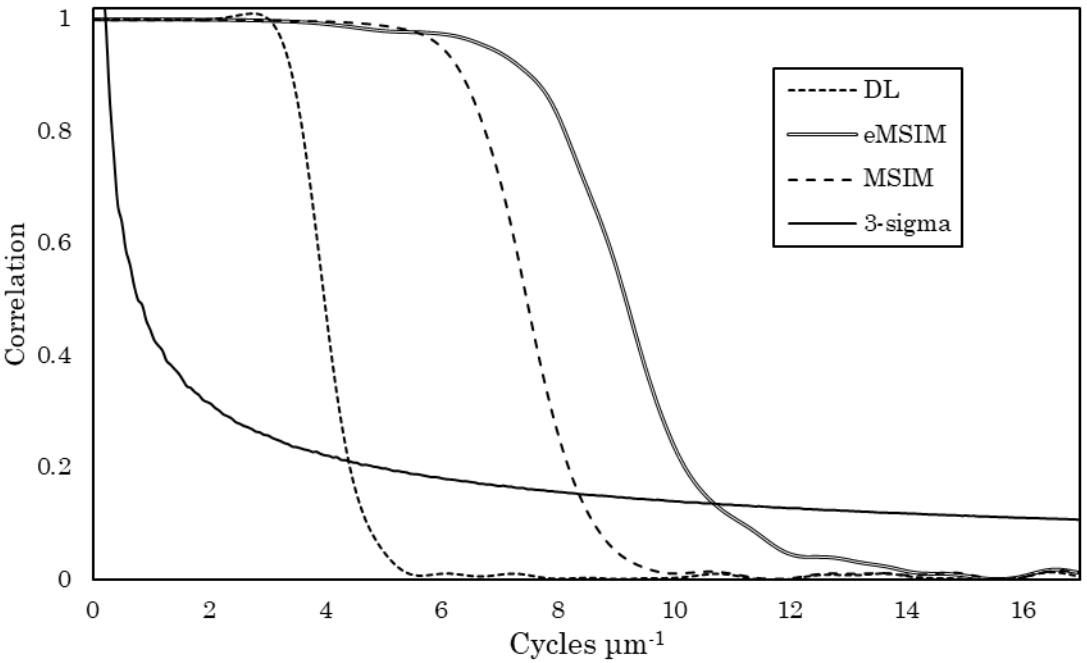

Figure 3.11: Reconstruction FRC curves with different techniques.

FRC curves for different super resolution methods. Solid line: 3σ curve. Narrow dash: diffraction-limited imaging. Double line: eMSIM imaging. Wide dash: MSIM reconstruction. Reconstruction was performed using 25 PIFP iterations, 10 JRL iterations and a subtraction factor of 0.55.

From the FRC data, the resolution was calculated from the intercept with the 3σ curve. The quantitative results are summarised in table 1.

Table 1: Quantification of resolution improvement

Imaging method	**3σ intercept / cycles µm^{-1}**	**Resolution / *nm***
Diffraction-limited	4.42	226
MSIM	8.39	119
eMSIM	10.7	93.5

As expected, the resolution estimated using the FRC curves is below that predicted by the Abbe limit. This reflects how noise degrades the effective resolution of the system.

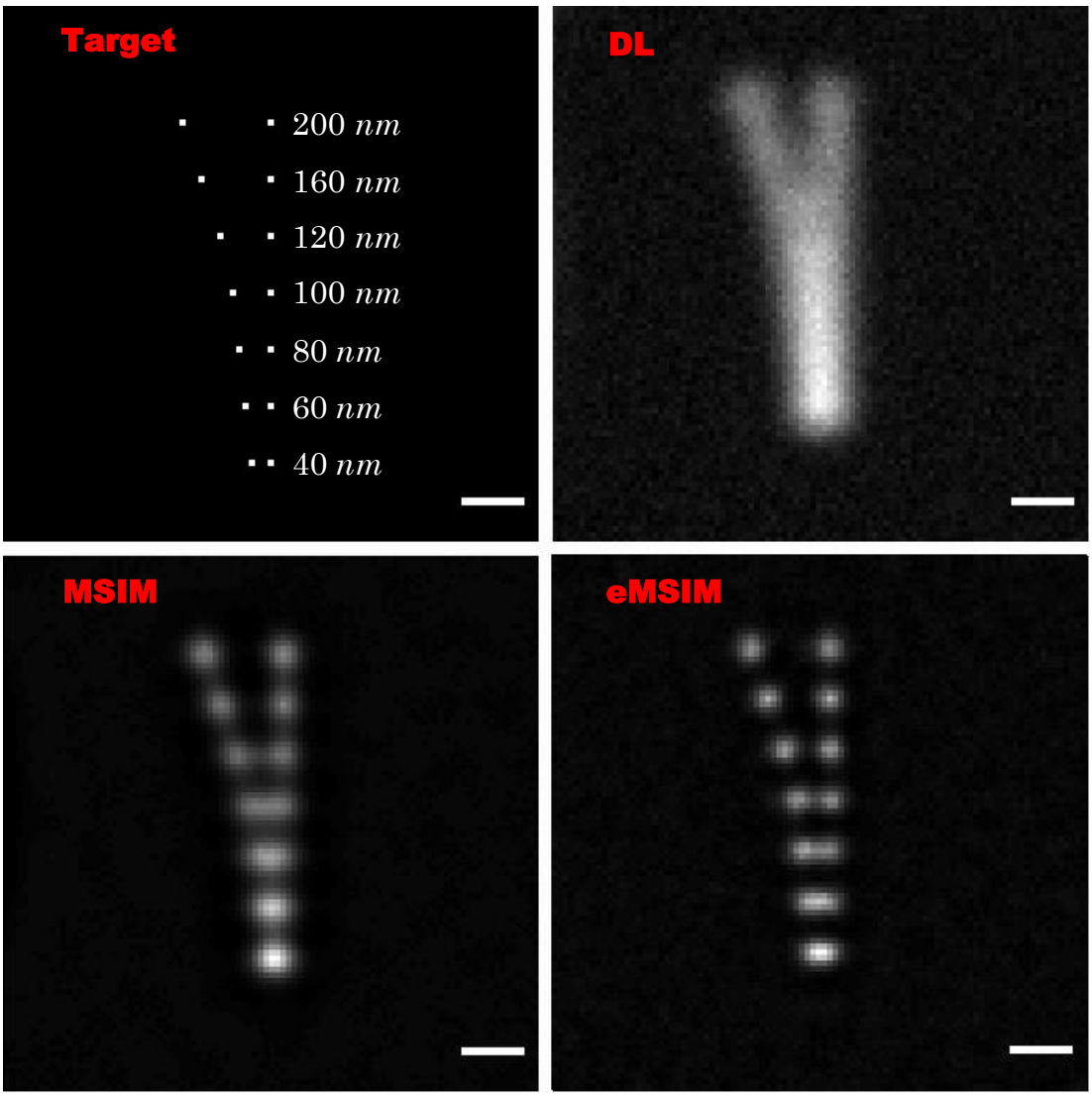

Figure 3.12: Comparison of imaging techniques on point sources.

Top left: ground-truth sample with the point source spacing indicated/ Top right: diffraction-limited (DL) image. Bottom left: MSIM image. Bottom right: eMSIM image. Reconstruction was performed with 10 JRL and 25 PIFP iterations. Scale bar is 200 *nm*.

The final resolution target was a cluster of point emitters. These results are shown in figure 3.12. For this reconstruction, more JRL iterations were used than in previous reconstructions, as JRL shows improved performance over PIFP on point sources. The resolution increase of eMSIM over the diffraction-limited images and MSIM images is apparent, as point sources with a smaller separation have been resolved. Based on the separation, eMSIM has successfully resolved point sources with a separation of 100 *nm* which defines an upper bound on the resolution, in agreement with the FRC predictions. The MSIM reconstruction has successfully resolved sources with a separation of 120 *nm*, also in

agreement with FRC predictions. Again, as with the FRC predictions, the resolutions are worse than those predicted by the Abbe limit, reflecting the influence of noise on imaging resolution. Simulated diffraction-limited imaging has, however, been able to resolve point sources with a separation of 200 *nm*, better than predicted by FRC. This could be a result of the high noise levels skewing the FRC measurements, as MSIM and eMSIM also offer some denoising as well as resolution improvement. Additionally, the resolution estimates from the point sources are below those predicted by the Siemens star. This is due to the fact that the point sources, as single emitters, provide less signal than the larger spokes of the Siemens star, and consequently the sample's spatial frequencies are harder to detect above the random noise. This is apparent in figure 3.12, where the contribution from the background noise is stronger than in figures 3.8 and 3.9.

3.4 Summary

Both the real-world and frequency space measurements demonstrate the improved resolution of eMSIM imaging on all the targets used. Each target and resolution estimation method gave different resolution approximations for each technique, and a resolution improvement of 1.2 – 1.5 times that achievable with MSIM.

The advantage of increasing the resolution using PSF engineering rather than non-linear methods is the flexibility. eMSIM requires only twice as many exposures over MSIM and no increases in illumination intensity, minimising phototoxicity to maintain compatibility with live-cell imaging. Despite these advantages, eMSIM suffers from the disadvantage that multi-spot and multi-doughnut patterns must be projected and shifted quickly. While there are simple ways to achieve MSIM projection using Spatial Light Modulators (SLMs), these setups are often incompatible with simple swapping between spots and doughnuts; generating the doughnuts

requires phase engineering the beam while traditional SLM setups permit only amplitude modification of the light. To get around this, a new technique for SIM pattern projection was constructed, based on holographic projection (described in Chapter 4).

4. Holography

Summary: *this chapter introduces the concept of holography in optics for pattern projection. It describes the essential components for holographic projection and builds on this to describe how the use of holographic projection may provide significant new opportunities in structured illuminations. This chapter also details the use and testing of holography throughout this project.*

4.1 Introduction

For many years, high intensity, tightly-focused laser beams have been used in the field of optical trapping.[69][70] With a high light intensity, it is possible to exert pico-Newton forces on objects in the focal spot through momentum transfer between from the light to the trapped object.[71] These 'optical traps' or 'optical tweezers' have found many uses across a wide range of fields. In biological studies they can be used for the direct manipulation and movement of cells, [72][73] as well as particle sorting and

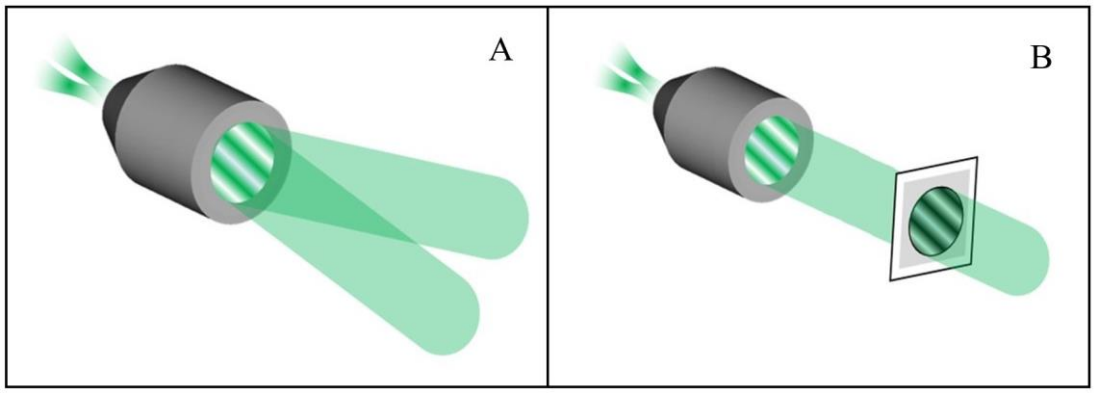

Figure 4.1: Concept of holography.

A: If two beams enter the back of an objective at different angles they focus to different points in the focal plane. At the back of the objective this generates an interference pattern in the phase of the beams. **B**: By applying the same phase to a single beam entering an objective, the focus of the beam mimics the behaviour of the original two beams.

measurement of microscopic forces.[74] For more complicated optical trapping experiments, multiple particle traps are required to study the behaviour of interacting targets. Early experiments generated the multiple

traps by deflecting a single beam using one or more mirrors and briefly switching the laser on at each trap location, giving the illusion of multi-trap patterns.[75] However, as experimental demands grew, a new technology was required to generate a greater number of more dynamic traps. Avoiding the limitations of the mechanical movement of mirrors, beam steering can be achieved using Electro-Optical Deflectors (EODs)[76] and Acousto-Optical Deflectors (AODs)[77][78] which offer a faster mechanism to steer the single beam. However, the use of a single beam to generate multiple traps is still limited by the fact that the trapping force is not constant throughout the experiment as each trap only experiences the trapping force of the laser for a brief period of time. The use of holography for pattern generation arose to address this issue by offering a way to simultaneously generate multiple traps from a single beam.[79] Figure 4.1 shows the basic principle of holography. When multiple off-axis beams enter the back of an objective, there is an interference pattern in the phase of the beams at the back focal plane. Using holographic techniques, the same phase patterns can be imparted onto a single beam to mimic the behaviour of the original beams. Holography involves calculating the required phase patterns (kinoforms) and applying these to a single focused beam.[80] For pattern projection in MSIM, amplitude-only modulation (Chapter 5.1) is typically used to generate the multi-spot patterns. Briefly, in amplitude-only modulation, an SLM is imaged onto the focal plane of the sample and uniformly illuminated with excitation light. Each spot in the projected pattern corresponds to one active pixel on the SLM. The disadvantage of this method of projection is the efficiency. For a 15:1 spot separation, only 0.4% of the excitation light is used at any one time. In contrast, holography is typically 50-80% efficient, meaning simpler and cheaper light sources can be used. In addition to this, most PSF engineering and aberration correction techniques require phase modulation of the focused beam, and this can be combined with the holograms to apply the same engineering to multiple PSFs simultaneously.[79][81] Such modifications of the beam to engineer PSFs as well as generate spot patterns have proved exceptionally useful in the field

of optical trapping. For example in trapping experiments, PSFs whose phase has been engineered to have non-zero orbital angular momentum can be used to rotate particles confined in the optical traps.[82] For this project, holography offers an attractive method for pattern projection as the simple optical configuration and the ease of PSF engineering greatly simplify the process of generating multi-spot and doughnut excitation grids.

4.2 Hologram calculation

One of the most challenging steps in holography is reliably calculating the necessary holograms. The efficacy of hologram calculation methods is measured by the efficiency (e) and percentage standard deviation (σ) of the pattern generated. The efficiency is a measure of the amount of light that is directed into the correct regions of the sample plane, and the standard deviation measures the variation of intensity in the traps. For multi-spot patterns with m spots, these are defined as:

$$e = \sum_{m=0}^{N} I_m\,, \quad \sigma = 100\sqrt{\langle (I - \langle I \rangle)^2 \rangle}\,/\langle I \rangle\,, \qquad \text{Eq. 4.1 \& 4.2}$$

where I_m is the intensity of the m^{th} spot and $\langle I \rangle$ is the average over the m spots. Different hologram calculation algorithms were tested for MSIM pattern projection, and their performance was measured using these metrics.

4.2.1 Superposition of gratings and lenses

One of the simplest holograms is the stepped phase grating (figure 4.2). When applied to the back of the lens, a stepped grating deflects the focal spot from the centre of the focus. For multi-spot arrays the necessary hologram can be calculated by taking the sum of all the stepped gratings

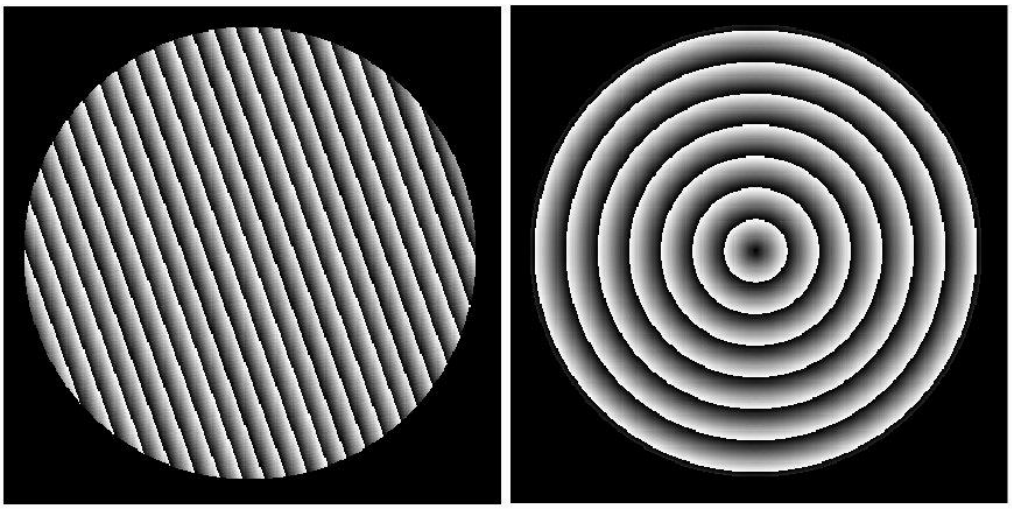

Figure 4.2: Simplest holograms.
Left: stepped phase grating. Right: Fresnel lens.

needed to deflect the focus to each of the spot locations. The same principle can be applied to create 3D spot patterns. The Fresnel lens hologram (figure 4.2) has the effect of displacing a spot in the axial direction, either above or below the focal plane. A focal spot can therefore be generated at any point around the focus by applying the combination of a stepped grating and Fresnel lens. Using the super-position principle, 3D multi-spot patterns can be generated by taking the sum of these combined holograms. This technique of summing individually-calculated holograms is termed the 'superposition of gratings and lenses' approach.[83,84] As a method for calculating holograms for multi-spot patterns, this approach is very appealing as very little calculation time – typically a few seconds – is required. This has formed the basis of a several multi-focal setups using diffractive optical elements and mechanical beam steering.[85][86] The downside of this approach is when calculating very symmetrical patterns.[87] This effect generates what is known as 'ghost traps' at the points of symmetry. The light deflected into these ghost traps lowers the overall efficiency of the hologram. This is particularly disruptive for eMSIM where regular grid patterns are needed. The issue can partly be resolved by introducing asymmetry into the patterns outside of the region of interest and then blocking out these regions. This method was tested *in silico* but still proved to offer a very low efficiency and, more importantly,

low uniformity. The speed of the algorithm, however, makes it an excellent candidate to provide an initial estimate for other hologram calculation methods. For eMSIM, the next group of hologram calculation algorithms tested were the Iterative Fourier Transform Algorithms (IFTAs). The superposition of gratings and lenses was, however, used throughout as a candidate to provide a starting estimate of the hologram.[88]

4.2.2 Iterative Fourier transform algorithms

IFTAs are one of the most popular methods for calculating kinoforms. As a group they are based on the simplest iterative algorithm, the Gerchberg-Saxton (GS) algorithm.[89] Simplified in figure 4.3, the GS algorithm breaks down the problem into a series of individual complex Fourier Transforms. Using the simplest lens focusing model, the distribution of the light in the focal plane is the complex 2D Fourier transform of the beam before the lens.[90] The GS algorithm uses this transform model to predict the distribution of the focused light. It then replaces the predicted amplitude with the desired one while keeping the

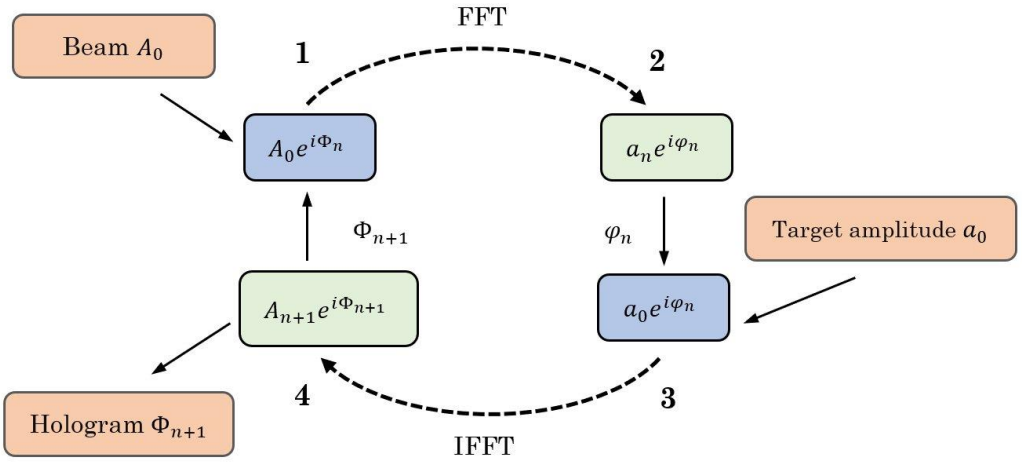

Figure 4.3: Steps of the GS algorithm.

1. The complex function of beam amplitude (A_0, and best-guess hologram, Φ_n) are forward transformed to the sample plane.
2. The amplitude at the sample plane is replaced by the target amplitude, a_0.
3. The complex function is then back-transformed.
4. The next guess at the hologram, Φ_{n+1}, can now be extracted. The amplitude at the pupil plane is then replaced by the beam profile, A_0, ready to be forward-transformed in the next iteration.

predicted phase in the focal plane. This complex distribution is then back-transformed to the lens plane to generate an estimate of the required hologram. Using knowledge of the beam amplitude profile, the process is then repeated until both a sufficient uniformity and intensity are produced. By breaking the process down into a series of Fourier transforms, the algorithm can be calculated programmatically using the Fast Fourier Transform (FFT) algorithm, also making it an efficient way to produce kinoforms on modern computers. Since they deal with the whole FOV with each iteration, the speed of the program is also independent of the number of spots. In terms of computational efficiency, these overtake the superposition techniques when calculating patterns with more than several hundred spots. IFTAs also show improved hologram efficiency and uniformity over superposition methods,[80] and many variants of these algorithms have also been developed, each with subtle changes that allow for a more application-specific optimisation.[91,92]

For eMSIM pattern projection, several IFTAs were tested. While the stand-alone GS algorithm is the simplest IFTA, it is one of the least popular for hologram calculation since it gives very poor pattern uniformity. The most commonly used algorithm is the GS-Adaptive Additive (GAA) algorithm. In figure 4.3, the GAA algorithm uses a different replacement scheme in step 2. The new amplitude taken forward is taken as a combination of the result of step 1 and the target amplitude, given by:

$$a_{new} = \omega a_0 + (\omega - 1)a_n \,. \qquad \text{Eq. 4.3}$$

In testing, the GAA algorithm performed better for the multi-spot patterns than the GS algorithm, giving an improved uniformity, although with a slightly reduced efficiency. This is in line with previous findings measuring algorithm performance for optical trapping.[80] Despite the improvement in uniformity, the calculated pattern uniformity – as measured by percentage standard deviation – was still below that required

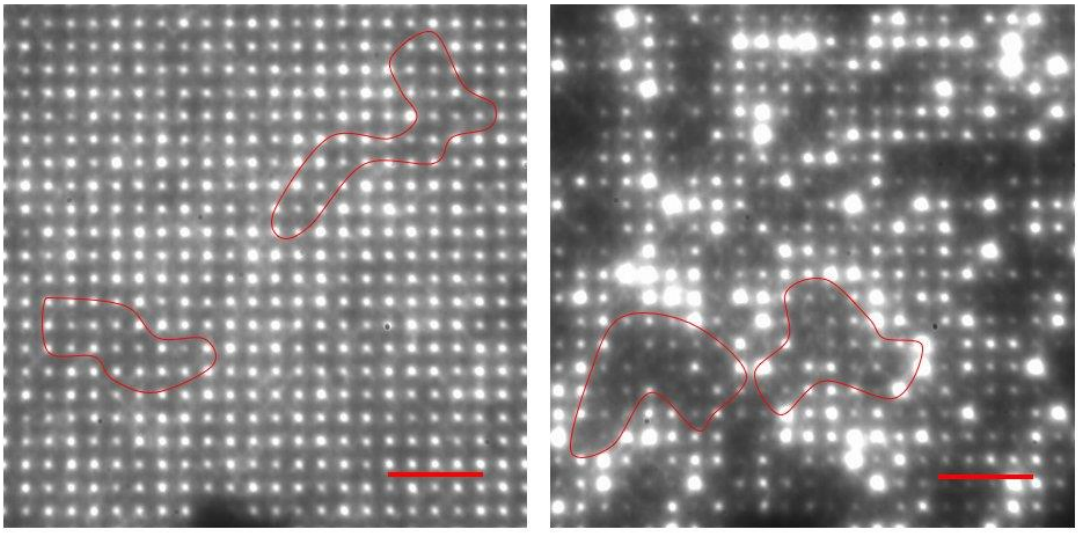

Figure 4.4: Comparison of GAA and GS IFTAs.

Left: GAA algorithm. Regions with random lower intensity outlined in red. Scale bar is 10μm. Right: GS algorithm. Regions with random lower intensity outlined in red. Scale bar is 10μm. Both holograms were calculated with 100 iterations.

for structured illumination. Figure 4.4 shows a comparison of multi-spot patterns generated using the GAA and GS algorithms. The GAA pattern shows significantly better uniformity compared to the GS algorithm, although still contains regions of reduced intensity.

The final IFTA tested was the Mixed-Region Amplitude-Freedom (MRAF).[93] MRAF aims to increase performance by allowing more degrees of freedom into the calculations. In the GS and GAA replacement schemes (step 2), the entire FOV is replaced. This constrains dark space in the region around the central multi-spot pattern. In practice this dark space, is not being imaged and a beam block can be used to occlude light from this region reaching the sample. MRAF uses this dark space as an extra degree of freedom in the algorithm by not replacing it with a dark region at step 2. The region being replaced is termed the Signal Region (SR) and the un-replaced section the Noise Region (NR). Figure 4.5 shows a comparison of the MRAF algorithm and GS algorithms as well as the target amplitude. Despite the addition of a noise region to increase degrees of freedom, there was very little increase in performance over the GS algorithm when generating multi-spot patterns. Because of this, the MRAF algorithm was not tested further for pattern projection.

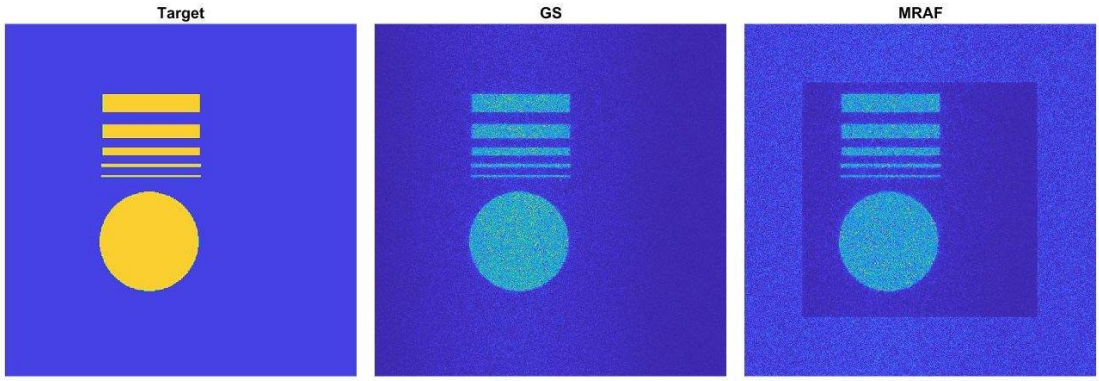

Figure 4.5: MRAF vs GS.

Comparison of the intensities resulting from the GS and MRAF algorithms. The target amplitude is shown on the left. On the MRAF image, the noise region is visible as the brighter region surrounding the inner target.

While the GAA algorithm showed improved performance over the GS algorithm, none of the IFTAs tested gave sufficient uniformity for MSIM and similar results have also been reported for other IFTAs.[94,95] The poor performance is a result of stagnation issues in the IFTAs. One of the most common reasons for poor IFTA performance is the introduction of aberrant

optical vortices into the hologram.[96] In the context of phase retrieval algorithms, an optical vortex is a singularity (pixel) where the phase of the surrounding pixels wraps back on itself. One property of the IFTAs is that they are incapable of removing optical vortices from the estimate of the hologram. This means any vortex present in the initial estimate remains in the final hologram. Figure 4.6 shows several optical vortices in the final hologram after 100 GAA iterations. While some optical vortices may be present in the final ideal hologram, the high density of those present suggests a number may be aberrant ones from the initial guess of the hologram. The IFTAs can be improved by isolating the vortices every few iterations and removing them.[96] This method, however, is very computationally intensive as every pixel must be tested for the presence of a surrounding vortex. As a result, IFTAs with vortex removal was not tested for holographic projection. Other attempts to avoid the stagnation issues have been to seed the IFTAs with initial guess holograms carefully designed to not include any optical vortices or by replacing the FT with a modified step factoring in the polarisation of the focal spots.[97]

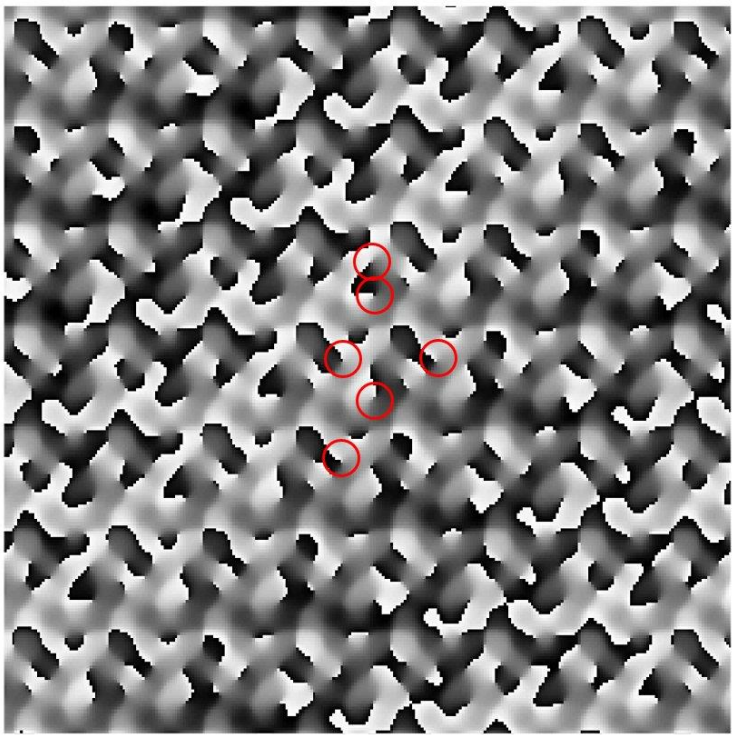

Figure 4.6: Optical vortices in IFTAs.

Hologram calculated using 100 GAA algorithm iterations. The optical vortices are circled in red.

4.2.3 Direct search algorithms

The alternative approach to calculate holograms is a Direct Search (DS) algorithm. In this method, the hologram is calculated pixel-by-pixel, with the best phase value of each pixel being chosen as the value which minimises the cost function:

$$C = \langle I \rangle - k\sigma \, . \qquad \text{Eq. 4.4}$$

Here, k is a constant which can be altered to weight the algorithm to prioritise either the uniformity or efficiency of the hologram. The DS algorithms typically produce the most efficient and uniform patterns. The disadvantage of the DS approach is the computation-intensity of the process. For example, calculating a 512×512 hologram with 16 grey levels requires 4,194,304 separate calculations. With IFTAs, the entire focal plane is calculated at the same time using an FFT. With the DS algorithm,

however, the time required to calculate the entire focal plane for each grey level at each pixel would be prohibitively slow. Using the above example, calculating the hologram on a mid-range graphics card using FFTs would take approximately 3 days because of the number of calculations required. Since the cost function only requires knowledge of the intensity at the location of the spots, a more sophisticated approach is to calculate the intensity only at these locations in the focal plane. Ignoring the effects of polarisation, the electric field $\epsilon(\vec{r})$ at a point $\vec{r}$ in the focal plane can be computed as the sum of the contributions from each of the N pixels in the hologram. Mathematically, this is expressed as:

$$\epsilon(\vec{r}) = \sum_{j=0}^{N} A_0(\vec{\rho}_j) exp\left(i\phi(\vec{\rho}_j)\right) \exp\left(-i\frac{2\pi\,\vec{r}\cdot\vec{\rho}_j}{\lambda f}\right). \qquad \text{Eq. 4.5}$$

$A_0(\vec{\rho}_j)$ and $\phi(\vec{\rho}_j)$ denote the amplitude and phase of the light incident on the j^{th} pixel on the SLM at a point $\vec{\rho}$. λ is the wavelength of the light and f is the focal length of the optical train. $\phi(\vec{\rho}_j)$ represents the phase change imparted by the SLM. For each pixel, the DS algorithm chooses a value for $\phi(\vec{\rho}_j)$ that minimises the cost function (equation 4.4). When computing

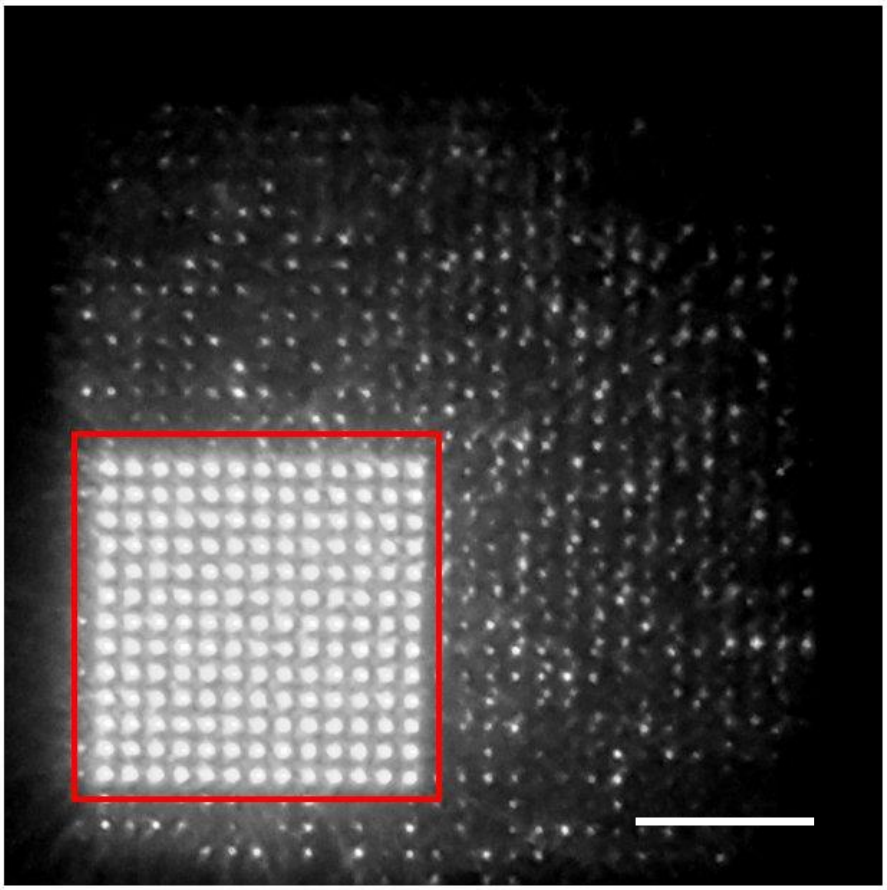

Figure 4.7: Pattern generated using DS algorithm.

The area of interest, where the MSIM/eMSIM imaging is performed, is outlined in red. The red circle denotes where the undiffracted portion of the beam has been blocked by the beam block. The lower efficiency of the DS algorithm is clear from the extent of the ghost traps extending from the region of interest. Scale bar is 20 μm.

holograms for optical traps where high intensity is required, the value of k is set to a low number, typically 0.1, to prioritise efficiency over uniformity. In contrast, MSIM and eMSIM require a high uniformity in the excitation pattern. In the optical setup used, the excitation light source provided more light than needed for imaging. This meant that hologram efficiency could be sacrificed to improve pattern uniformity. For MSIM and eMSIM pattern generation, the value for k in equation 4.4 was set to 0.4. Looking at figure 4.7 (which has been slightly over-exposed), the ghost traps – resulting from the symmetry of the pattern and reduced efficiency – extend a significant distance from the FOV.

4.3 Aberration correction

As previously discussed, one of the advantages of using phase engineering to generate the multi-spot patterns is the easy implementation of aberration correction. This section describes the background to this field and details how aberration correction was achieved in eMSIM/MSIM imaging.

4.3.1 Background

So far, in discussion of the resolution limit, we have been considering the case of ideal imaging conditions. However, to reach the maximum resolution limit imposed by Abbé's law, there are several aspects of the imaging system that must be maintained. For example, Abbé's law assumes homogenous imaging media with a constant refractive index throughout the focal length of the objective lens. This means that any refractive index mismatch will disrupt the resolution. Air-immersion objectives typically have the lowest resolution, partly due to the mismatch between the glass objective lens and the air. Higher-resolution objectives reduce this effect by using an immersion oil with the same refractive index as the lens and coverslip, although this does not address mismatch at the sample-coverslip interface.[98] As well as refractive index mismatching, the other most common aberrations found are astigmatism and spherical aberration arising from imperfect optics and off-axis illumination.

In classical widefield microscopy, where the excitation is a uniform intensity, the issue of these aberrations is limited to only the detection branch. As there are very few optical components in the detection pathway, and with high-quality objectives eliminating spherical and chromatic aberrations such detection aberrations are often ignored in all but the most sensitive imaging conditions like those required for SMLM. However, with imaging techniques that require precise excitation patterns, such as SIM

and MSIM, aberrations in the excitation pathway become an issue. This problem is compounded by the fact that more sophisticated illumination optics often require more optical components, each likely contributing to an overall distortion of the excitation wavefront.[99–101]

To correct for aberrations, it is important to have a mathematical description of the problem. In the simplest case of focusing a single beam, the aberrations can be represented by phase modifications on the complex beam function before the focusing element. These phase modifications are described by the 2-D orthogonal Zernike polynomials.[102] Figure 4.8 shows the phase profiles of the Zernike polynomials and figure 4.9 shows the PSFs generated at the focus of a beam with the corresponding Zernike aberration.

4.3.2 Global phase correction

Since every aberration can be described by a phase profile imposed on the optical pathway, aberration correction can easily be achieved by application of the inverse phase profile to the beam. If more than one aberration is present, the sum of the phase profiles can be applied to the beam to compensate for all aberrations simultaneously.

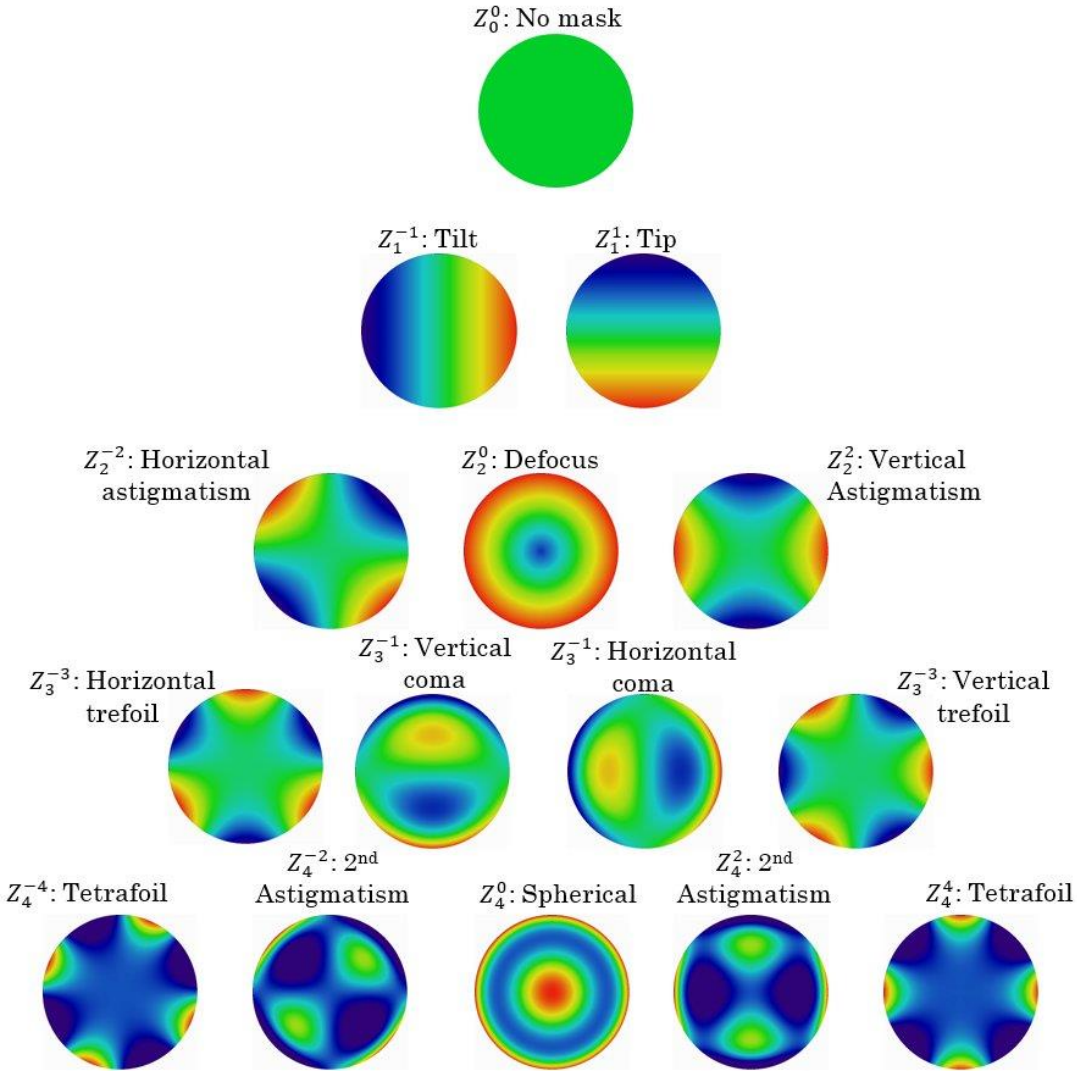

Figure 4.8: Phase profiles as described by Zernike polynomials.

Top row: The zero order zero frequency aberration which describes no aberration. Second row: The first order aberrations Z_1^{-1} and Z_1^1 which describe the vertical and horizontal tilt or shift. Third row: the second order Z_2^{-2} and Z_2^2 aberrations which describe the 45° and 0° first astigmatisms respectively. The second order zero frequency Z_2^0 polynomial describes system defocus. Fourth row: Z_3^{-3} and Z_3^3 are the left and right trefoil aberrations and the Z_3^{-1} and Z_3^1 are the horizontal and vertical coma aberrations. Fifth row: Z_4^{-4} and Z_4^4 are the tetrafoil aberrations which are uncommon in optics. Z_4^{-2} and Z_3^2 are the second astigmatisms. Z_4^0 describes the spherical aberration. The other polynomials with applications in optics are the Z_5^{-1} and Z_5^1 which represent the second coma and the Z_6^0 (not shown) which describes the secondary spherical aberration.

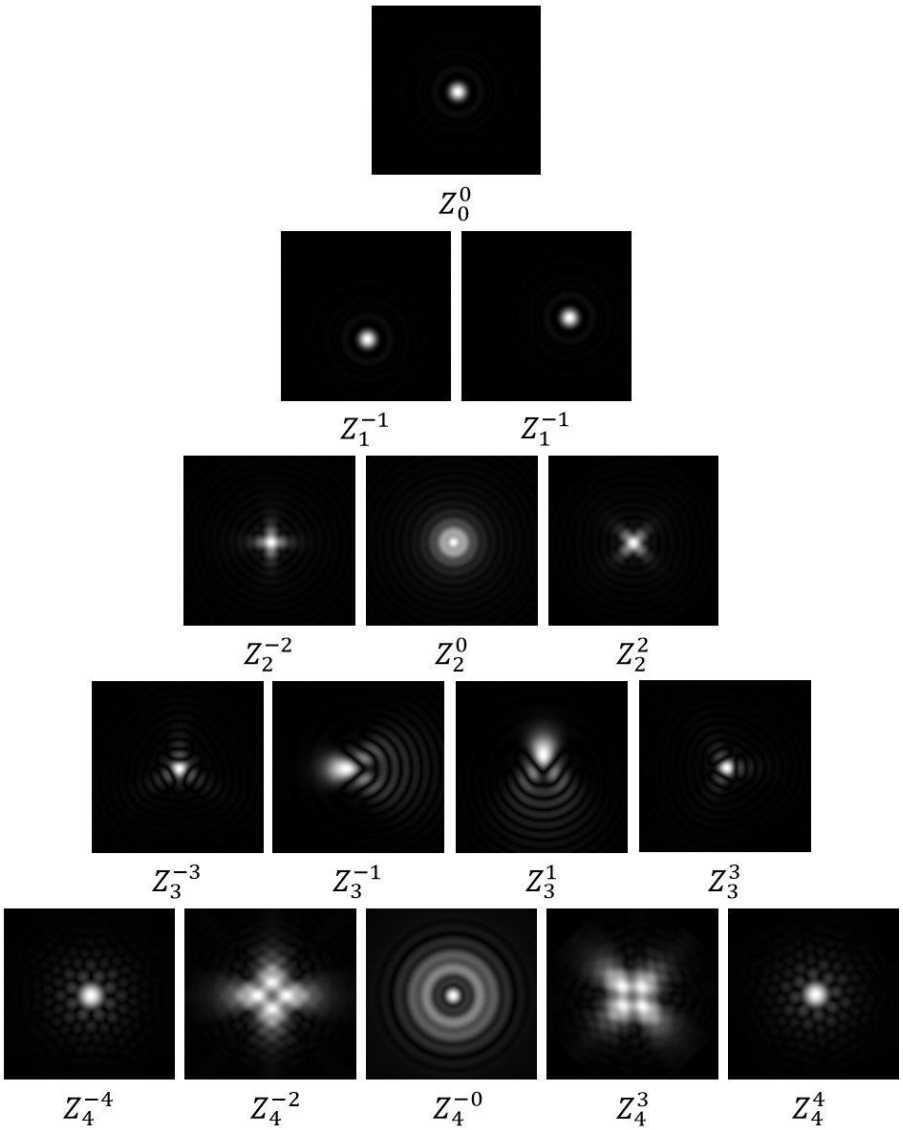

Figure 4.9: PSF distorted by Zernike aberrations.

Top row: The zero order zero frequency aberration which describes no aberration. Second row: The first order aberrations Z_1^{-1} and Z_1^1 which describe the vertical and horizontal tilt or shift. Third row: the second order Z_2^{-2} and Z_2^2 aberrations which describe the 45° and 0° first astigmatisms respectively. The second order zero frequency Z_2^0 polynomial describes system defocus. Fourth row: Z_3^{-3} and Z_3^3 are the left and right trefoil aberrations and the Z_3^{-1} and Z_3^1 are the horizontal and vertical coma aberrations. Fifth row: Z_4^{-4} and Z_4^4 are the tetrafoil aberrations which are uncommon in optics. Z_4^{-2} and Z_3^2 are the second astigmatisms. Z_4^0 describes the spherical aberration.

Applying the phase profile to the beam is achieved with a phase-only SLM,[103,104] a deformable mirror (DM),[105,106] or a hybrid approach, merging the two technologies.[107]

As with holography, the corrective element used is placed in the conjugate plane to the back of the objective and the appropriate phase profile applied. SLMs have the advantage that they have many more pixels than there are actuators on DMs, meaning they can generate more complicated phase patterns. Because of this, they are able to compensate for higher order and more severe aberrations. However, for aberration correction in biological imaging, DMs remain the most popular choice since they are more optically efficient and have faster response times.[108]

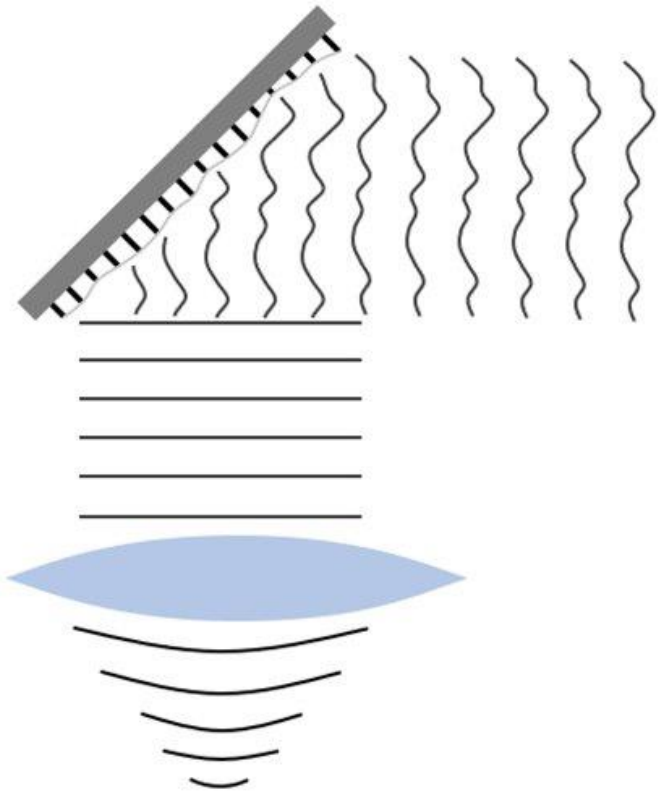

Figure 4.10: Deformable Mirror.

An aberrated wavefront incident on the deformable mirror. Actuators underneath the mirror deform the surface of the mirror such that aberrations in the distorted wavefront are corrected for. This allows the wavefront to be focused properly by following optical components.

4.4 Location-dependent correction of aberrations

As with all forms of structured illumination, MSIM and eMSIM are susceptible to aberrations arising from imperfect optical components and alignment. The effect of aberrations in eMSIM is made worse by the fact that image quality is disrupted by aberrations in both the spot and doughnut patterns. Applying the inverse phase profile to the entire excitation beam is a simple way to remove aberrations affecting the whole excitation beam equally, for example defocus.[81] However, not all aberrations affect the entire FOV equally, and in these cases applying the Zernike profile to the beam would only correct for aberrations in a small portion of the FOV while increasing aberrations in other regions. The effect of this is that imaging must be limited to only a small fraction of the FOV where all spots are aberrated equally. Figure 4.11 shows an example MSIM pattern with a radially-dependent astigmatism, common in MSIM excitation over wide FOVs.

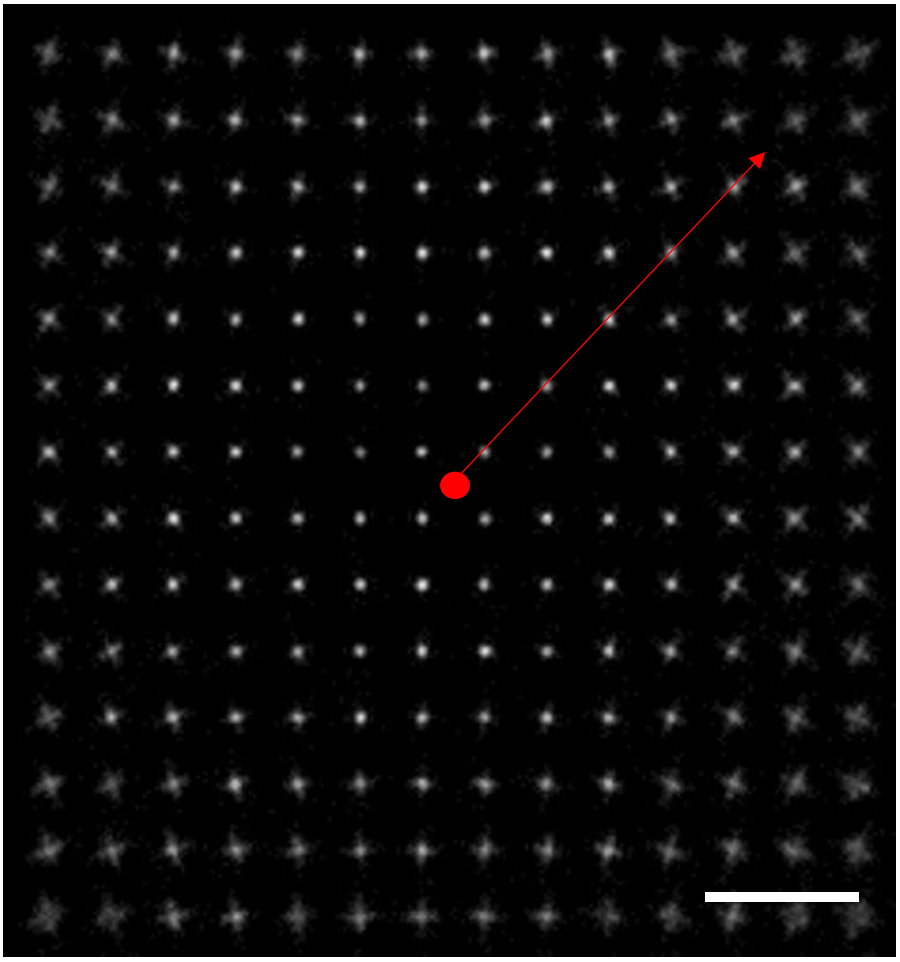

Figure 4.11: Radially dependent astigmatism.

Simulated focal plane with a radially dependant astigmatism. The simulated central point is denoted by the red spot. With increasing radius, the magnitude of the astigmatism increases. There is also an angular dependence which changes the relative magnitudes of the lateral and vertical astigmatism components around the FOV. PSFs were calculated for a wavelength of 532 nm and an objective lens with 1.4 NA. Scale bar is 4 μm

To maximise the area of the sample that can be imaged, it is necessary to compensate for aberrations in a spot-dependent manner. To achieve this, a modified DS algorithm was developed to introduce a factor $K(\vec{r},\vec{\rho})$ to compensate for location-dependent aberrations:

$$\epsilon(\vec{r}) = \sum_{j=0}^{N} A_0(\vec{\rho}_j) K(\vec{r},\vec{\rho}_j) exp\left(i\varphi(\vec{\rho}_j)\right) \exp\left(-i\frac{2\pi\,\vec{r}\cdot\vec{\rho}_j}{\lambda f}\right). \quad \text{Eq. 4.6}$$

$K(\vec{r},\vec{\rho}_j)$ is a kernel which adds a different phase value to each pixel of the hologram according to the aberration of the spot at position $\vec{r}$.

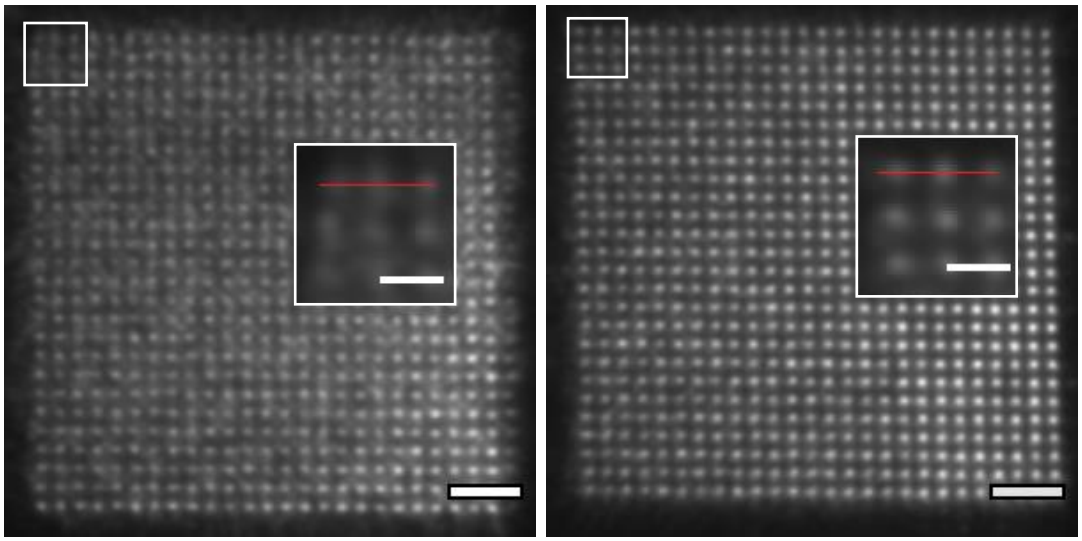

Figure 4.12: Aberration correction in holographic projection.

Multi-spot patterns projected onto a fluorescent surface. Left: Uncorrected pattern. Right: Corrected pattern. In comparison to the corrected pattern, the uncorrected grid shows reduced contrast between the spots due to smearing of the PSF from aberrations. The radial dependence of the astigmatism means this reduction in contrast is most noticeable in the top left of the uncorrected pattern, furthest from the centre of focus (bottom right). Inset shows magnified region of image indicated. Intensity profiles in figure 4.13 were taken across the red lines. Main scale bar is 5 µm, iset scale bar is 2 µm. 488 *nm* excitation patterns were projected onto rhodamine monolayer through 100X 1.4NA objective.

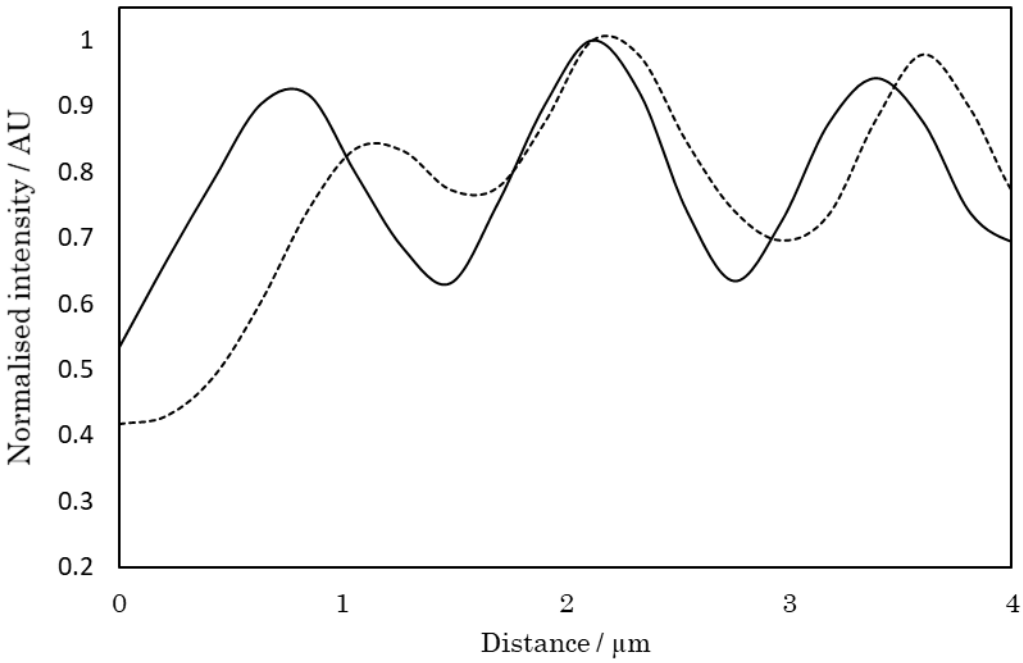

Figure 4.13: Line profile across three extremal excitation spots.

Line profiles taken across the spots indicated in figure 4.12. Solid line: Spots with aberration correction. Dashed line: spots without aberration correction. Not only is there increased contrast between the peaks, but the spacing between the peaks is also constant in the corrected pattern.

In the eMSIM setup, the most significant aberration was a radially-dependent astigmatism, which increased with the distance from the centre of the grid. As such, the kernel was set to:

$$K(\vec{r},\vec{\rho}) = \exp\left(i\sqrt{\vec{r}\cdot\vec{r}}\left(\alpha\rho_x\rho_y\cdot\cos(\theta_r) + \beta\left(\rho_x^2-\rho_y^2\right)\cdot\cos(\theta_r)\right)\right), \quad \text{Eq. 4.7}$$

where α and ß are constants describing the magnitude of the first two astigmatisms as defined by the Zernike polynomials. The $\cos(\theta_r)$ and $\sin(\theta_r)$ dependence describe the change in the 'direction' of the astigmatism around the centre of the grid. The workflow for the updated DS algorithm is depicted in figure 1.4.

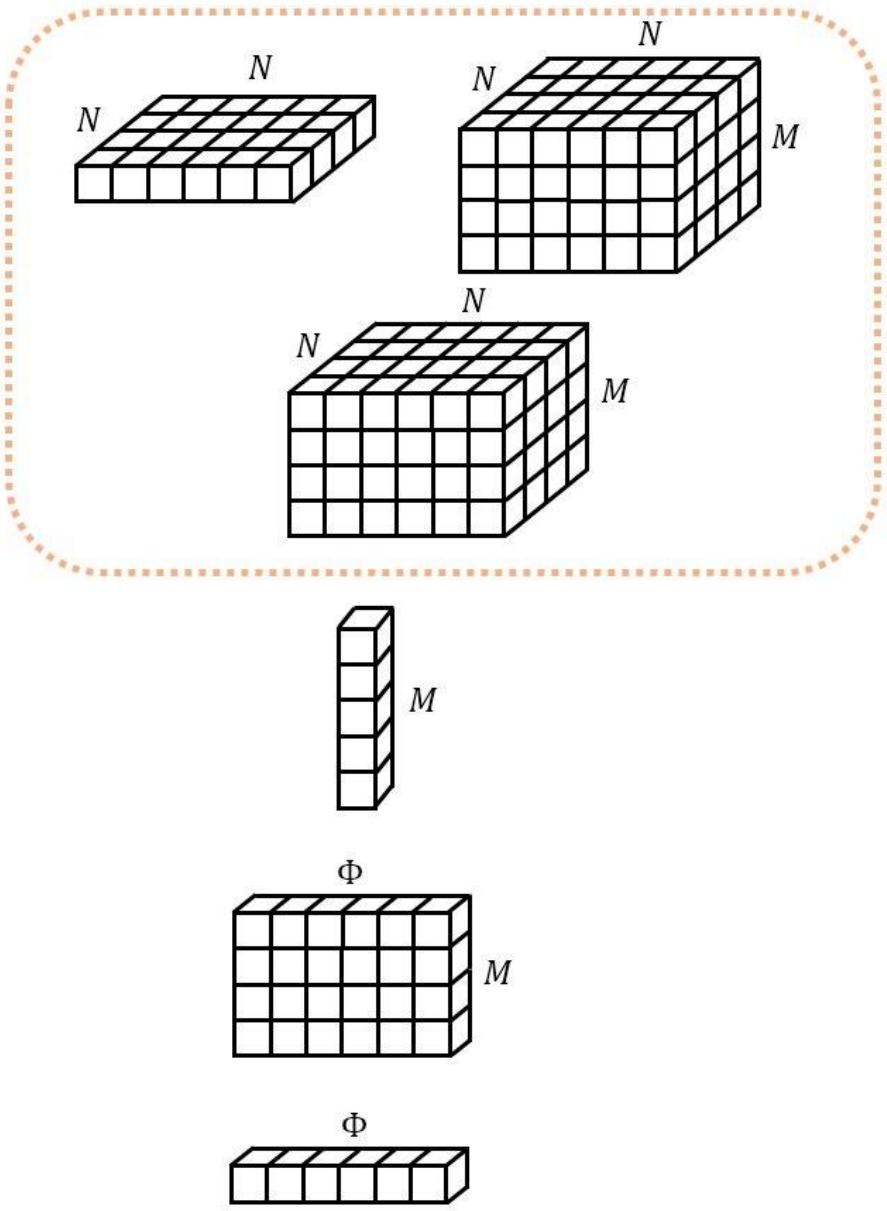

Figure 4.14: Workflow of DS algorithm.

To calculate an $N \times N$ hologram for M spots and Φ possible phase values at each pixel, the modified DS algorithm works as follows. Steps 1 and 2 are computed on the GPU to accelerate the algorithm.

1) $A(\vec{\rho})$ and $K(\vec{r},\vec{\rho})$ are computed to generate $N \times N$ and $N \times N \times M$ arrays.
2) These arrays are combined to form $A(\vec{\rho})K(\vec{r},\vec{\rho})$, an $N \times N \times M$ array.
3) For each hologram pixel, $\vec{\rho}$, $A(\vec{\rho})K(\vec{r},\vec{\rho})$ is indexed and $A(\vec{\rho})K(\vec{r},\vec{\rho})exp\left(-i\frac{2\pi\,\vec{r}\cdot\vec{\rho}}{\lambda f}\right)$ is calculated at each spot to generate a $1 \times M$ array.
4) Using the array from 3), $A(\vec{\rho})K(\vec{r},\vec{\rho})exp(i\phi)exp\left(-i\frac{2\pi\,\vec{r}\cdot\vec{\rho}}{\lambda f}\right)$ is calculated to form a $\Phi \times M$ array.
5) The cost function C is calculated for each value of ϕ to generate a $\Phi \times 1$ array. The maximum value for C in this array is used to choose the optimal value for ϕ.
6) Steps 3 – 5 are repeated until all pixels of the hologram have been optimized.

4.5 Holography in MSIM and eMSIM

Because of the advantages of holography over conventional SIM pattern generation methods, it was used throughout the project for pattern projection. While theoretically holography could be used for MSIM/eMSIM, there will always be small deviations in spot uniformity. To test whether these deviations would affect SIM, the method was tested *in silico*. MSIM imaging was simulated using the excitation patterns generated from the DS algorithms and compared to ideal patterns constructed from calculated PSFs. Figure 4.15 shows a comparison of MSIM performance using the DS-

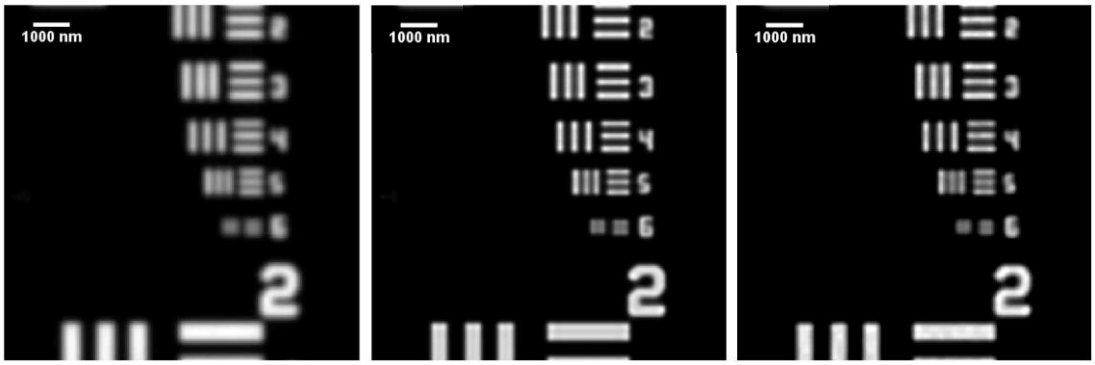

Figure 4.15: Testing of DS algorithms for MSIM.

1. Simulated diffraction-limited image. **2.** Simulated MSIM image with ideally-constructed patterns. **3.** Simulated MSIM image with patterns generated by DS algorithm. The DS-generated patterns have given a comparable resolution increase over the ideally-constructed patterns. PSFs were calculated for 488 *nm* excitation and objective NA of 1.4.

generated patterns and ideally-constructed ones. Although there is deviation from perfect uniformity in the holograms, this has not prohibitively affected image reconstruction. While this was an important test of holography, the results are limited by the calculation of the excitation patterns. In the ideal conditions modelled, the only effect on excitation pattern was a reduction in pattern uniformity. In real-world application however, a number of other factors (such as sample-specific aberrations) affect the final pattern at the sample. The simple model also does not factor in the effects of polarisation on the patterns and comparison

to the ideal patterns is also limited as, in-reality, all methods of pattern projection would be affected by imperfections in the optical system.

4.6 Summary

The holographic projection method described here offers a new and versatile way to generate SIM excitation patterns. Unlike traditional SIM methods where the patterns are generated using mechanically-moved diffraction gratings, holographic projection requires no moving parts, greatly simplifying construction and system stability. Furthermore, the use of phase engineering allows for sophisticated correction of aberrations in the system which would require additional components in either striped SIM or amplitude-only MSIM projection.

5. Optical methods in holographic projection microscopy

Summary: *this chapter will describe the optical methods used throughout the project for pattern projection and imaging. It will describe the principles behind the choices of optical setup as well as detailing the construction, calibration and platform testing*

5.1 Pattern projection

5.1.1 Spatial light modulators

Throughout this project, SLMs were used for pattern projection. As SIM has developed, SLMs have been increasingly used to generate the excitation patterns. Compared to beam interference techniques, they offer a lot of advantages in terms of versatility and simplicity. As well as striped patterns, SLMs allow for projection of any desired pattern onto the focal plane. In biological imaging this can be used not only in structured-illumination, but also techniques which required targeted illumination. For example, fluorescence recovery techniques, which image the movement of fluorophores into an area which has been photobleached, require intense illumination at specific locations in the sample. Such systems which do not use pattered illumination for resolution enhancement are termed Programmable Array Microscopes (PAMs).[109]

5.1.2 Amplitude modulation

In optical microscopy, and SIM in particular, SLMs are most commonly used in an amplitude-only fashion. This is commonly chosen for the simplicity of the design and a high contrast ratio between the off and on pixels. In this configuration, digital micromirror devices (DMDs) are usually the SLM of choice. On these devices each pixel is a small mirror on

an actuator. The pixels are switched from 'on' to 'off' by changing the actuator to deflect the beam in a different direction. The portion of the beam deflected by the 'off' pixels is reflected into a beam dump and the light from the 'on' pixels continues down the optical pathway.

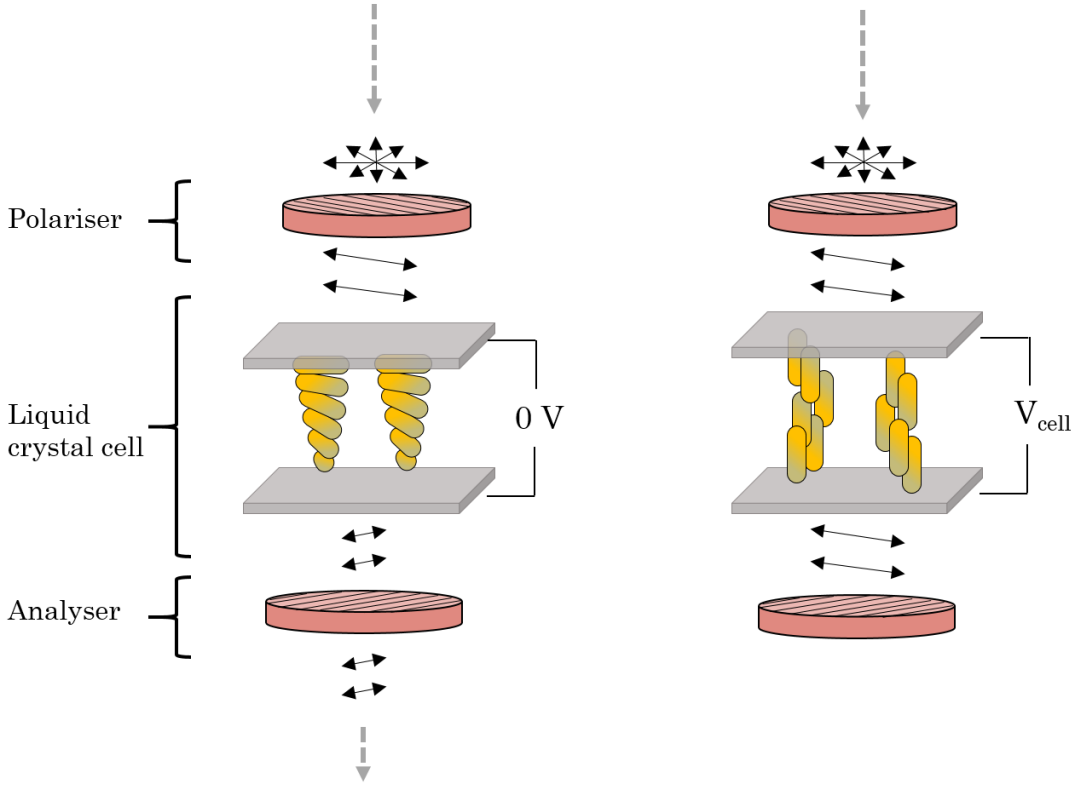

Figure 5.1: Twisted nematic LC layer as an amplitude-only SLM.

Left: LC with no applied electric field. Right: LC with a voltage applied across the cell. Unpolarised light enters the LC device through a linear polariser, producing linearly polarised light. In the case of no applied electric field (left), the LC adopts a stacked, twisted configuration. This has the effect of rotating the polarisation of the light by 90°. In the case where a voltage, V_{cell}, is applied across the LC (right), the LC molecules align with the direction of the electric, losing the twisted configuration. With no twisted structure, the polarised light passes through the LC cells without a change to the polarisation. After exiting the LC, the light passes through a second polariser, the analyser, with is rotated 90° relative to the first polariser. As a result, only light which has had its polarisation rotated by the cell is capable of passing through. By building the pixels of the SLM from independent LC cells, patterns and images can be projected by controlling which pixels allow light to pass through.

The second class of SLMs are those based on Liquid Crystal (LC) technology. The LC chips used in this project were based on the twisted nematic field effect, shown in figure 5.1. Twisted nematic LC SLMs rely on the polarisation rotation effects of LC layers. When no voltage is applied across a twisted nematic LC layer, the LCs align into a twisted

configuration, rotating the polarisation of transmitted light. When a voltage is applied across the layer, the crystals re-orient parallel to the electric field, and in this configuration, there is no change in the polarisation. By placing the LC layer between two crossed polarisers, the amplitude of the transmitted light can be varied by changing the extent of the polarisation rotation. For many years, twisted nematic LCs were the most commonly used LC configuration in display technology. More recently, they have been replaced by in-plane switching LCs and Liquid Crystal On Silicon (LCOS) SLMs, though they are still the most common LCs used in digital projectors. For amplitude modulation, LCOS SLMs are the most common LC chips in use. The advantage of using LCs over DMDs for this application is that they allow for different grey levels, typically 8-bit or 256 levels. This variable intensity, however, comes at the cost of a lower contrast ratio between the on and off pixels.

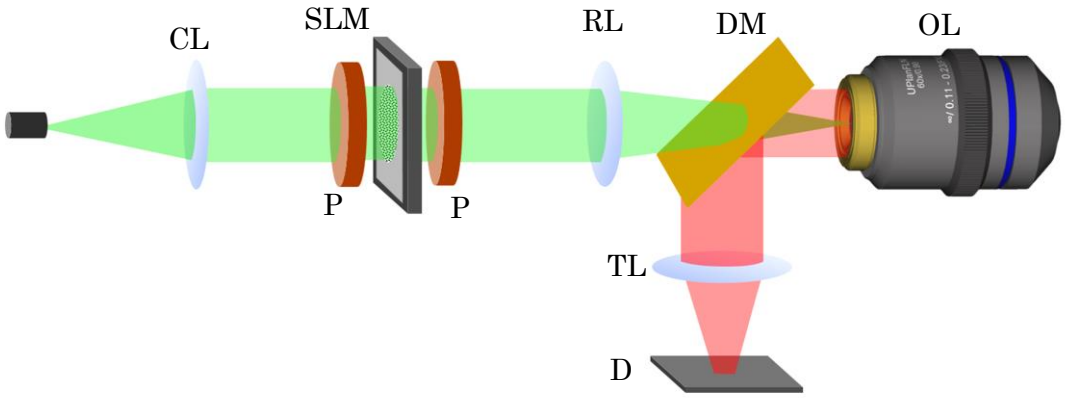

Figure 5.2: Placement of SLM for amplitude-only modulation.

Incoming beam (green) is expanded and collimated by a collimating lens (CL) to overfill the SLM. This helps to increase the uniformity of the illumination light. In this case, a transmissive LC SLM is being used, and the SLM is sandwiched between a pair of crossed polarisers (P). For micro-mirror devices, no polarisers are required, and the incoming beam is reflected off the device into the optical path. A relay lens (RL) relays the image to the objective lens; this places the Fourier plane at the back of the objective lens (OL). In this way, the image of the SLM is projected onto the sample by the objective lens. Any fluorescent signal (red) recovered from the sample reflects off a dichroic mirror (DM) and is imaged onto a detector (D) by a tube lens (TL).

5.1.3 Phase modulation

The second way that SLMs can be used is in phase manipulation of the incident beam. As well as rotating the polarisation of transmitted light, LCs also affect the phase of the light in a voltage-dependent manner. This effect is maximised when using elliptically-polarised light. By converting linearly-polarised light to elliptically-polarised light with a quarter waveplate, passing it through an LC layer, and converting it back to a linearly-polarised light with a second quarter waveplate and polariser, a phase-only – or rather a phase-mostly – SLM is created. It is this phase-modulation capability of LC SLMs that allows them to be used in PSF engineering and holography, where phase manipulation of a focused beam is required.

The SLMs used (shown in figure 5.3) were of the transmission type and taken from a commercial projector though were the same liquid crystal chips as used in several scientific grade SLMs. As transmission SLMs they had a relatively low fill factor (~60%) compared to reflective LCOS chips (~90%) meaning they were less light efficient than might otherwise be achieved however, given the excess laser power available and hologram efficiency this lower fill factor did not adversely affect pattern projection. The chips offered a very fine 8-bit greyscale resolution (i.e. 256 available grey levels). However, the effect the LC layer in the chip has on the incident

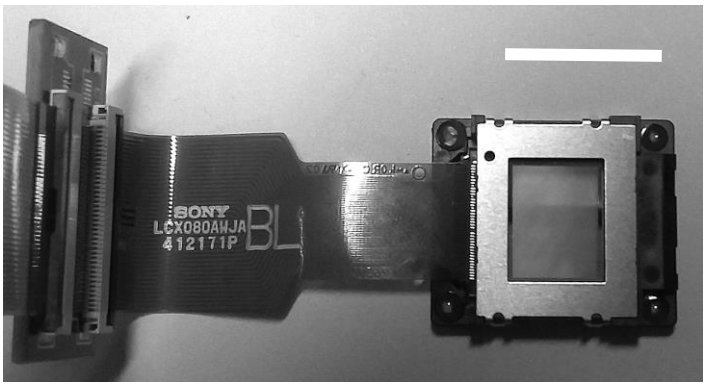

Figure 5.3: Image of the transmission SLM used.

Sony LCX080 transmission liquid-crystal chip. Scale bar is approximately 2.5 *cm*.

light is not directly proportional to the voltage applied across the layer. To account for this, the projector is calibrated with a lookup table (LUT) to ensure the correct voltage will be applied to the layer. While a projector is a cost-effective way to obtain and drive the SLMs, one disadvantage is that this LUT within the projector cannot be altered. Since polarisation rotation – for which the projector is calibrated – is not proportional to phase change, there are added complexities when using these SLMs for phase-only modulation. Most importantly, the voltage required to generate a $\pi/2$ polarisation rotation (i.e. the highest voltage the projector can provide) is lower than that required to generate a 2π phase change. This effect can be minimised by using the LC chip dedicated to the red channel of the image. For longer wavelengths, a higher voltage and/or layer thickness is needed for a $\pi/2$ polarisation rotation. In the projector, this means the voltages applied to the LC layer in the chip for the red channel are higher than in the other chips. For shorter wavelengths (i.e. the blue and green excitation wavelengths) this means the maximum polarisation rotation would be $> \pi/2$ and the phase shift is also maximised. As well as the imperfect phase change that is characteristic of the SLMs, the LUT built into the projector does not result in a linear increase in phase change with increasing grey level. For the highest-possible quality of holographic projection, the LUT needs to generate a linear increase in phase change with grey level, and the maximum phase change possible needs to be measured for each wavelength. Calculating the new LUT was done using a common-path interferometer (see Fig. 5.4). In this setup, a coherent and unpolarised beam is collimated before passing through a linear polariser and quarter waveplate to generate elliptically-polarised light. The beam is then

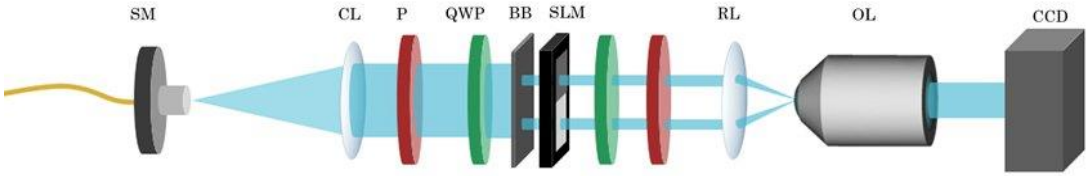

Figure 5.4: Common-path interferometer.

SMF: Single-mode fibre. CL: Collimating lens. P: Linear polariser (Red). QWP: Quarter waveplate (Green). BB: Beam block. SLM: Spatial light modulator. RL: Relay lens. OL: Objective lens. CCD: Camera.

separated into two beamlets using a beam block. These beamlets then pass through two halves of the SLM, where each half of the SLM is displaying a different grey level. The beamlets then pass through another quarter waveplate and linear polariser before being focused to a point by a relay lens. This sandwiched approach to LC SLM setups was used as it maximises the phase change that can be achieved. At the focal point of the first lens, the two beams interfere with each other and generate a striped interference pattern. This interference pattern is then imaged onto a camera using a low magnification objective lens. By leaving one half of the SLM at the zero grey level and changing the grey level of the second half in regular steps, the relative phase of the two beamlets can be altered. At the focal point, this relative change in phase causes a phase shift in the interference pattern, equivalent to a lateral shift in the striped pattern image collected by the camera.

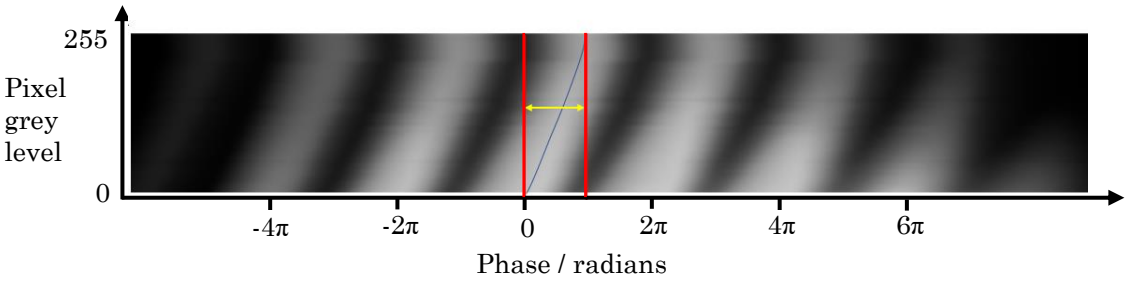

Figure 5.5: Calibration of SLM LUTs.

The stack of striped images acquired at different grey levels on the projector SLM is merged to form one image representing the phase-shift at each level. The minima of the pattern is then traced (orange line). The phase shift of each grey level is then the lateral displacement of the line from the minima at the zero level. The total phase shift possible is the distance between the lateral extremes of the line (red lines).

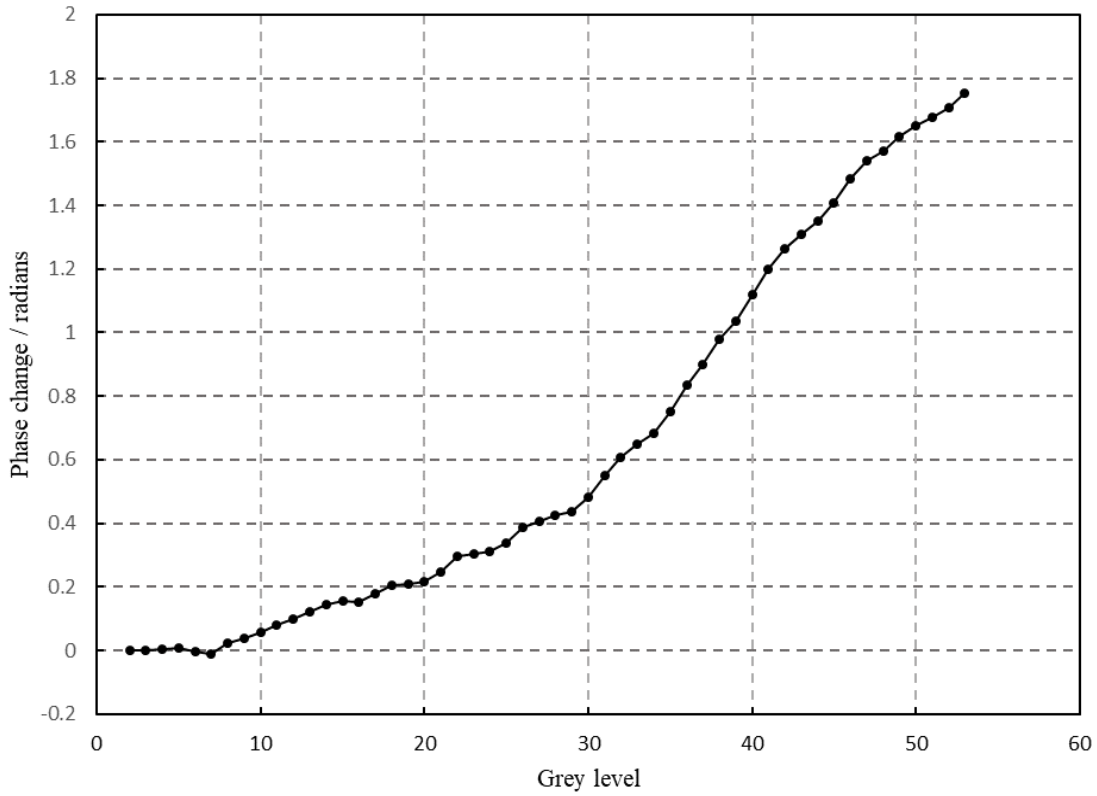

Figure 5.6: Graph showing phase change with increasing grey level.

Measurements were made using a common-path interferometer using 488 nm laser light. The phase change increases with grey level, up to a maximum of 1.753 radians. The increase is approximately linear after a short region where there is no phase change with increasing grey level.

By looking at the movement of the minima in this striped pattern as the grey level on the SLM increases, the maximum phase change can be measured and a new LUT can be developed. Measuring the extent of the lateral shift for each grey level allows for a quantifiable measure in phase shift. This process is shown in figure 5.5. These phase measurements were then repeated for each of the wavelengths used ($405\,nm$, $488\,nm$ and $532\,nm$). The measured LUTs were then applied to the holograms before being sent to the projector.

5.2 Optical setup

5.2.1 Excitation light source

For eMSIM, a custom multi-line laser system was constructed and used to provide the excitation light throughout. Five laser diodes (wavelengths

637 nm, 532 nm, 488 nm, 450 nm and 405 nm) ware combined coaxially and coupled to a single-mode fibre by a 10 X microscope objective. The emission from each diode passed through a laser-line filter, to give a $\pm 2\,nm$ wavelength range for each laser line. The output powers of each diode were varied through control of dedicated constant current power supplies. Diode triggering was controlled through an Arduino development board, in turn controlled through a LabVIEW DAQ card. Using an Arduino allowed for control of the diodes through a manual trigger switch when the computer was disconnected, as well as LabVIEW control when the computer was running. During image acquisition, the diodes were triggered with start of image acquisition to prevent unnecessary exposure of the samples to excitation light.

Widefield excitation was achieved on the Leica microscope by a mercury vapour discharge lamp coupled to a liquid light guide. The light from the light guide was collimated and focused onto the back focal plane of the objective to give uniform illumination of the sample. A flip mirror was installed in the holographic projection optics to switch between holographic and widefield excitation. The shutter on the discharge lamp was again controlled using the Arduino development board to allow manual and automated control.

5.2.2 Holographic projection optics

To demonstrate the potentially modular nature of the holographic projection technique, the holographic projection optics were constructed on a semi-portable breadboard at the back of the microscope. Light entered the system from a Single-Mode Fibre (SMF) as linearly polarised zero-order Transverse Electromagnetic Mode (TEM_{00}) beam and was collimated by a collimating lens, CL. During hologram calculation, the amplitude of the light was approximated to have uniform intensity across the input plane at the hologram. For the hologram to be properly projected, the intensity at the SLM must also have a uniform intensity. Since the laser left the SMF with a Gaussian intensity profile, the beam was expanded until the central region that illuminates the SLM had minimal intensity variation across it. The beam then passed through a linear polariser and a quarter waveplate, the angles of which were set using the common path interferometer. For holographic projection, the phase modulation pattern on the SLM must be relayed onto the back focal plane of the objective lens. This was achieved using a 4f optical system (see figure 5.8) composed of the relay lenses, RL, in figure 5.7. An image of the excitation pattern was formed at the Fourier plane between the two relay lenses.

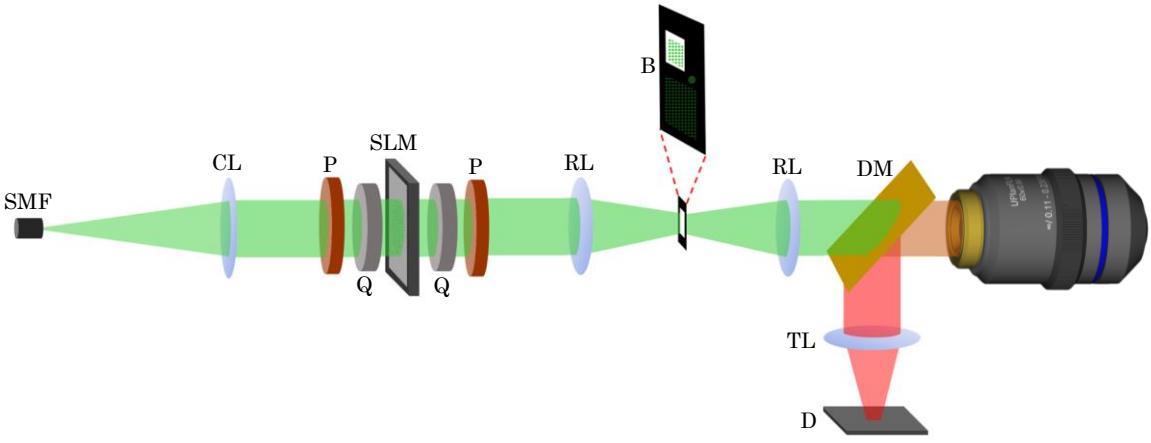

Figure 5.7: Setup for holographic projection.

SMF: Single-mode fibre. CL: Collimating lens. P: Linear polariser. SLM: Spatial light modulator. Q: Quarter waveplate. RL: Relay lens. B: Beam block. Magnified region shows the shape of the beam block used to block ghost traps and the portion of the beam not deflected by the SLM. TL: Tube lens. DM: Long-pass dichroic mirror. O: Objective lens. D: Detector.

Since the SLM allowed a fraction of the light to pass through without phase modulation and ghost traps appeared outside the FOV, a beam block was placed at the centre of the Fourier plane to block unwanted light from reaching the sample. The size of this square was matched to the size of the pattern in the Fourier plane, excluding light from ghost traps outside of the projected pattern area. The light then entered the microscope body through a dichroic beam splitter.

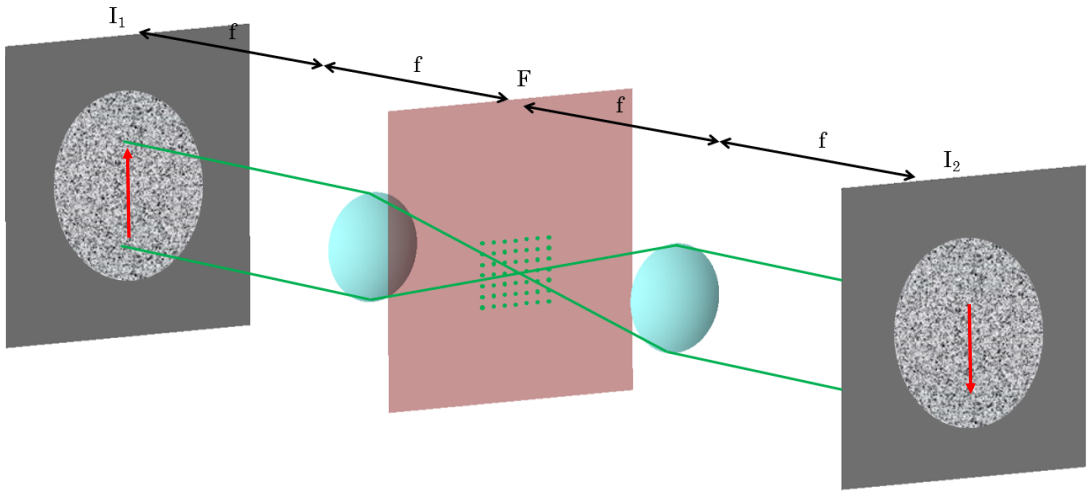

Figure 5.8: 4f optical relay system.

Two lenses, with focal lengths f, are placed a distance of 2f apart from each other. At a distance, f, before the first lens, is the input image plane, I_1. Light is focused by the first lens to the Fourier plane, F. The second lens collects the focused light from the Fourier plane, and the image plane, I_1, is replicated at the plane I_2, a distance f from the second lens. The image at I_2 appears as a flipped version of the image at I_1. In holographic projection, the SLM and objective lens are placed at the planes I_1 and I_2 respectively. In the optical setup, the pattern to be projected onto the sample is replicated at the Fourier plane.

5.2.3 Microscope body

Two microscope chassis were used throughout: Leica DMi8 and Olympus IX71 inverted microscopes. A Ludl motorised stage and focus drive was added to the Olympus frame and controlled through a dedicated Ludl control box. The motorised stage, shutter, and focus drive on the Leica DMi8 were all integrated into the chassis, and were controlled through the Leica CTR-control box. Both microscope bodies contained the filter cubes used for imaging. Filter cubes in the microscope directed the excitation light into the objective and isolated the fluorescent signal. For UV excitation/ emission, a 405 nm laser line excitation filter, 420 nm long-pass dichroic mirror and 435 nm long-pass emission filter were used. Blue laser excitation was achieved with a 488 nm laser line filter, a 510 nm long-pass dichroic mirror and a 520 nm long-pass emission filter. Green excitation was achieved with a 532 nm laser line filter, a 550 nm long-pass dichroic mirror and a 555 nm long-pass emission filter. Due to time and cost limitations, filter cubes for the Leica DMi8 chassis were 3D printed from polylactic acid. As expected, the prints of the filter cubes were not perfectly consistent, and the dichroic mirrors had slightly different alignments in the different cubes. On a conventional SIM/MSIM microscope, this would be problematic as differences in the beam paths between the filter cubes would mean inconsistent alignment of the patterns. However, for holographic projection, perfect uniformity was not required as different phase masks could be applied to the holograms for different cubes to compensate for any inconsistencies. For the widefield imaging, illumination of the FOV of the camera was not affected by the differences between the cubes.

5.2.4 Detection optics

Three different cameras were used throughout. Initial tests were carried out with a CMOS camera (Raptor photonics, Osprey) as this provided the

fastest imaging speeds in bright environments, (typically below 10 ms per frame). This camera was also used for imaging under brightfield and widefield fluorescent illumination. The Osprey camera was controlled through LabVIEW via a Camera Link frame grabber. The camera was triggered using an external trigger line from a DAQ card. However, the COMS camera proved not to be sensitive enough for the low-light conditions of live-cell and fixed-cell MSIM/eMSIM imaging. As an example, the typical exposure time required was 2 seconds per frame, meaning a total acquisition time of 17 minutes for each eMSIM image. Because of these low-light conditions, more sensitive Electron-Multiplying Charge Coupled Devices (EMCCDs) were needed. Two EMCCDs were used in imaging, an iXon life-EMCCD (Andor) and an ImagEM-X2 camera (Hamamatsu). Image acquisition with the iXon life was controlled through the Andor Solis software package but was integrated into the eMSIM setup by triggering the camera externally through a DAQ card. The Hamamatsu camera was also controlled through its own software package and integrated into the system with external triggering. Given the high sensitivity of the EMCCD cameras, imaging speeds were limited by the switching time of the LC SLM. Typical frame acquisition times were 20 ms, meaning an eMSIM image would require a total imaging time of 9 s, suitable for imaging relatively slow-moving cellular structures, such as the mitochondrial network.[110]

One important factor to consider in super-resolution microscopy is the resolution of the camera being used and whether the pixels of the camera are sufficiently small to meet the Nyquist criteria. In microscopy, the Nyquist criteria dictates that to maintain image resolution, the periodicity of the pixels must be at least twice that of the highest spatial frequency permitted by the objective. This means that the width of the pixels must be less than half the size of the diffraction limit. When placed in the camera port of the microscope, the Osprey camera – whose pixels were 5.5 $\mu m \times 5.5$ μm on the sensor – gave pixel sizes in the acquired image roughly equivalent to 30 $nm \times 30$ nm (for the 100× 1.4NA objective). This size is well below the $60\,nm \times 60\,nm$ pixels required for Nyquist imaging. This excessively small pixel size will also have contributed to the low sensitivity of the camera, as the detected signal was split across too many pixels.

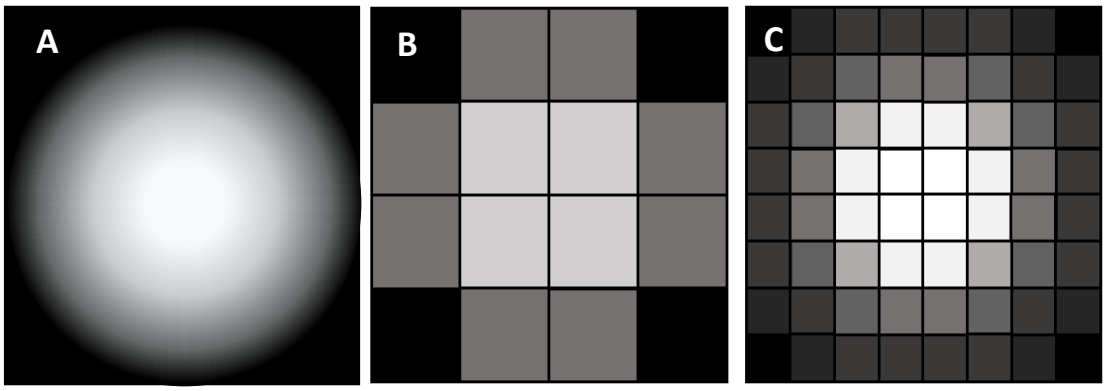

Figure 5.9: Demonstration of the Nyquist sampling criterion.

A Diffraction-limited object. **B** Image captured below Nyquist level. **C** Image captured above Nyquist level. For two adjacent point sources, the FWHMa of the two would be indistinguishable for the sampling density in **B**.

For the iXon camera, whose pixels on the sensor are $13\,\mu m \times 13\,\mu m$, pixels in the final image were roughly $56\,nm \times 56\,nm$; close to the largest possible size to allow diffraction-limited imaging. For MSIM/eMSIM it is best to be close to this limit as it maximises the sensitivity of the camera by not dividing the signal over more pixels than necessary, reducing the SNR. The ImagEM-X2 Hamamatsu camera had the largest pixels of all the cameras, measuring $16\,\mu m \times 16\,\mu m$. While not a significant increase over the iXon camera, when placed directly onto the camera port of the microscope, pixels in the images acquired measured $69\,nm \times 69\,nm$. These pixel sizes were too large to allow diffraction-limited imaging, meaning

additional optics were required after the microscope to magnify the image. When adding magnification optics to the detection branch of a microscope, it is important to consider that any optics will introduce aberrations into the image and degrade image quality. The simplest zoom system that can be used to increase the magnification is a Keplerian or Galilean telescope arrangement of two lenses. These simple lens systems form the basis of the earliest compound microscopes and telescopes but generally perform poorly in terms of aberrations, specifically spherical and chromatic aberrations. To minimise aberrations, and allow for varying magnification, a more complicated Angenieux lens system was used. This combination of lenses performs very well in terms of aberrations and is the basis for many lenses used in commercial cameras. The Angenieux lens system is a variable-zoom, variable-focus lens system, meaning the magnification and focus of the image can be adjusted while keeping aberrations to a minimum. It also has the advantage that its compact nature means it can be easily fitted on

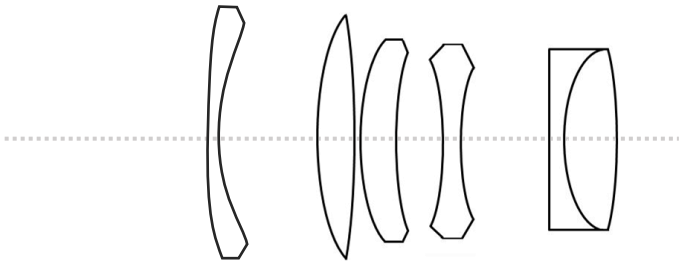

Figure 5.10: Angenieux lens system

The lens system consists of five lenses in total. From left to right: a negative meniscus lens, a best-form lens, a positive meniscus lens, a biconcave lens and a cemented achromatic doublet. The back four lenses form one lens group and changing the distance between this group and the image changes the magnification. Once the magnification has been fixed, the focus of the image onto the camera is changed by moving the first meniscus lens. Being able to change the focus and magnification without moving the camera is ideal in optical design where a camera needs to be firmly fixed down.

an optics bench with tight space constraints. The variable-zoom nature of the lens system allowed for the optimal magnification to be chosen for the EMCCD camera, something not achievable with simpler lens systems. This lens system is ideal for imaging applications, as changing the magnification and zoom requires only the lenses to be moved, allowing the camera to be firmly fixed in place. The Angenieux system is also useful as

the movement of the lenses required to change the magnification and zoom is several millimetres, making it less sensitive to movement than other systems. Such reduced sensitivity makes aligning the system easier. The disadvantage to using this more complicated lens system is that each optical element will reduce the light reaching the camera. For the anti-reflection coating, the stated transmission of each element is ~97% meaning a total transmission for the system of ~88%. Although this represents a loss in the transmitted signal, total transmission was still sufficient to allow for imaging at high framerates.

5.3 Software control

In order to control the hardware, software was written in both MATLAB and LabVIEW. The goal of this project was to demonstrate the potential of holographic projection and eMSIM for biological imaging. One important part of this was to ensure that the system constructed could be controlled in a user-friendly fashion by someone with little knowledge of optics or hardware control. To achieve this, hardware was controlled through

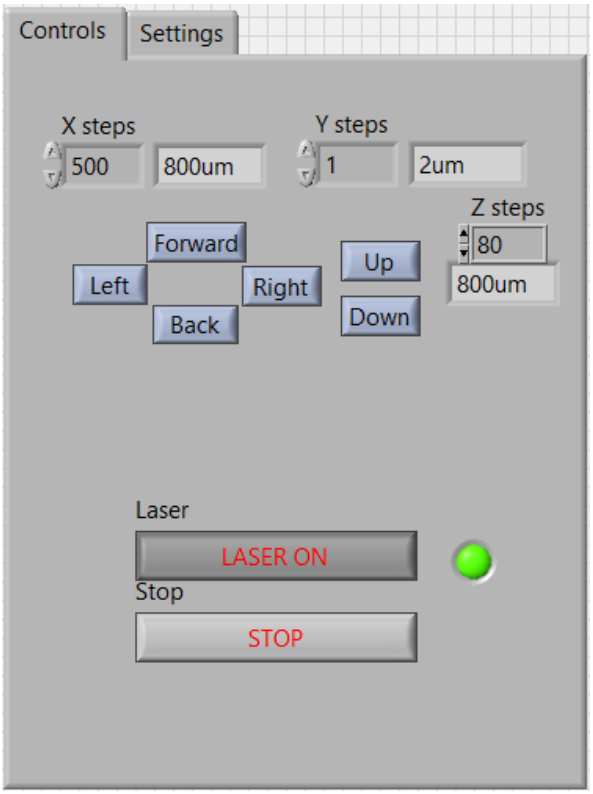

Figure 5.11: Front panel used for Olympus microscope control.

This GUI shown was used for control of the Ludl stage and focus motor. This GUI also incorporated basic control of the lasers.

LabVIEW and integrated into an easy-to-use Graphical User Interface (GUI). This is shown in figure 5.11. Control of the Ludl stage and focus drive was achieved through RS232 serial commands. For the Lecia frame, simple serial commands were not available for the control box. Instead, more complicated programming was required, as the control box uses a hierarchical approach to hardware control. That is, the hardware is split into groups and/or subgroups which must all be specified and checked for each command. To simplify the process, the micromanager Application

Programming Interface (API)[111] was used. Micromanager is an open-source software package built for the control of a number of microscope systems and accessories. As the necessary programming work had been completed to manage communications with the Leica microscope using micromanager, control of the scope was achieved by calling micromanager functions in LabVIEW. Although a more convoluted approach, this method simplified the process, as rewriting the code for LabVIEW was not required. Figures 5.12-5.16 show the separate GUI for control of the

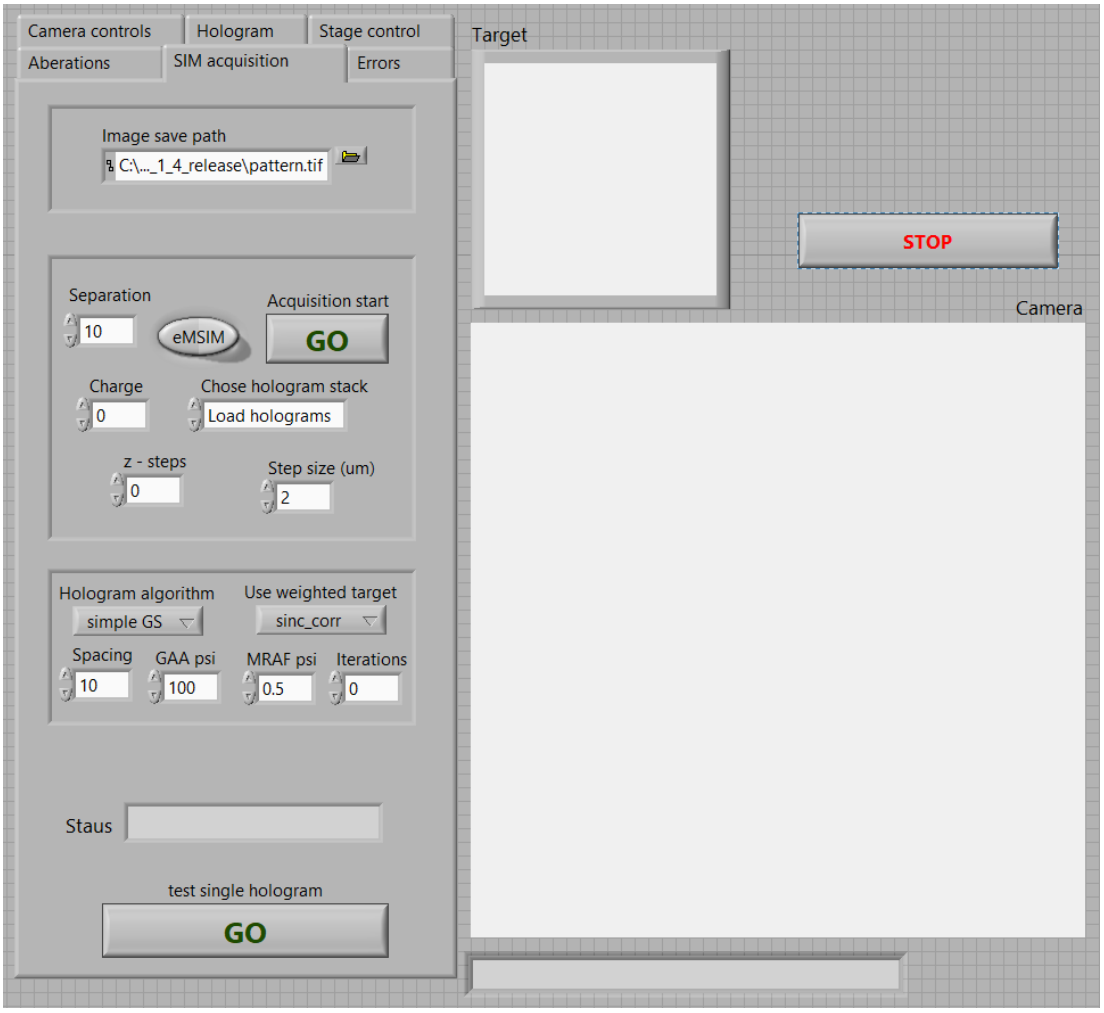

Figure 5.12: Front panel for holographic projection.

This GUI shows the full version of the program used to control holographic projection. For ease of use, camera control, aberration correction, algorithm selection and acquisition parameters are all integrated into the same program. The SIM acquisition pane contains all the controls necessary to choose the parameters for the hologram. GS and GAA algorithms were left into the program as they acted as quick ways to generate simple holograms for calibration.

holographic projection and MSIM/eMSIM image acquisition. This is the full version of the program and was used for the testing of holographic

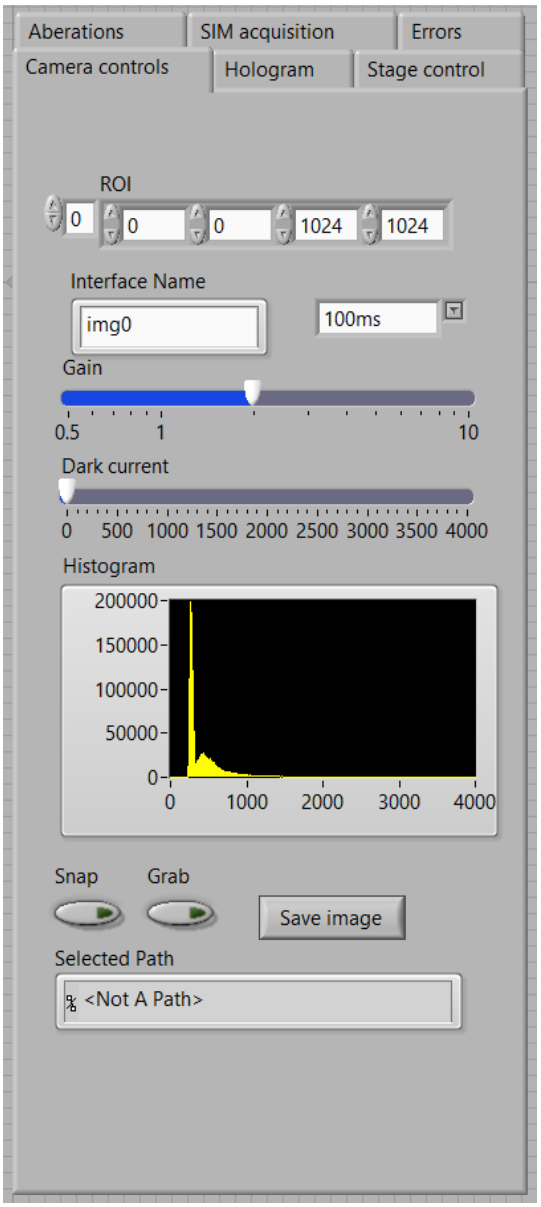

Figure 5.13: Camera control pane.

This page was used for control of the osprey camera through the NI cameralink board. The LUT can be visualised in real-time and the ROI, gain, dark current and exposure time can all be controlled.

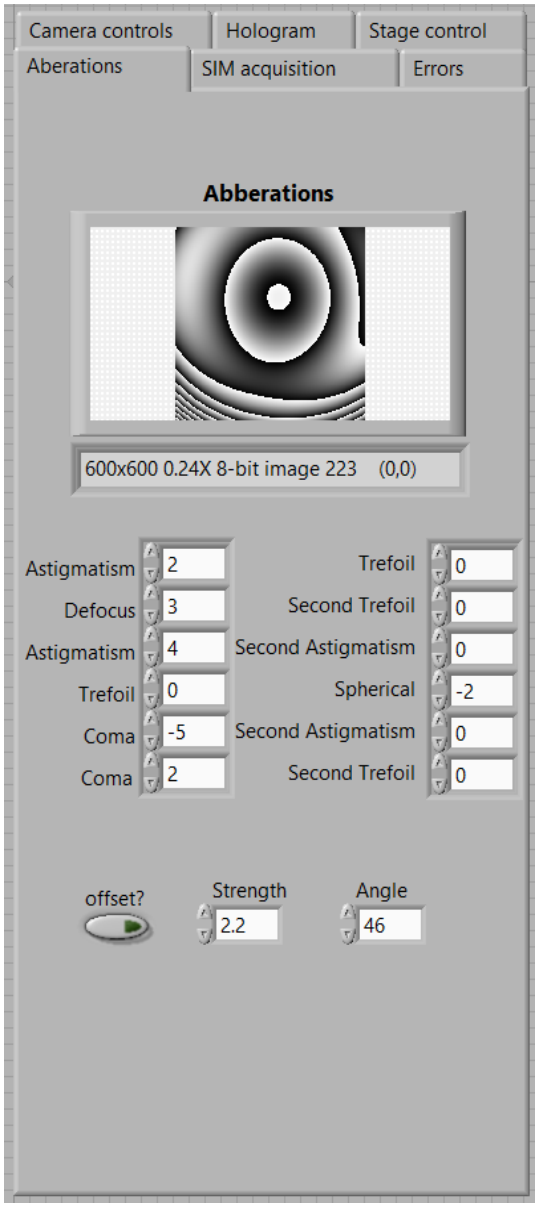

Figure 5.14: Aberration control pane.

This page was used for compensation of aberrations in hologram calculation. All the aberrations are controllable in real-time as a change in any value automatically updates the projected hologram. The option to include the offset to move the projection away from the focal centre is also controlled on this plane. For simple error checking, the aberration correction phase mask can also be visualised.

projection. The majority of the code for aberration correction, SLM calibration and hologram calculation was generated in MATLAB for ease

of construction. Running portions of the code through MATLB also allowed for acceleration

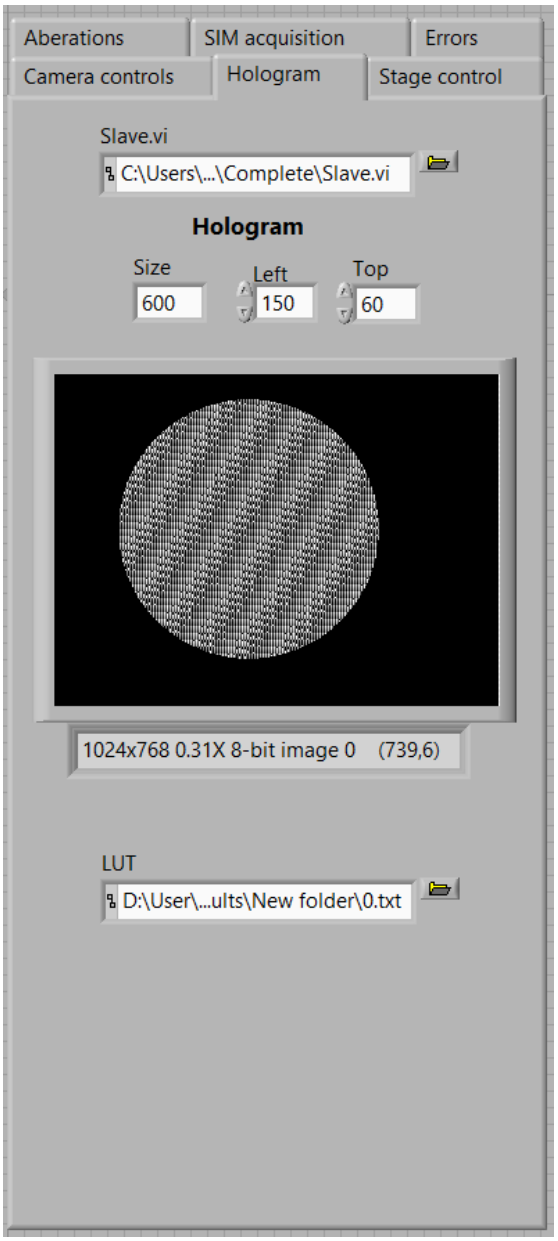

Figure 5.15: Hologram control pane.

This page was used for control of the hologram projection sub-vi. This 'slave' sub-vi ran in the background and acted to control the image on the second monitor of the PC, i.e. the image on the SLM. The location of the hologram on the SLM as well as the size of the hologram were all controllable. This page was also used to load the correct LUT for the hologram projection.

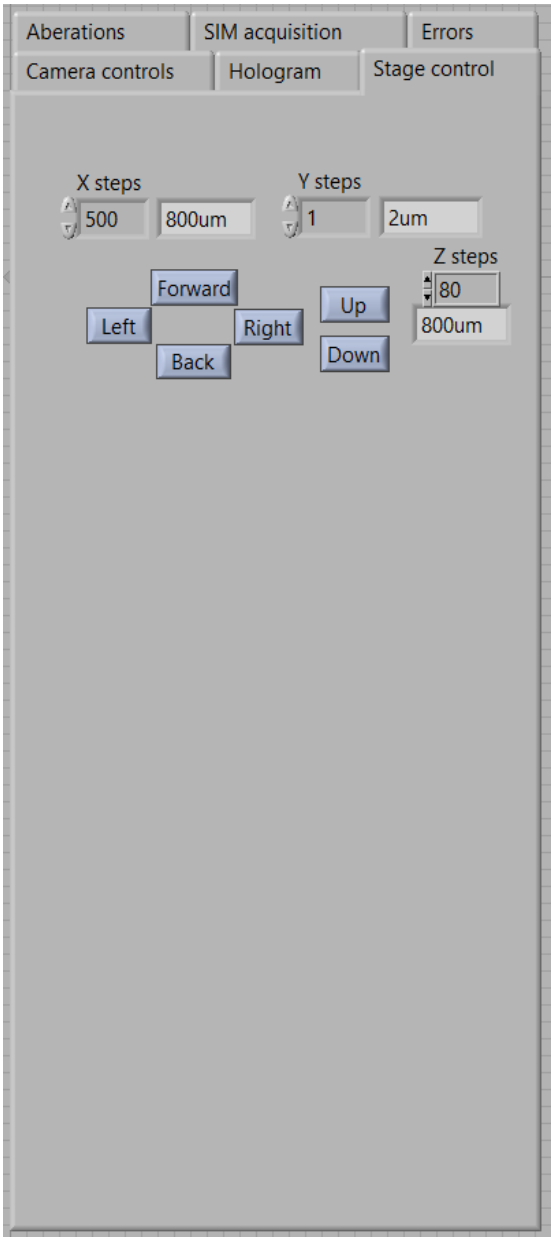

Figure 5.16: Stage control pane.

This page was used for control of the microscope stage. This version of the LabVIEW program was built to control the Leica chassis and, as the control was run in the background by the micro-manager API, no additional controls were required.

of the program using the GPU, which would have been difficult to achieve in LabVIEW. Laser control and camera triggering was done directly in

LabVIEW through outputs from a DAQ card. LabVIEW was used as a front end for all this code, integrating it into one standalone program for the ease of use for untrained users. If this program is to be developed further, one area for improvement is the expansion of the microscope body control using the micromanager API. In the current form, only the stage position is controllable, and no feedback is given to the user on the status of the microscope. Micromanager allows for much more sophisticated control of the hardware including the brightfield lamp and internal shutters in the microscope. To better develop the holographic projection software, it would be useful to include these controls in the LabVIEW program and offer feedback to the user on the status of the microscope as well as simple configuration information, for example stage position and internal light path configuration.

5.4 Platform testing

Once the system was constructed, platform testing and calibration was undertaken to maximise the quality of pattern projection.

5.4.1 Camera scale calibration

The camera scale was determined by averaging measurements of a calibrated ruler slide. This data was used to confirm that the imaging system satisfied the Nyquist criteria.

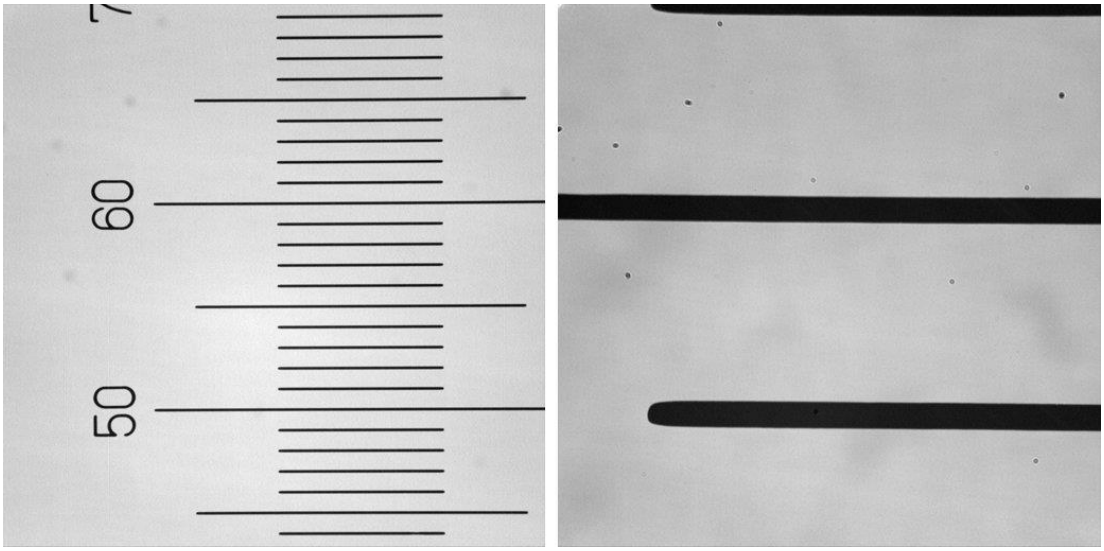

Figure 5.17: Images of camera scale calibration.

Typical images acquired for calibrating camera scale. Left: calibration slide viewed under a 10 X objective. Right: same region of the calibration slide viewed under a 100 X objective. Small bars are 50 μm.

5.4.2 Sinc envelope correction

When using any SLM, the shape of the pixels must be considered. For the LC SLM used, each pixel requires an electrical connection with the SLM driver, which is achieved using thin wires running between the pixels. This means that the borders of the pixels are opaque and the SLM does not have a 100% fill-factor, i.e. less than 100% of the light incident on the SLM is transmitted through a pixel. The first issue this leads to is that the SLM behaves as a 2D diffraction grating. This scatters images of the SLM away from the central image where the beam passes through. Although this loses approximately 50% of the incident light, efficiency is still high enough for MSIM/eMSIM imaging.

The second – and more disruptive – effect the imperfect fill factor has is to introduce variations in pattern uniformity. This can be demonstrated by considering the simplified model of beam focusing (figure 5.18). Ignoring the phase change of the SLM, the amplitude profile of the beam after passing through the SLM is a series of squares, i.e. the pixelated hologram is a convolution of the hologram with a square pixel. Given that the focal plane is the Fourier transform of the hologram plane, this convolution

becomes a multiplication of the Fourier transforms of the hologram and square pixel, i.e. the multiplication of the multi-spot pattern with a sinc function. As the intensity of the sinc function drops off from the centre, the outer spots show a reduced intensity. This is demonstrated in figure 5.19. For MSIM and eMSIM, a uniform intensity in spots is required for proper imaging. This variation from uniform intensity would introduce artefacts into the final reconstructed image. To account for this, a sinc envelope correction was built into the DS algorithm. By altering the cost function, the hologram can be optimised to generate spots whose brightness increases from the centre.

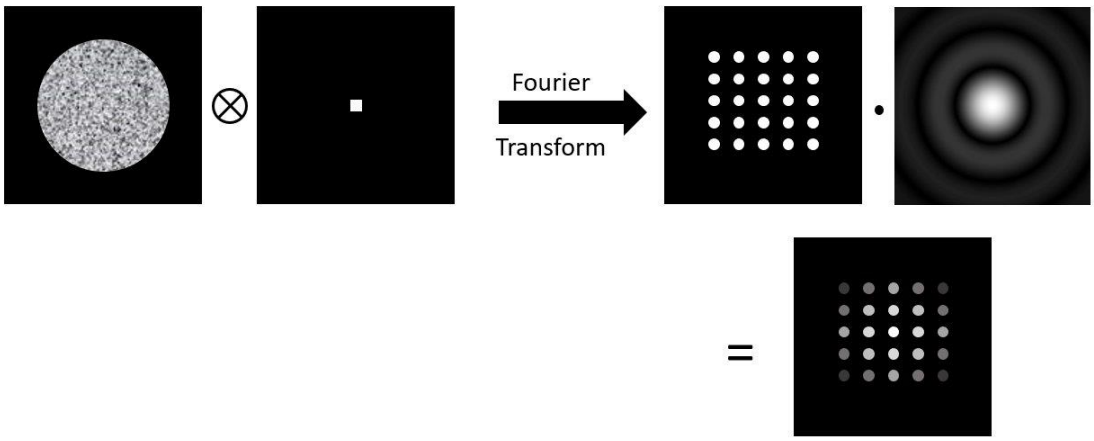

Figure 5.18: Origin of the sinc envelope.

Left side of the Fourier transform: the SLM, being made of square pixels, is the convolution of the hologram and a square with the same size as the pixels. Right side of the transform: the focal plane is calculated by taking the Fourier transform of the hologram. This is equivalent to multiplying the Fourier transform of the hologram (multi-spot pattern) and the Fourier transform of a square, a 2D sinc function. The bottom-right figure shows the final pattern projected in the focal plane, with the intensity of the outer spots attenuated by the sinc envelope.

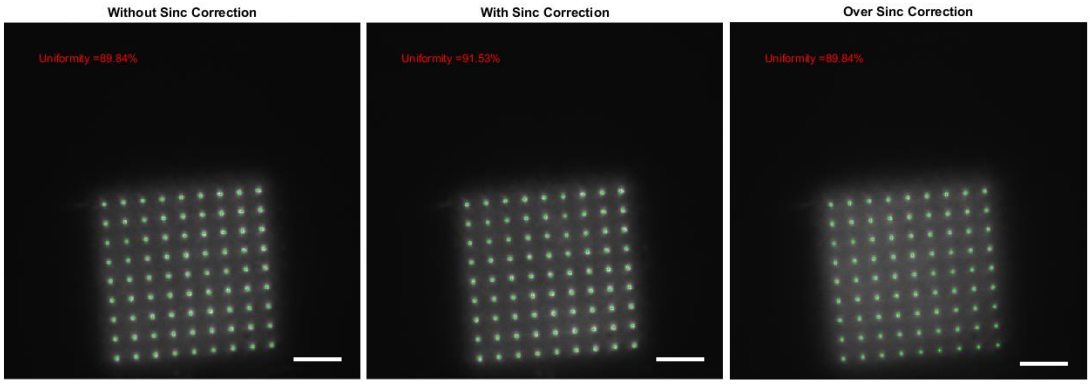

Figure 5.19: Sinc envelope correction.

Left: The pattern projected without sinc correction. Middle: The pattern after sinc correction. Right: The pattern with excessive sinc correction to better demonstrate the radial intensity variation. Uniformities of the spots are shown above each pane. The centre of the sinc envelope is the central focus of the objective lens. Since the spot pattern is deflected away from this point to block diffracted light, the sinc envelope manifests as intensity variations from the top-left to the bottom-right of the pattern. Scale bars are 5 μm.

When the hologram is used in the microscope, the effect of the sinc envelope reduces the intensity of the outer spots, giving an overall uniform illumination. Figure 5.19 shows the effects of the sinc correction applied to the holograms.

5.4.3 Spot aberrations

Aberrations were determined by analysis of the pattern projection onto a fluorescent rhodamine monolayer. The aberrations in the spots at the four corners of the pattern were measured. From this, the variation of aberrations across the FOV was extrapolated. This was then fed back into the DS algorithm and a new hologram calculated. Due to chromatic aberrations in the projection optics and inconsistent filter cube alignment, aberrations were different for each of the colour channels. To compensate for this, a separate hologram was calculated for each excitation colour.

Aberrations were measured on a mixture of spot and doughnut grids, as each PSF is differently affected by different aberrations, i.e. certain aberrations are more apparent on one PSF than another.[100,112]For example, small coma and astigmatism aberrations are difficult to distinguish on Gaussian excitation spots, but have very noticeable differences on doughnut excitation spots.

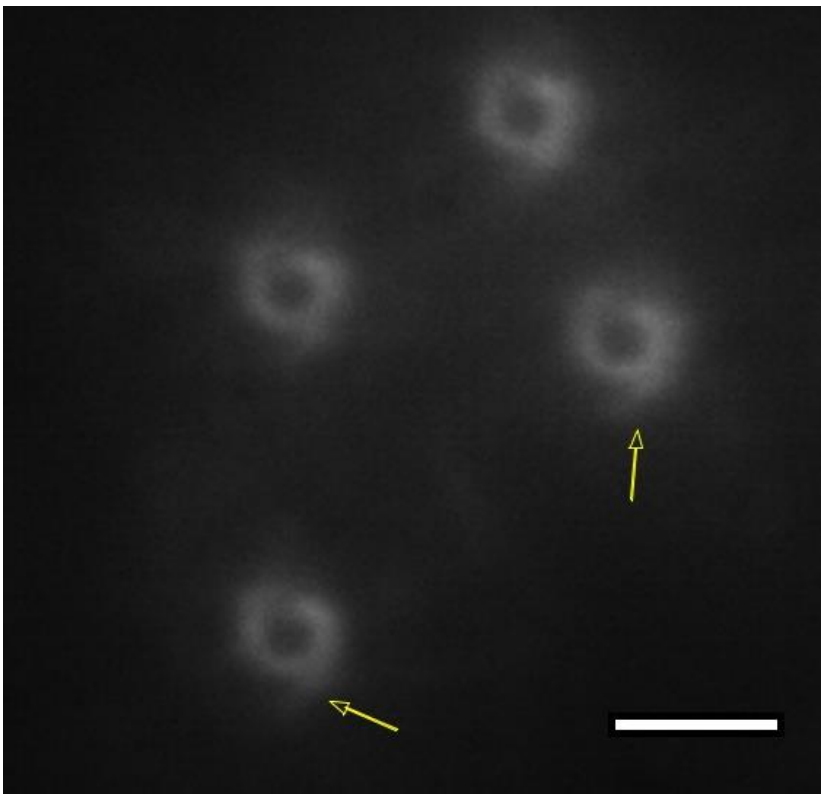

Figure 5.20: Aberrations viewed on doughnut PSF.

Projection of a cluster of doughnut PSFs with an $l = 6$ spiral charge. Yellow arrows show a tail on the bottom side of the PSF. On the opposite side of the doughnut is a darker region in the ring. This suggests an astigmatism in the excitation pathway. Monolayer was excited with 488 nm excitation light. Scale bar is 5 μm.

Astigmatism on a doughnut appeared as a tail on one edge of the spots, whereas coma resulted in a smearing of the doughnut in one direction. Likewise, defocus and spherical aberration are less apparent on doughnut PSFs[99] but more easily distinguished on Gaussian spots.

5.5 Summary

In this chapter the details of the optical setup have been described. The software used throughout as well as the methods used to characterise and calibrate the system have also been detailed. The use of a commercial projector to provide the phase-mostly SLM means that, by following these methods, existing optics labs would be able to construct easily the instrumentation necessary for holographic projection. This would allow for not only eMSIM imaging but also a range of other studies requiring flexible and high-precision patterned illumination. This work has also formed the basis of a currently accepted manuscript, summarising the optical methods and making available the software used to drive the components.[113]

6. Image processing

Summary: *this chapter aims to describe the image processing methods used for this project. Building on the previously-described theory of image processing in structured illumination techniques, it will provide a justification of the methods used and a description of their programmatic implementation.*

6.1 Introduction

All SIM requires extensive image processing to recover the super-resolution image. The basic steps are pre-processing of the data, estimation of the excitation patterns and image deconvolution.

6.2 Post-acquisition pattern estimation

Pattern estimation is one of the most important steps in any SIM methodology. There are two principle ways in which pattern estimation can be achieved: pre-acquisition calibration and post-acquisition estimation. Each of these has its advantages and drawbacks and, in many instances, only one of the approaches may be possible with the available data. While being technically the most complex approach, post-acquisition strategies have the advantage that they are less susceptible to system drift and sample-specific distortions in the illumination pattern. Broadly, post-acquisition strategies can be split into two categories based on whether they determine the pattern in real or frequency space. Across the field of SIM, frequency space methods are by far the most common way to determine the excitation pattern. This is because of their versatility and relative insensitivity to noise in the image. This is especially true of striped-pattern SIM where the pattern is visualised as a set of sharp peaks.

6.2.1 Pattern spacing estimation

Pattern spacing estimation can be achieved in either frequency or real space. For multi-spot patterns, where in real space the pattern is defined as a 2D delta-comb, in frequency space it is also visualised in the same way. This is shown in figure 6.1. The spacing between the spots in real space is determined by the spacing between the maxima in frequency space. Since all the spots in the real space image contribute to each peak in frequency space, this method is less susceptible to minor fluctuations in the apparent spot spacing resulting from different regions of the sample being illuminated. However, frequency space methods put certain constraints on the sample. If the sample contains regular repeating structures, such as aligned filaments or resolution bars, these structures generate their own peaks in frequency space.

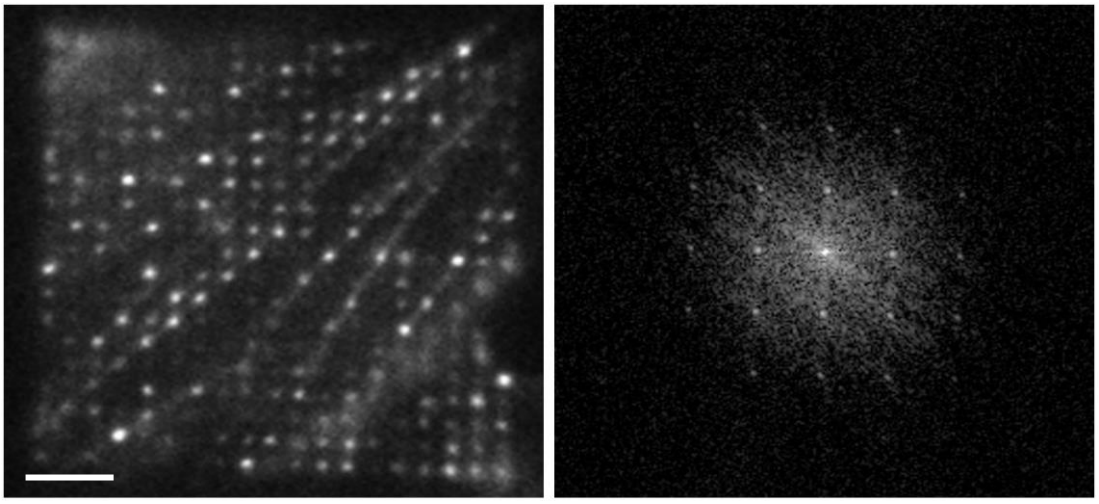

Figure 6.1: MSIM FFT.

Left: Typical MSIM raw data. Right: magnified log FFT of the raw data. The multi-spot pattern is again visualised as a 2D delta-comb. Scale bar is 5 μm.

In contrast to frequency methods, real space estimation has fewer constraints on the underlying sample structure, although offers a more computationally intensive problem. For eMSIM, pattern spacing was estimated using newly-developed real space methods. This was achieved with image auto-cross correlation: shifting the image over itself and determining a measure of image similarity. When the shift gives a

maximum in similarity it means that there is overlap of adjacent excitation spots. From this, the pattern spacing can be extracted as the shift vector with the maximum similarity. This process was repeated for every 10 images acquired and the average spacing (excluding outliers) was calculated. Before performing the shifts, images were filtered by finding local maxima and using the images of local maxima for the shift. This is shown in figure 6.2. This method for spacing estimation proved robust on all the model data tested.

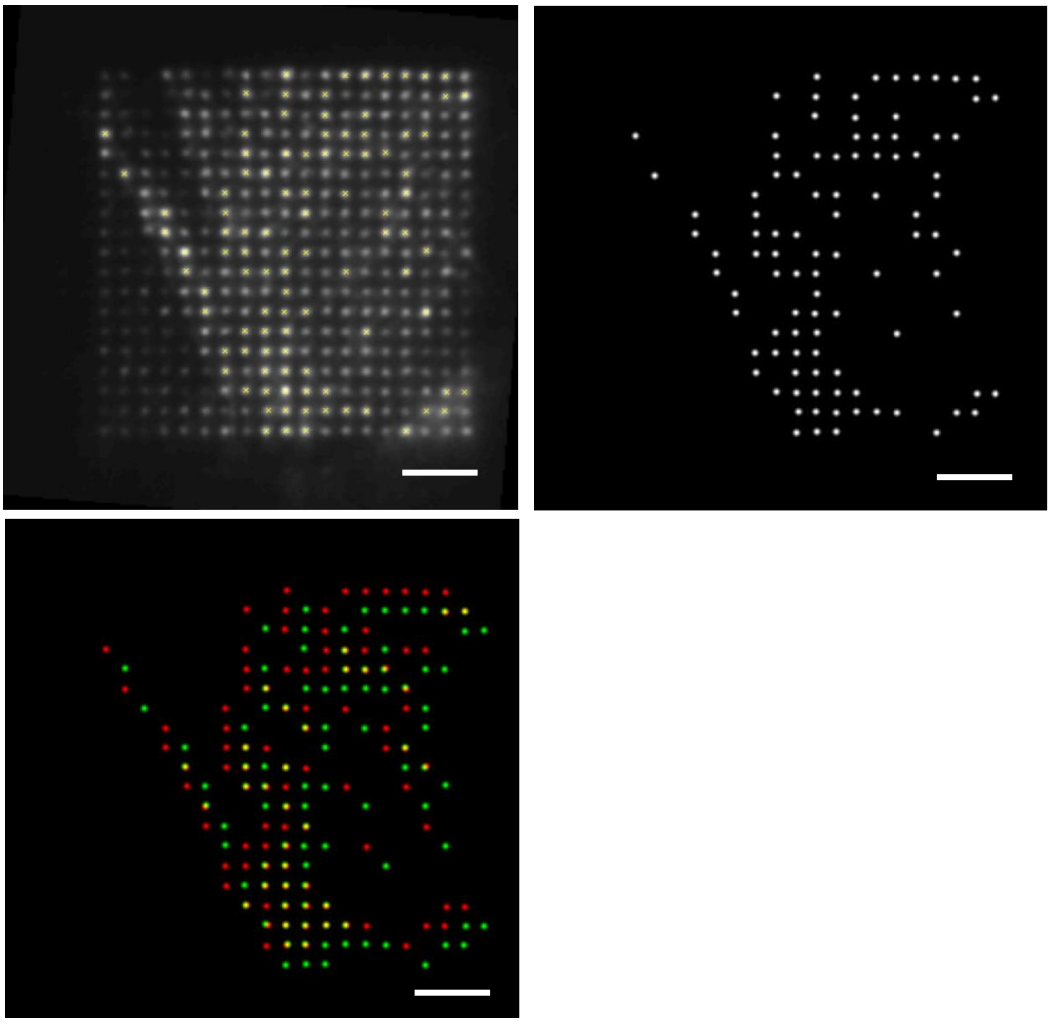

Figure 6.2: Pattern estimation overlay.

Top left: The local maxima are found in the acquired image. Top right: A filtered image is constructed by inserting PSFs at the coordinates of the maxima. Bottom left: The filtered image is shifted over itself pixel by; when the spots align the similarity is maximised. The shift that gave the highest similarity corresponds to the approximated value for the pattern spacing. This process is repeated for every 10^{th} frame. The from the ~10 estimates, the lowest 3 and highest three values are removed to prevent outliers affecting results. The average of the remaining shifts is then taken. Scale bars are 5 μm

From the spacing values, an ideal pattern was generated by inserting the estimated PSFs at regular intervals in the model pattern, separated by the calculated spacing.

6.2.2 Pattern shift estimation

Once the pattern spacing has been determined, the next step is to determine the shift of the pattern. To do this, an ideal stack of shifted patterns was generated from the single ideal pattern previously calculated. By shifting each frame in the ideal pattern stack by a fixed amount relative to the previous frame, it is possible to constrain uniform illumination. This constraint is essential for MLD of SIM data, as discussed in Chapter 2. Once this ideal stack of illumination patterns has been generated, it is necessary to determine the global shift of the patterns relative to the sample.

The x and y shifts which are scanned over are equal to the pattern spacing, as this is the maximum distance which the ideal pattern can need to be shifted. This method for calculating the pattern shifts was the most reliable of any method tested or previously reported, since it calculates the error based on every frame acquired. The cost of this is in computational time, as the inner loop is a complicated series of calculations which must be computed several hundred times. To allow for reasonable calculation times, the process was heavily optimised for GPU processing. Final calculation time for this step was typically $5 - 10\,s$; faster than other, simpler methods currently available.

6.2.3 Finalising pattern estimation

The above method for determining spacing and shift was effective on model test data used. However, the method proved difficult to implement on real-world data. The reason for this was determined to be sub-pixel accuracy on pattern spacing and small errors in pattern rotation. The pattern spacing is determined by shifting the filtered images over themselves and looking for a maximum similarity. The issue with this method is that the images can only be shifted by an integer number of pixels. With the model data, patterns are built by inserting PSFs at regular intervals, crucially separated by a whole number of pixels. For this reason, the shifting method is effective since it can exactly match the pattern spacing. However, in real-world data the pattern spacing may not be a whole number of pixels. The average of multiple images is used to account for this, and works well if the true pattern spacing lies evenly between two integer shifts. For example, if the true pattern spacing is $10.5\,pixels$, the

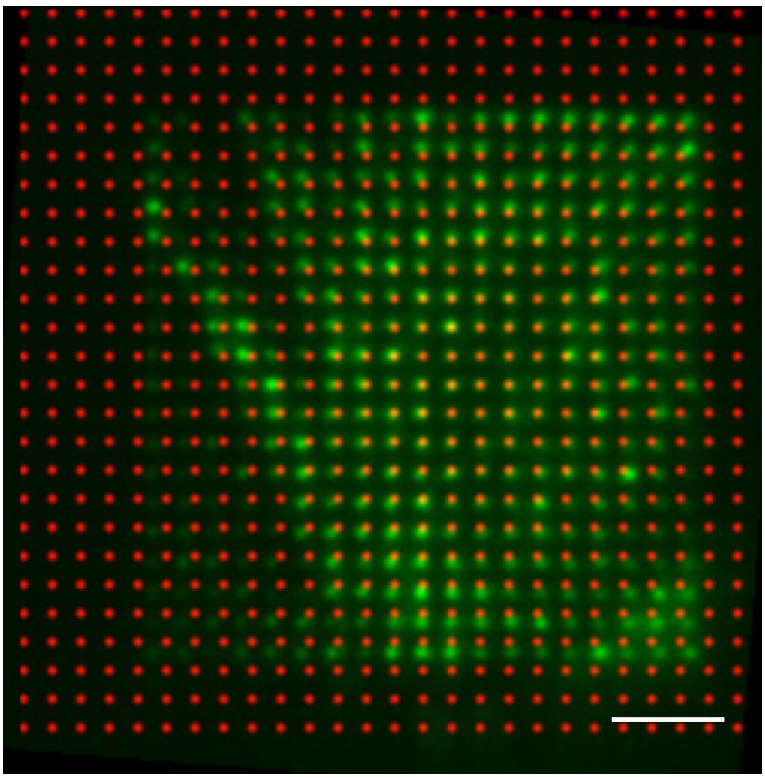

Figure 6.3: Pattern spacing error.

The true pattern spacing is 19.34 *pixels* and the shift method has estimated a spacing of 19 *pixels*. In the centre of the pattern, the spacing error has had minimal effect, though as distance from the centre increases, so does the pattern error. Scale bar is 5 μm.

shifting will estimate the spacing as 10 $pixels$ and 11 $pixels$ roughly an equal number of times, and the average spacing will be calculated correctly as 10.5 $pixels$. However, if the true pattern spacing lies significantly closer to one integer than another, for example 10.15 $pixels$, the shifting method will always find a minimum at 10 $pixels$. While the small difference – typically $0.1 - 0.3$ $pixels$ – would not be significant when looking at smaller areas, over the extended FOV used in holographic projection, this difference becomes very noticeable and degrades MSIM/eMSIM reconstruction. Figure 6.3 shows an example where the pattern spacing has been estimated incorrectly by a sub-pixel amount.

To address this issue, a method was developed to correct for sub-pixel errors in pattern spacing and minor rotation. The approximated spacing and pattern shift allows for matched features to be determined in the ideal pattern and acquired image. Figure 6.4 shows these matched features. The scaling, rotation and minor shift changes can be described by the nonreflective similarity transform, $\boldsymbol{T}$. This is represented such that coordinates of a maxima in the ideal pattern [x y] are transformed to the coordinates in the acquired image [u v], i.e.

$$[u\ v] = [x\ y\ 1]\boldsymbol{T} \qquad \text{Eq. 6.1}$$

where the transform matrix, $\boldsymbol{T}$, is given by:

$$T = \begin{bmatrix} s \cdot \cos\alpha & -s \cdot \sin\alpha & 0 \\ s \cdot \sin\alpha & s \cdot \cos\alpha & 0 \\ t_x & t_y & 1 \end{bmatrix}. \qquad \text{Eq. 6.2}$$

Here, α is the angle of rotation; t_x and t_y are the x and y translations respectively; and s is the scale factor. Matching the maxima in the image with the nearest spot in the ideal pattern gives a pair of points in equation 6.1. By finding a number of points in the images, the angle and scale factor can be determined. Once these values have been obtained, the raw images are rotated by $-\alpha$ to correct for rotation, and the spacing previously

determined by the shift method is multiplied by the scale factor to give the sub-pixel pattern spacing.

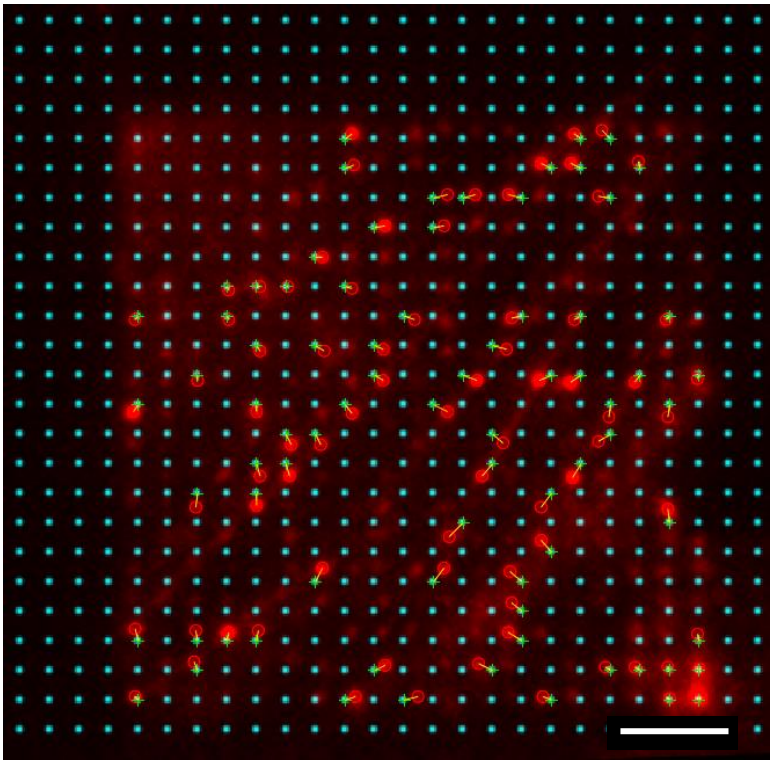

Figure 6.4: Matched features in the raw data and ideal pattern.

Red: raw imge. Cyan: ideal pattern overlay. Red circles show local maxima of the raw image and green crosses indicated the nearest maxima in the ideal excitation pattern. Scale bar is 5 μm.

6.2.4 Pattern aberration estimation

As well as aberrations in individual excitation PSFs (Chapter 4), projection aberrations and imperfect detection optics introduce skew into the projected pattern. An extreme example of this is shown in figure 6.6 where poorly aligned optics have resulted in a notable skewing of the pattern. For many of the images acquired, the system was sufficiently well aligned, and this step was not required. However, for a few of the images, especially those acquired with the Hamamatsu EMCCD, pattern skew prevented proper image reconstruction. The skew resulting from imperfect alignment can be described by a 2nd order 2D polynomial transform. For a point in the ideal pattern $\vec{r}_{ideal} = (x, y)$, the corresponding point in the real projected pattern $\vec{r}_{real} = (u, v)$ can be determined by the polynomials

$$u = A(1) + A(2)x + A(3)y + A(4)x^2 + A(5)xy + A(6)y^2 \quad \text{Eq. 6.3}$$

and

$$v = B(1) + B(2)x + B(3)y + B(4)x^2 + B(5)xy + B(6)y^2. \quad \text{Eq. 6.4}$$

Here, A and B are vectors of length 6 which define the coefficients of the 2D transform. An example of pattern skew is shown in figure 6.5.

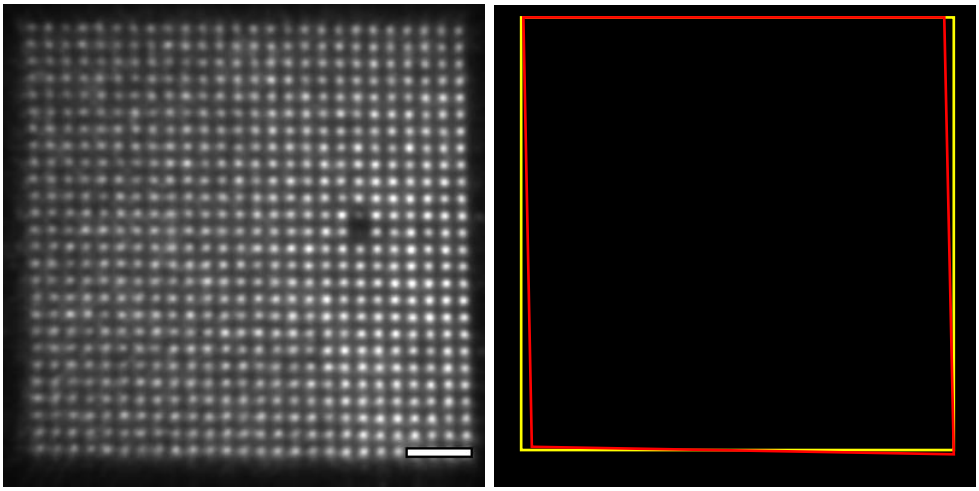

Figure 6.5: Pattern aberration error.

Left: raw image collected. Right: overlay of ideal square (yellow) and measure outside border of projected pattern (red). Scale bar is 5 μm. Although the pattern deviation is small (<1 μm), this error would prevent correct image reconstruction.

Determining the skew and rotation coefficients requires multiple matched points in the images of projected patterns and ideal patterns. A local maxima finder was used to extract the locations of points in both the ideal and acquired patterns. From this data, matched points were found by locating the nearest peak in the ideal pattern to a peak in the acquired images. Using the co-ordinates of these matched points, equations 6.3 and 6.4 can be solved using a least squares method to find values for the coefficients in the vectors A and$B$. Once the warping coefficients had been determined, the inverse of the warp was applied to each frame of the pattern stack. Values for A and B changed between images but typical values gave an effective rotation of less than one degree and a skew that corresponded to a 1 μm error across the FOV.

6.2.5 Pre-acquisition calibration

While not always preferable, the conditions imposed on sample structure for post-acquisition estimation can mean that pre-acquisition calibration is necessary. For example, in sparsely fluorescing samples or samples whose structures may impede pattern estimation, pre-calibrated patterns must be used. Pre-acquisition estimation involves projecting the excitation pattern onto a fluorescent monolayer, estimating the pattern and then saving the results. The principle issue with using saved patterns is that differences in the pattern between the monolayer and the sample result in reconstruction artefacts. The most common differences that occur are those resulting from differences between the refractive indices of the immersion media, the sample and the mounting media. For example, the images of the monolayer are all acquired at a fixed distance from the objective, i.e. the surface of the coverslip. In contrast, typical cellular structures that are imaged lie some distance above the coverslip surface, and light must travel through the mounting media between the imaging plane and the coverslip. As the light travels this extra distance, refraction has the effect of distorting any excitation pattern and introducing additional aberrations. Such distortions of the pattern would mean that the pre-acquired estimated patterns no longer align with the real excitation patterns at the sample, detrimentally affecting image reconstruction.

6.3 Image deconvolution

As is previously described, in MSIM and eMSIM, there exists no way to recover the super-resolution image directly in frequency space, as there is with striped-pattern SIM. As such, the image deconvolution was achieved using the JRL and PIFP methods described in Chapter 3. Once the patterns had been appropriately estimated or loaded from pre-acquisition, no alterations were required to the existing methods.

7. Imaging results

Summary: *this chapter aims to describe the results of the imaging experiments in the project. It will cover the steps of sample preparation and detail the samples used. After presenting the results, it will also discuss how these can be interpreted in the context of the project.*

7.1 Introduction

The final stage of the project was to test the developed imaging techniques in real-world applications. This involved imaging simple targets for calibration, as well as the imaging of biological structures in both fixed and live cells.

7.2 Sample preparation

Four targets were used for testing holographic projection and the eMSIM technique. The first of these was a fluorescent monolayer formed

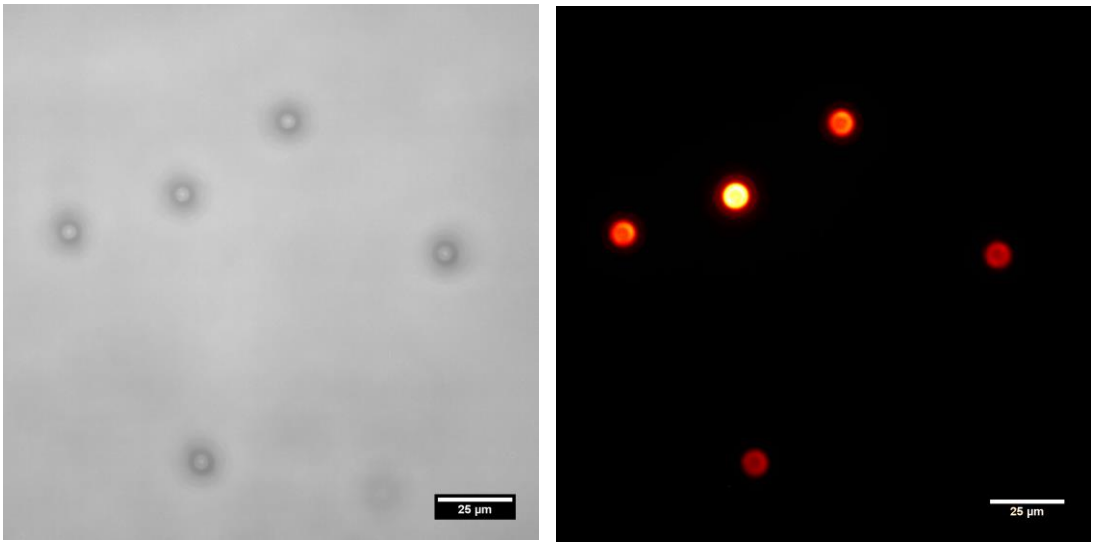

Figure 7.1: Fluorescent polystyrene beads.

Diffraction-limited image of a cluster of 4 μm beads. Left: Brightfield transmission light image. Right: False-colour fluorescent image captured under 532 nm laser excitation and 550 nm detection.

by drying rhodamine 6G onto a coverslip before mounting with refractive index-matching media and sealing with fast-drying nail varnish. This was used for alignment of the system as the uniform fluorescent response and thin fluorescent layer make imperfections in the illumination optics apparent and easily corrected. Once the system was calibrated, the sample was used to determine ideal illumination patterns for the processing of samples with sparse fluorescence.

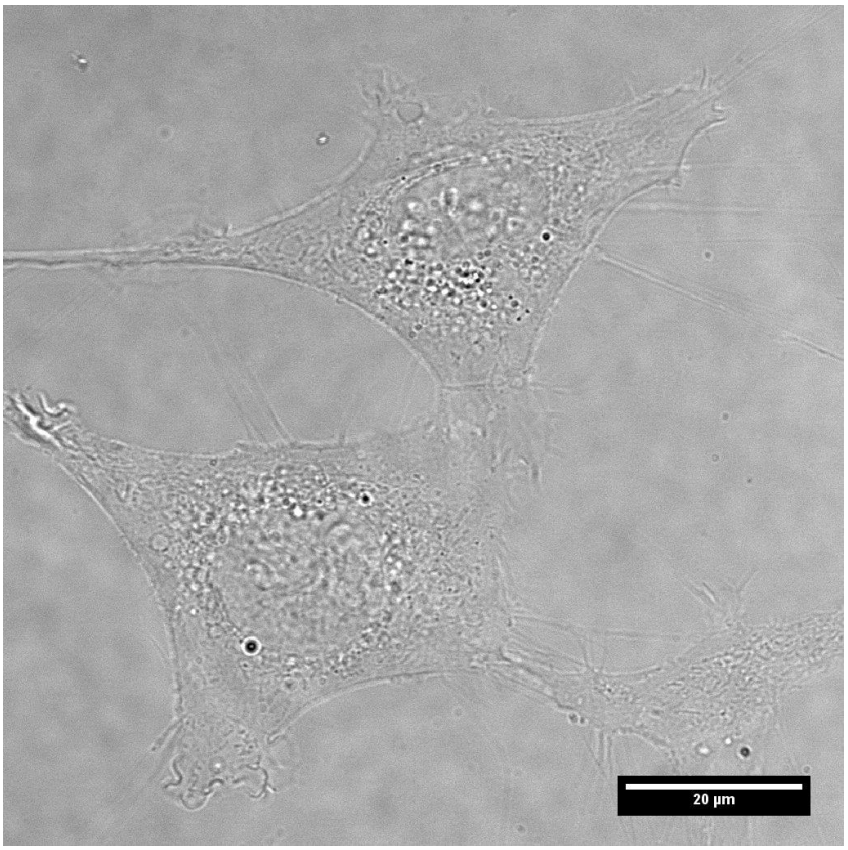

Figure 7.2: Fibroblast cells under transmission light microscopy.

Typical NIH/3T3 mouse fibroblast cells viewed under brightfield transmission light microscopy. The need for fluorescence labelling is highlighted by the lack of clear and discernible organelles in the cell.

The second target used was a layer of fluorescent polystyrene beads with diameters 4 μm, 500 nm and 100 nm. These beads were sparsely distributed onto a coverslip by drying a dilute solution containing the beads in suspension. The beads were also mounted in an index-matching media and sealed with fast-drying nail varnish. The beads were excited with 532 nm laser excitation, and fluorescence signal was measured after a 550 nm long-pass dichroic mirror.

The final targets used were fixed and live-cell slides. NIH/3T3 mouse fibroblast cells were incubated in Dulbecco's modified Eagle's medium and split every $2-4$ days to prevent the cell culture becoming confluent (i.e. limiting cell-cell contact), which hinders the use of protease enzymes to release cells from the culture surface. For the live-cell studies, Mito-Tracker Green (MTG) was used to selectively stain the mitochondrial network of the cell. As a dynamic network whose distribution changes over time, the mitochondria are an excellent target to test live-cell techniques, as high temporal resolution is required to obtain good quality images. Live cells were mounted in Phosphate-Buffered Solution (PBS). Although PBS cannot be used for the long-term imaging and culture of cells, for the short-term imaging studies it offered a simple imaging media with no background fluorescence.

The final target used was the actin cytoskeleton of fixed cells. Cells were fixed with paraformaldehyde and permeabilised with a weak detergent solution (0.1% Triton-X 100). Permeabilization was required as the actin stain (Alexafluor (AF)-488 Phalloidin) cannot pass through the cell membrane. To demonstrate the multi-colour capabilities of fluorescence microscopy (figure 1.3), a subset of the fixed cells were also stained with DAPI to label the cell nucleus.

7.3 Monolayer imaging

Images of the monolayer were captured throughout as a standard target for calibrating and aligning the system. Specifically, the monolayer was used to determine the coefficients describing the system aberrations and sinc envelope. It was also used to calibrate ideal patterns for pattern estimation. Figures 5.21 and 6.5 show two examples of pictures acquired through imaging of the monolayer for system calibration.

7.4 MSIM imaging with holographic projection

As a proof of concept for holographic projection, the first imaging studies carried out were MSIM imaging. These results have also formed the basis for pending publication on the technique. In these MSIM imaging experiments, spot patterns with a 16:1 separation ratio were used throughout. This meant a total of $16^2 = 256$ pattern shifts were used. Typical camera exposure times were 10-20 *ms*.

7.4.1 Micro-bead imaging

Imaging fluorescent microspheres is a useful way of determining many properties of an optical system. As a resolution target, they also offer a simple way to determine whether resolution criteria have been reached. Figure 7.3[113] shows the results of MSIM micro-bead imaging with holographic projection. 5 PIFP and 30 JRL iterations were used for reconstruction. While the FWHMa of the beads offers one resolution estimate, the intensity profile offers the most conclusive evidence of a true resolution increase. The choice to avoid measuring the FWHMa reflects the fact that excessive JRL iterations will artificially reduce the FWHMa without offering any further gain in resolution. Since there is very limited structure in the micro-bead samples, determining when to terminate the iterations is difficult as artefacts are less obvious in the reconstructed image. In contrast the line intensity profile is not affected in this way by excessive iterations and is therefore a more robust measure of resolution.

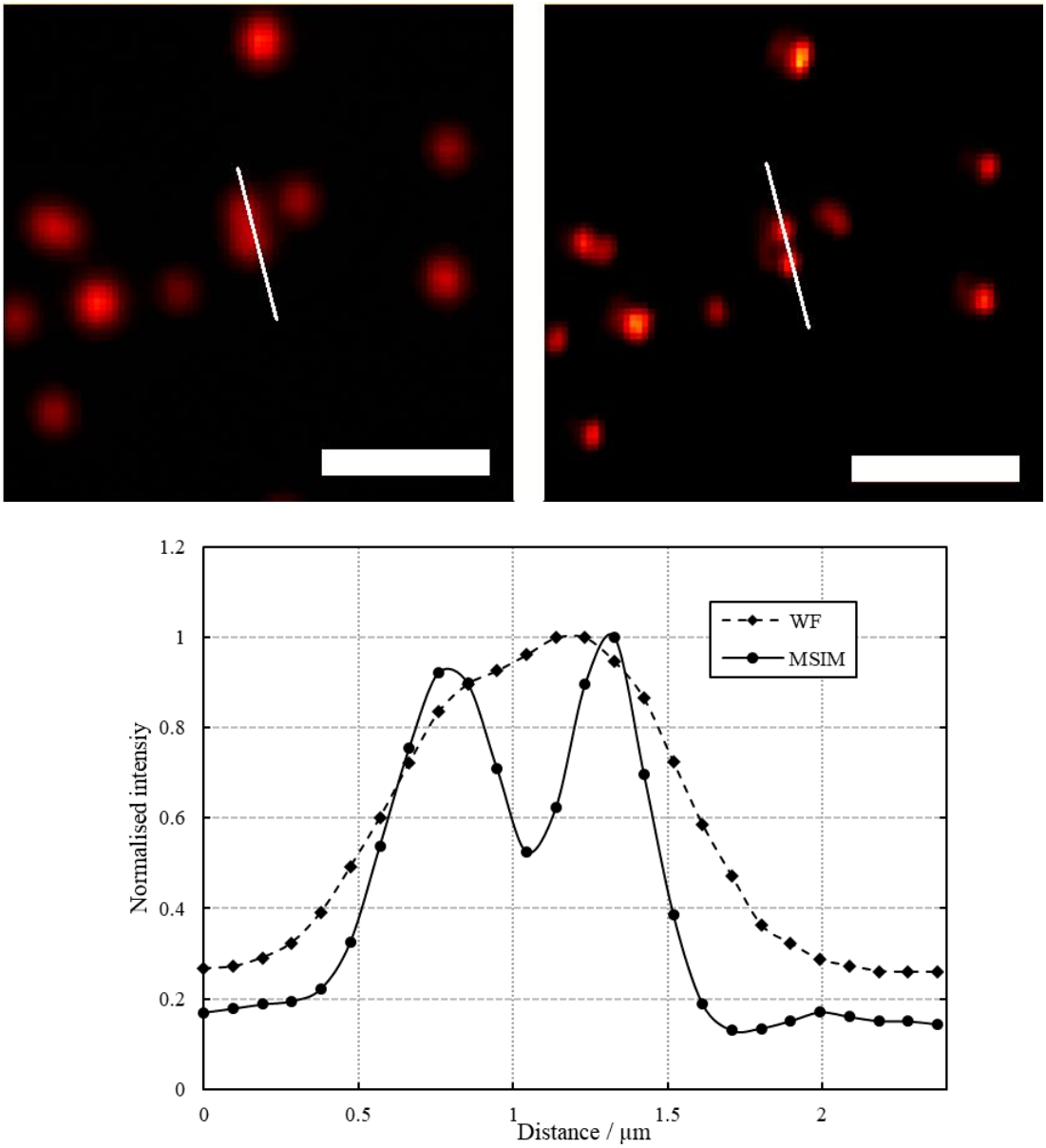

Figure 7.3: MSIM imaging of fluorescent beads.

Top left: Diffraction-limited image. Top right: MSIM image. Scale bar is 2.5 µm. Bottom: Intensity plot along blue line in both images. Beads were excited with 532 *nm* laser excitation. Emission was collected after a 550 *nm* long-pass filter. Adapted from Ward et al. 2019.[114]

7.4.2 Fixed cell imaging

While they offer a good target to measure resolution, microbeads are not indicative of most biological structures. To demonstrate that the resolution enhancement would be applicable to a wider range of structures of biological interest, the actin cytoskeleton of fixed cells was imaged. These results are shown in figures 7.4 and 7.5. In both sets of images, a significant resolution improvement is seen. This can be more easily seen in the line intensity plot as two filaments are clearly resolved in the centre of the line, though remain unresolved in the diffraction-limited image. As well as demonstrating the possible resolution improvement, these results also

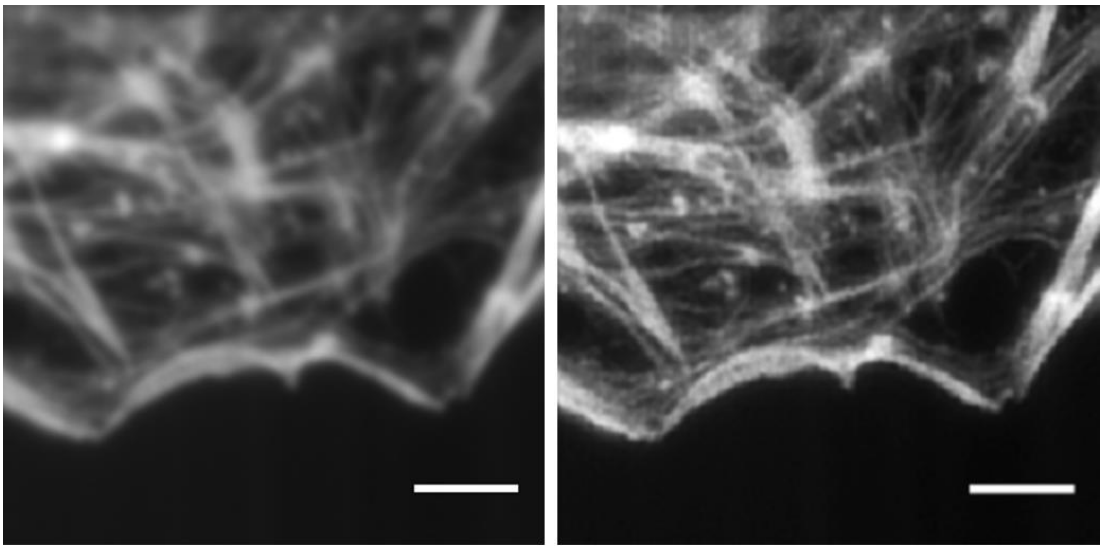

Figure 7.4: MSIM imaging of the actin cytoskeleton.

Left: Diffraction-limited image. Right: MSIM image. Scale bar is 5 μm. Cells were stained with Alexafluor-488 phalloidin to label the actin cytoskeleton. The label was excited with 488 nm laser excitation and fluorescent signal gathered after a 510 nm long-pass filter. Adapted from Ward et al. 2019.[114]

highlight some of the limitations of the technique. In the MSIM reconstruction shown in figure 7.5, a boxing artefact can be seen, with the image appearing to be composed of tiles. This is a result of the intensity of the spots in the raw images being artificially reduced to differing degrees in sequential frames. While such a tiling artefact would be present if photo-bleaching were reducing the intensity in sequential frames, the localisation of the artefact towards the upper left region of the image suggests an error in image reconstruction. Specifically, this suggests an improper pattern spacing estimation.

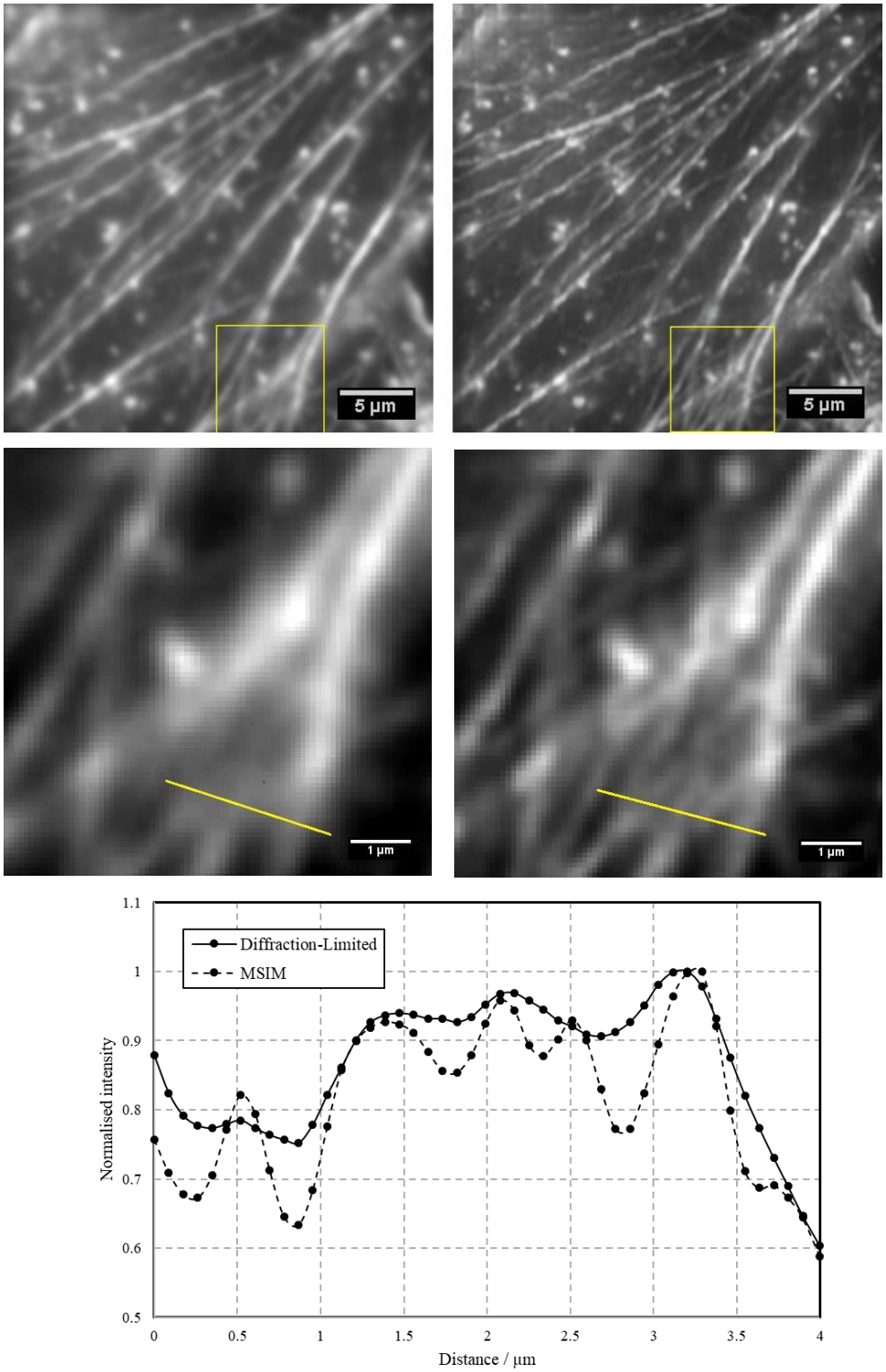

Figure 7.5: MSIM imaging of the actin cytoskeleton.

Top Left: Diffraction-limited image. Top Right: MSIM image. Scale bar is 5 μm. Middle Left: Zoom of area of diffraction-limited image indicated in full FOV. Middle Right: Zoom of area indicated in full MSIM image. Scale bar is 1 μm. Bottom: intensity plot along line shown in middle images. The dashed line represents MSIM imaging and the solid line shows diffraction-limited imaging. Cells were stained with Alexafluor-488 phalloidin to label the actin cytoskeleton. The label was excited with 488 nm laser excitation and fluorescent signal gathered after a 510 nm long-pass filter. Adapted from Ward et al. 2019.[114]

7.4.3 Live-cell imaging

The final, and perhaps the most important, test of MSIM with holographic projection is live-cell imaging. SIM is an attractive technique in biological imaging as the speed and limited light exposure make live-cell studies possible. To demonstrate that holographic projection allowed for rapid and non-phototoxic imaging, the mitochondrial network of live fibroblast cells was imaged. The results are shown in figure 7.6. Image reconstruction was performed using 30 PIFP and 30JRL iterations. Apparent in the image is the sharpening of the edges of the mitochondria, as well as the resolution of distinct mitochondria which appear merged in the diffraction-limited image. As a dense network, the diffraction-limited image of the mitochondria also contains a significant amount of out-of-focus light, especially in the region closer to the nuclear envelope. In the MSIM image however, a large amount of this out-of-focus light has been rejected by the digital pinholing, offering further apparent resolution increase over diffraction-limited imaging.

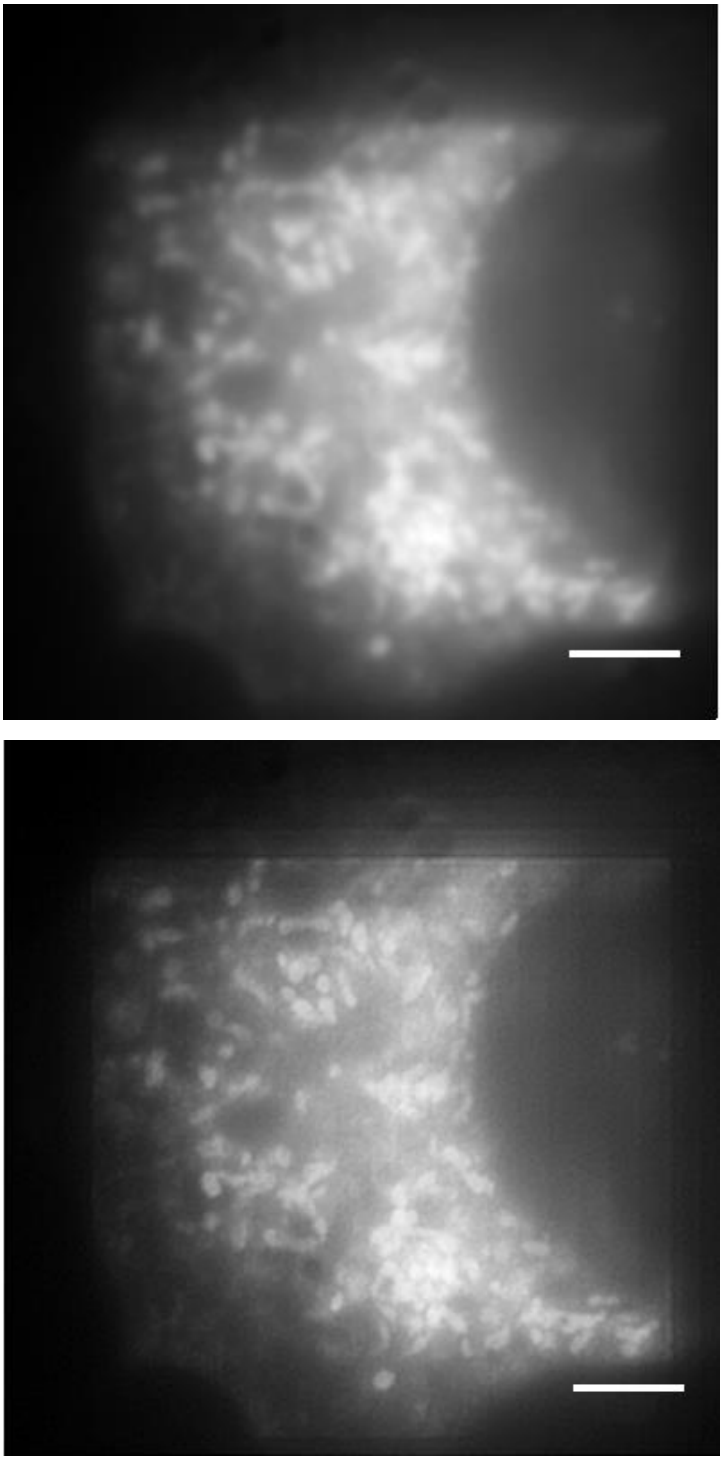

Figure 7.6: Live-cell imaging of mitochondria.

Top: Diffraction-limited widefield image. Bottom: MSIM image. Live cells were stained with MTG prior to imaging. MTG was excited with 488 nm laser excitation. Emission collected after 510 nm long-pass filter. Scale bar is 5 μm. Adapted from Ward et al. 2019.[114]

7.4.4 Analysis of MSIM imaging

Overall, the results of the MSIM imaging proved the efficacy of holographic projection. The first of these is the restricted imaging times. Unlike amplitude-only projection using a DMD, holography requires the rotation of liquid crystals in a cell rather than the rapid movement of mechanical actuators. The speed of this rotation places a time constraint on the minimum exposure time possible. In addition to this switching time, there was a further delay associated with the refresh rate of the SLM. Together, this means there was a period of time between when the image sent to the SLM was changed and when the camera exposure could start. Figure 7.7 shows an example of the images acquired when too little time was given for the pattern to refresh. Given that the camera was triggered after the new pattern was sent to the SLM, and that camera exposure was below the estimated refresh time, this error is a result of delayed pattern projection and not a mistimed camera triggering.

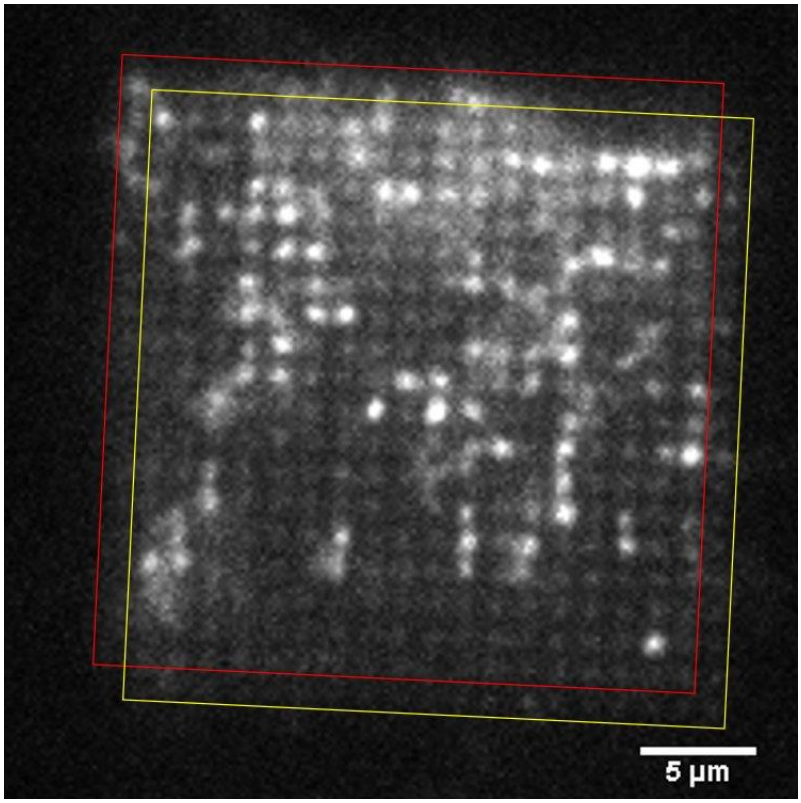

Figure 7.7: Example of pattern refresh error.

Red square shows the area of the previous pattern used; a square grid with doughnut PSFs. Yellow square shows the region of the desired pattern with spot PSFs. As a result of screen refresh rate and LC switching time, only half of the pixels have updated before camera exposure was started.

To measure the refresh time, a time delay was added between the pattern being sent to the SLM and the camera exposure being triggered. This delay was increased until the pattern error shown in figure 7.7 was no longer seen, giving an SLM refresh time of > 75 *ms*. This refresh time placed a limit on the speed of image acquisition, limiting temporal resolution. While live-cell imaging was achieved, the mitochondrial network is a relatively slow-moving structure and, assuming the cell does not undergo significant photodamage, does not significantly change shape over the course of one frame acquisition. It is, however, likely that imaging more dynamic processes would be difficult with these currently extended exposure times.

7.5 eMSIM imaging

After the successful demonstration of MSIM with holographic projection, eMSIM was tested on micro-beads, fixed cells and live cells using green and blue laser excitation. For these tests, $l = 1$ doughnut excitation spots were used for the doughnut patterns. After analysis of the MSIM imaging results, a pattern refresh delay of 100 *ms* was introduced between the pattern shifts and the start of image acquisition. 16:1 spot separation was used, requiring a total of 512 pattern shifts for each eMSIM image.

7.5.1 micro-bead imaging

Figure 7.8 shows the results of micro-bead imaging and figure 7.9 show the intensity profile across the image of two neighbouring beads. For eMSIM imaging, a FED subtraction factor of 0.5 was used. 5 PIFP and 30 JRL iterations were used for reconstruction. These beads were imaged with 532 *nm* excitation. In the images of the full field of view, the contrast improvement in the image is noticeable as a reduction in the background intensity compared to the diffraction-limited image. This is also apparent – although to a lesser extent – in the MSIM image.

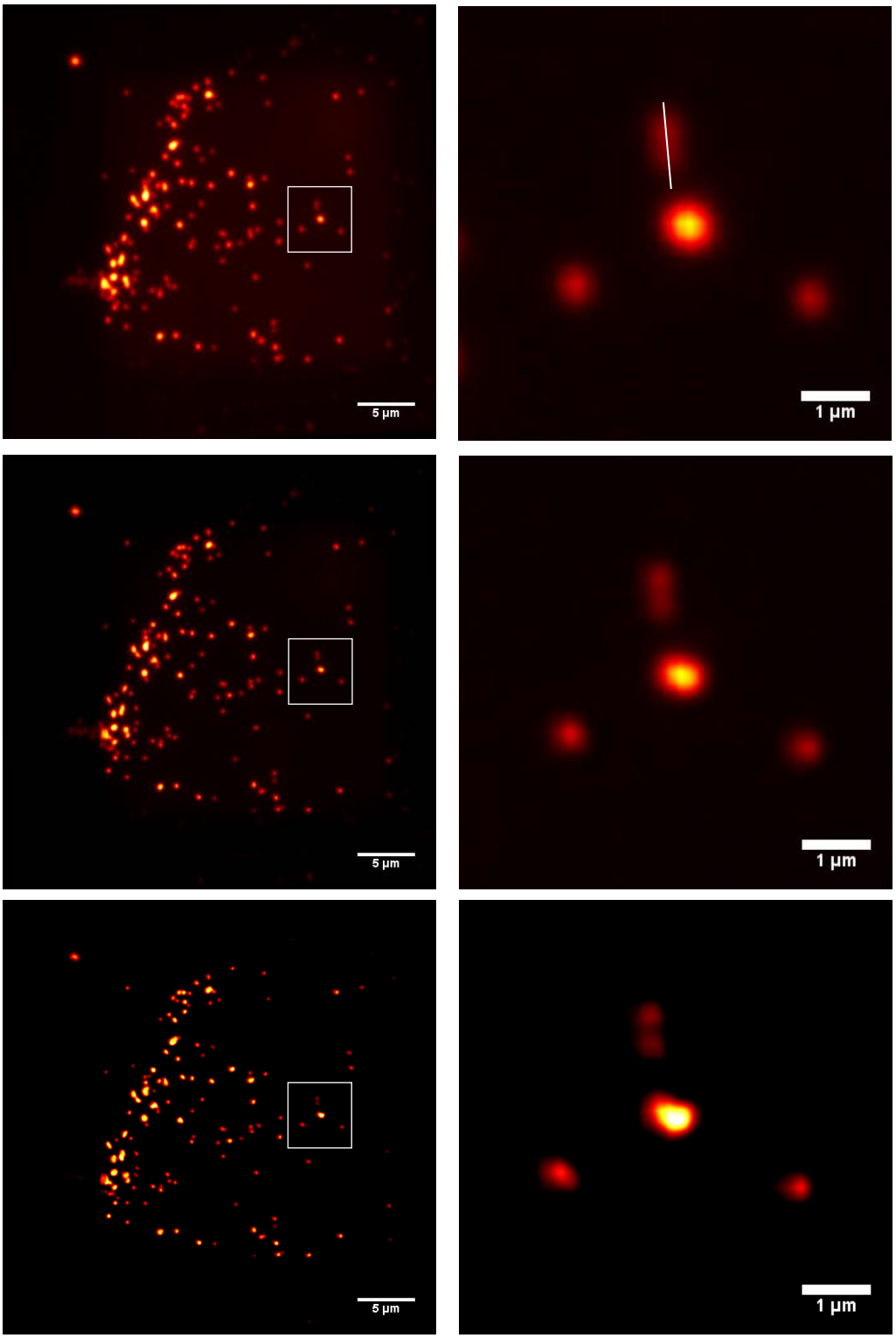

Figure 7.8: Comparison of microbead imaging techniques.

Top: Diffraction-limited imaging. Middle: MSIM imaging. Bottom: eMSIM imaging. Left panes show full field of view, right panes show magnified region indicated by white square. Beads were excited with 532 *nm* laser excitation and emission was collected after a 550 *nm* long-pass filter. Reconstruction was performed using 6 JRL iterations and 25 PIFP iterations.

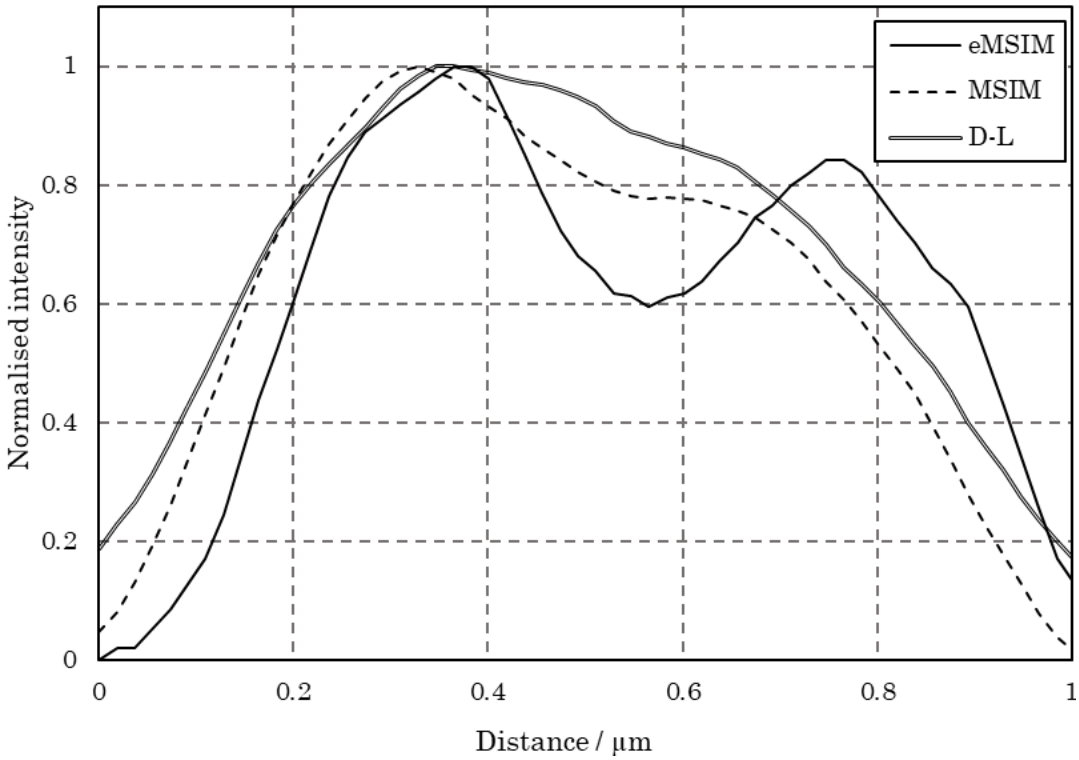

Figure 7.9: Intensity profile across two beads in eMSIM imaging.

Solid line: eMSIM imaging. Dashed line: MSIM imaging. Double line: Diffraction-limited imaging. Comparing the three intensity profiles, at this separation of beads only the eMSIM imaging has been able to resolve the individual beads.

7.5.2 Fixed cell imaging

The results of fixed-cell imaging are shown in figure 7.10. For fixed cell imaging, a FED subtraction factor of 0.5 was used. Image reconstruction was performed with 30 PIFP and 10 JRL iterations. Figure 7.11 shows the intensity along the line path indicated in figure 7.10. In contrast to the micro-bead imaging, eMSIM showed no significant improvement in resolution over MSIM imaging. This is demonstrated in the line intensity plot where no new features have been resolved but the difference in intensity across some of the actin filaments has been increased.

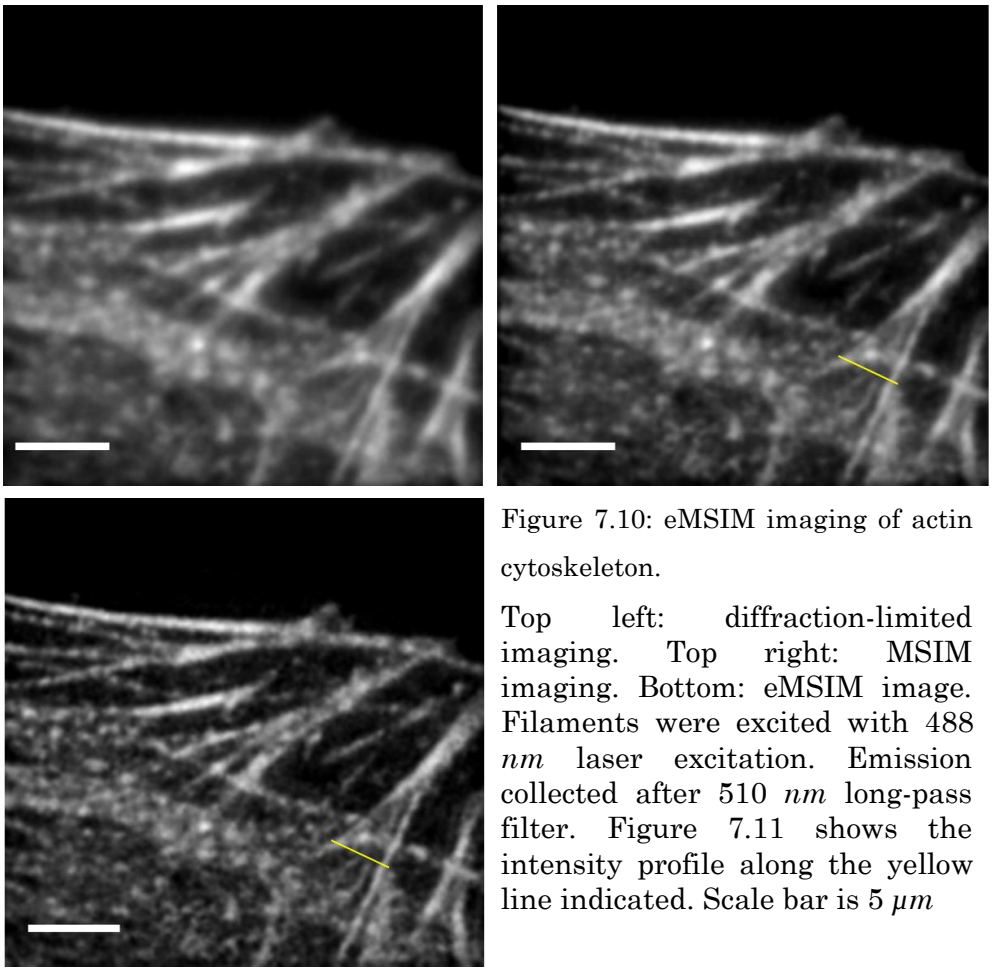

Figure 7.10: eMSIM imaging of actin cytoskeleton.

Top left: diffraction-limited imaging. Top right: MSIM imaging. Bottom: eMSIM image. Filaments were excited with 488 *nm* laser excitation. Emission collected after 510 *nm* long-pass filter. Figure 7.11 shows the intensity profile along the yellow line indicated. Scale bar is 5 μm

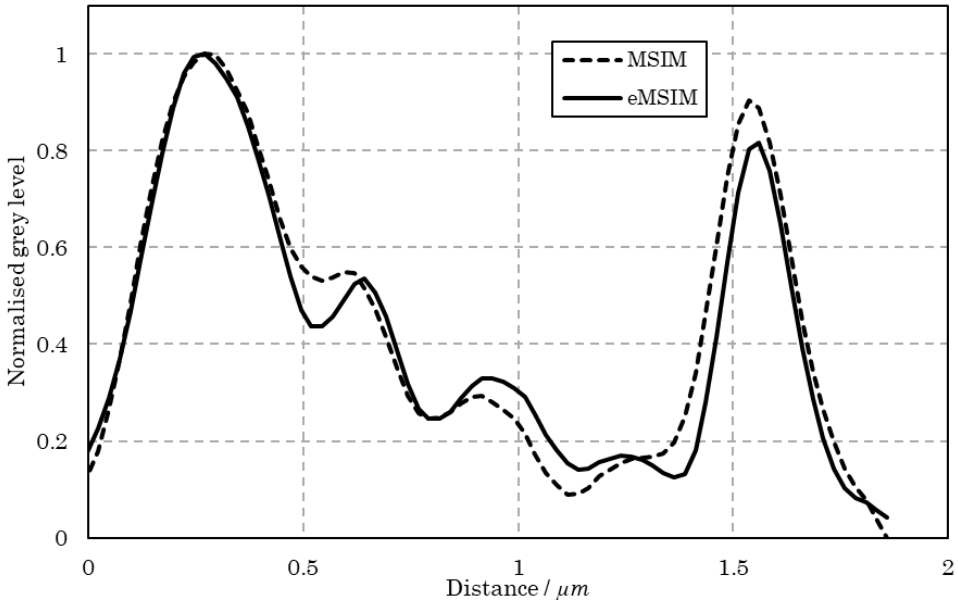

Figure 7.11: Intensity profile across actin filaments.

Solid line: eMSIM imaging. Dashed line: MSIM imaging. Although the peaks are far more distinct in the eMSIM reconstruction, the improvement in resolution over the MSIM image is minimal and neither fulfil the Raleigh criterion.

7.5.3 Live-cell imaging

The final targets used were live cells stained with MTG. Throughout mitochondrial imaging a FED subtraction factor of 0.5 was used. 30 PIFP and 30 JRL iterations were used for image reconstruction. Figures 7.12 and 7.13 show the results of mitochondrial imaging in the peri-nuclear region of the cell. The magnified regions in figure 7.13 show how this improvement in contrast has led to an increase in resolution as finer structures of the mitochondria are visible in the eMSIM reconstruction.

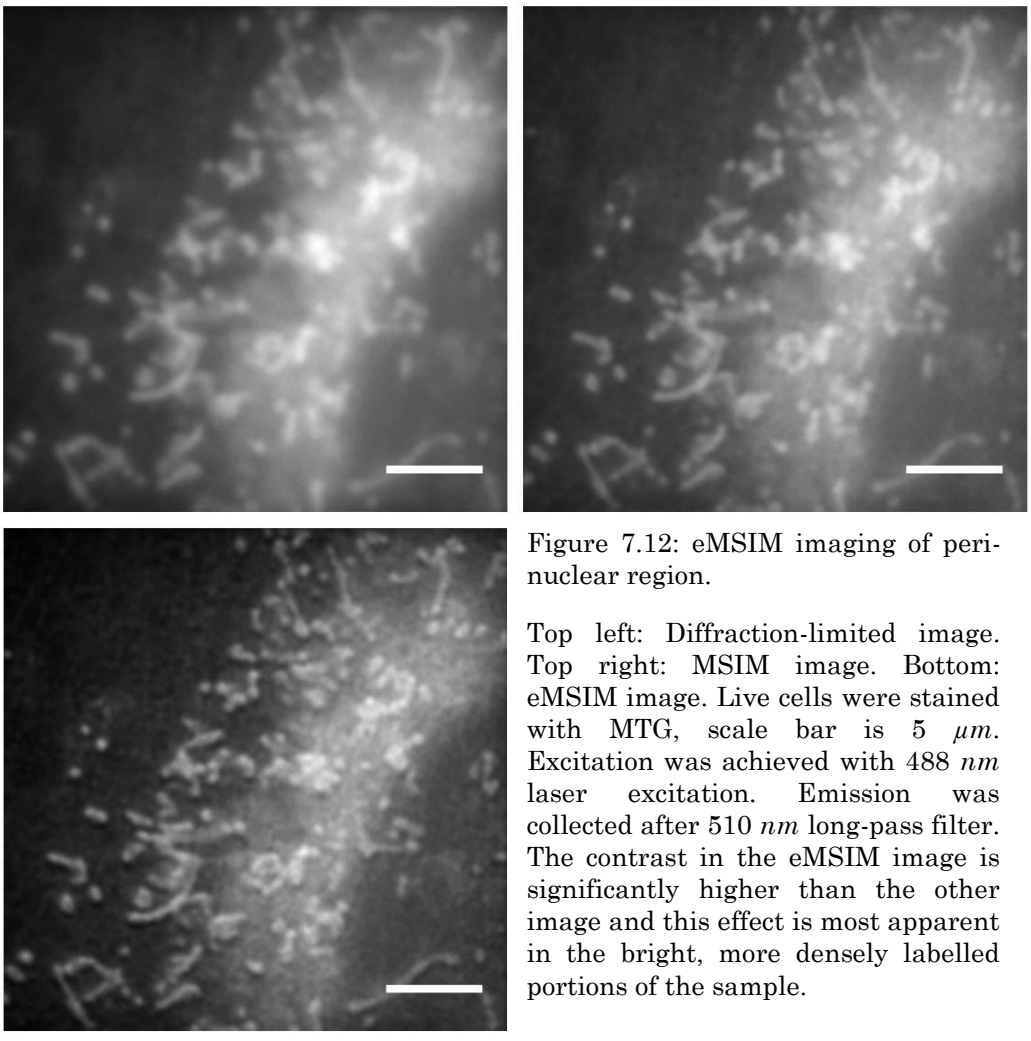

Figure 7.12: eMSIM imaging of peri-nuclear region.

Top left: Diffraction-limited image. Top right: MSIM image. Bottom: eMSIM image. Live cells were stained with MTG, scale bar is 5 μm. Excitation was achieved with 488 nm laser excitation. Emission was collected after 510 nm long-pass filter. The contrast in the eMSIM image is significantly higher than the other image and this effect is most apparent in the bright, more densely labelled portions of the sample.

Imaging the mitochondrial network also offers a way to determine the phototoxicity of the technique. The distribution of the mitochondrial network, as well as mitochondiral fission/fusion events, is highly sensitive to changes in the intracellular environment. In particular, mitochondiral

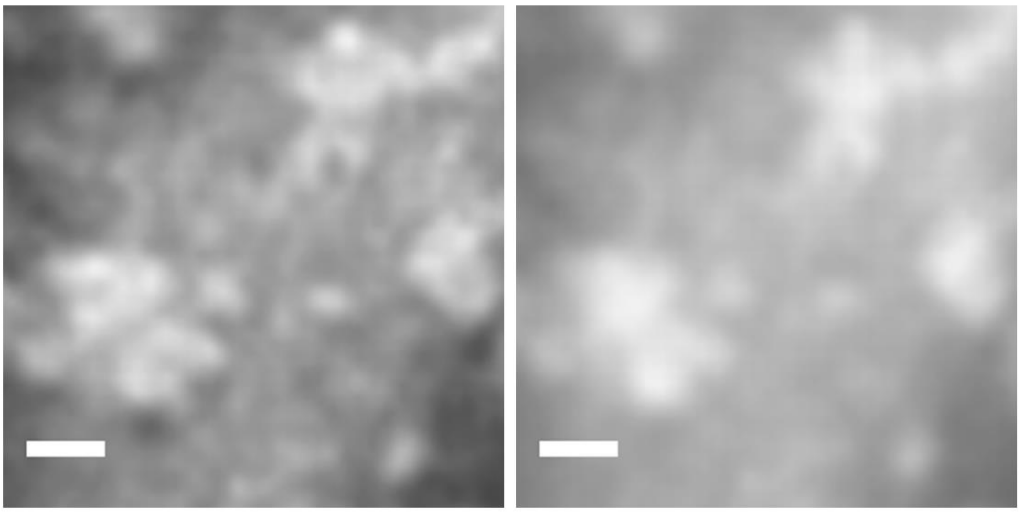

Figure 7.13: Magnified region of figure 7.12.

Left: eMSIM image. Right: MSIM image. Live cells were stained with MTG, scale bar is 1 μm. The resolution improvement is apparent as only the eMSIM image has resolved the finer details of the mitochondria. As an example, in the eMSIM image the

redistribution is rapidly affected by oxidative stress, one of the main causes of phototoxicity. As such, extending imaging of the mitochondrial network allows for a basic assessment of the phototoxicity of a technique. In eMSIM imaging, such redistribution of the network would be visible in the reconstructions as significant subtraction aretfacts. Since high numbers of such artefacts are not seen in figures 7.12 and 7.13, it is possible to say that the mitochondrial network was not undergoing a complete and rapid redistribution. As such, the relatively static nature of mitochondrial network suggests that eMSIM did not cause significant photo-toxicity at the exposures used.

In some reconstructions, however, the live-cell imaging also highlighted the limitations of the eMSIM method. Figure 7.14 shows a series of images acquired of a sample that shifted during imaging. The shift in this sample has been caused by either rearrangement of the mitochondria or, more likely, movement of the entire sample, possibly from sample drift. The black regions indicated are the result of areas of negative intensity in the FED image used as the initial estimate. Although some negative regions are inevitable in individual frames, with low subtraction factors these negative regions should be small, local artefacts which are removed when the final FED image is calculated. These larger black regions however

indicate that there are large areas of high fluorescence intensity, not present in the spot illumination but which have drifted into the same region before doughnut illumination. As all of these artefacts are located on the upper side of the mitochondria, and there is a fringing around the nucleus, it is likely that this movement was the entire sample shifting upwards rather than individual mitochondria redistributing.

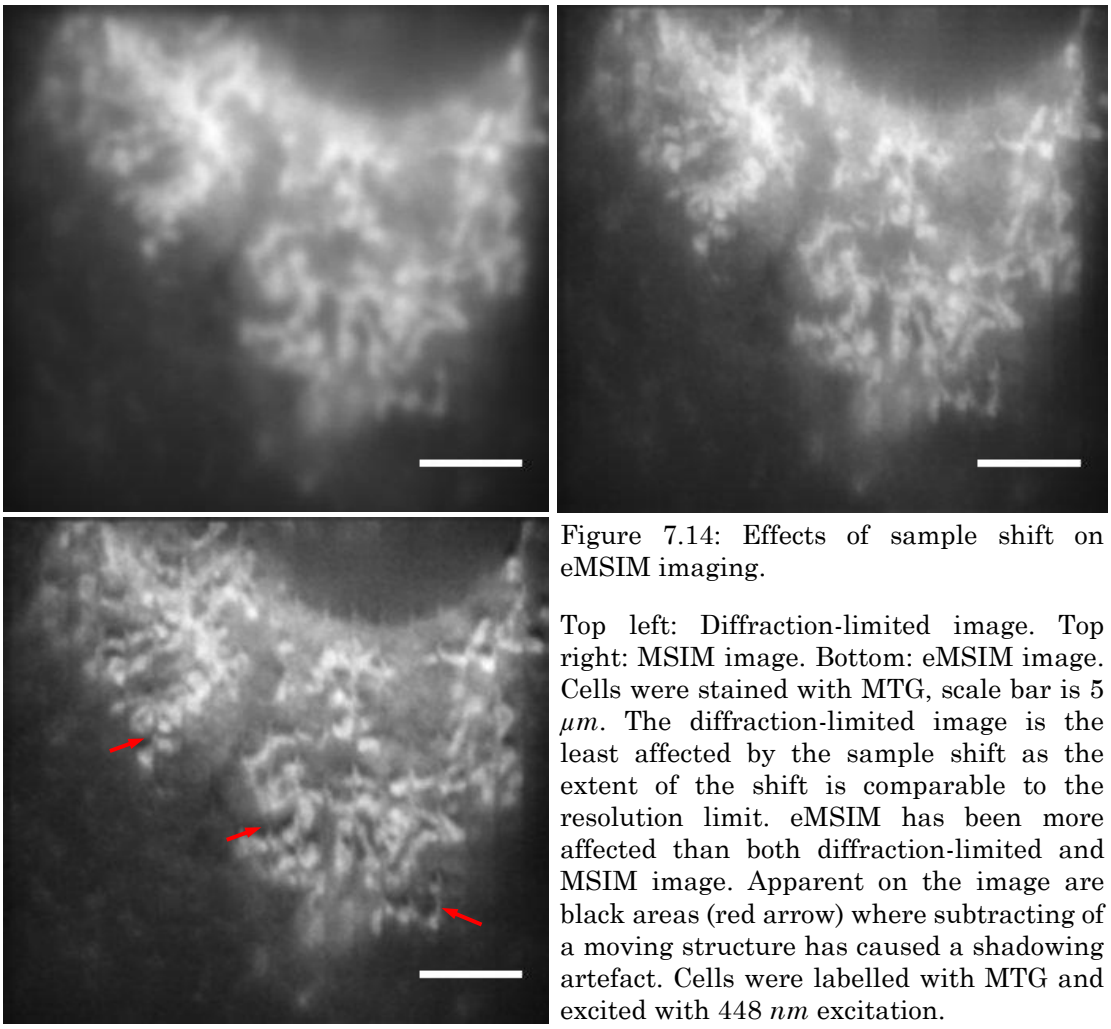

Figure 7.14: Effects of sample shift on eMSIM imaging.

Top left: Diffraction-limited image. Top right: MSIM image. Bottom: eMSIM image. Cells were stained with MTG, scale bar is 5 μm. The diffraction-limited image is the least affected by the sample shift as the extent of the shift is comparable to the resolution limit. eMSIM has been more affected than both diffraction-limited and MSIM image. Apparent on the image are black areas (red arrow) where subtracting of a moving structure has caused a shadowing artefact. Cells were labelled with MTG and excited with 448 nm excitation.

7.6 Analysis of eMSIM imaging

Overall, the quality of the results obtained through eMSIM imaging was mixed, highlighting both the improvements and further limitations over MSIM imaging. The micro-bead images indicate that there is a true resolution increase gain in eMSIM over MSIM imaging. However, this

analysis is limited to resolving only smaller point sources and does not on its own suggest an improvement over MSIM in general biological imaging. Additionally, it was not possible to acquire two images of the same FOV meaning FRC measurements could not be used to quantify the increase in resolution. Unlike the micro-bead imaging, the results of imaging the actin filaments showed no significant increase in resolution over MSIM. This may reflect how the resolution increase achieved over MSIM is limited and can only be seen in very specific targets. Measurements of the intensity profiles of filaments, however, does show that eMSIM increases the contrast of structures already resolved by MSIM. While this may offer no extra information, it does allow for the existing information to be better visualised above more random fluctuations in sample intensity. The advantage of the contrast improvement is visible in figures 7.12 and 7.13 where it has allowed for finer structures of the mitochondrial network to be visualised.

The exact origin of the contrast improvement is difficult to determine but is likely to be a result of two separate effects. The first possible explanation is an artefact of the subtraction used to generate the FED image for the initial estimate of the sample structure. During the subtraction process, negative values are inherently created in the subtracted image. Since such values have no physical meaning, in the FED image these are simply set to zero. In the FED image therefore, the varying range of negative values have all been set to the same zero value, reducing the total range of values, equivalent to increasing the contrast and decreasing the brightness.

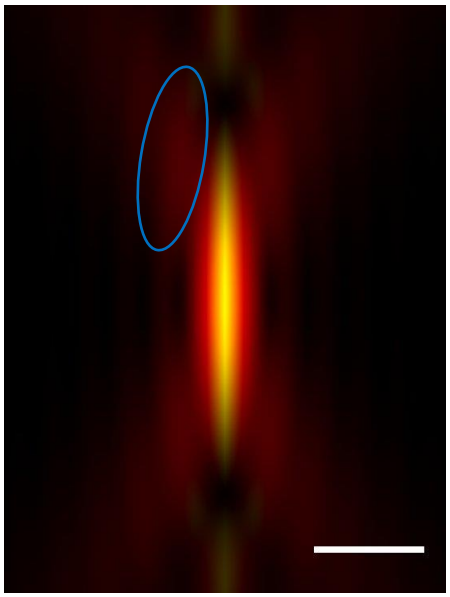

Figure 7.15: Comparison of axial MSIM and eMSIM PSFs.

Gaussian excitation PSF used in MSIM shown in red. Yellow shows the effective eMSIM PSF. PSFs calculated for a wavelength of 488 nm, objective NA = 1.2 and subtraction factor of 0.5. Scale bar is 500 nm. Subtracting the doughnut PSF not only reduces the width of the central maxima, but also removes the outer lobes of the PSF above and below the focal plane (blue circle).

The second – and potentially more interesting – explanation relates to the axial structure of the excitation PSFs used. The theoretical calculations of the PSFs show the doughnut PSF is axially more extended than the Gaussian PSF, i.e. the intensity of the beam keeps a narrower but more intense profile above and below the focal plane. This means that, not only does the subtraction increase lateral resolution, it also, though to a lesser extent, increases the effective the axial resolution by subtracting fluorescence emission from out-of-focus fluorophores close to the central axis. This is shown in figure 7.15 where the merged image shows a comparison of the axial profiles of the un-modified diffraction-limited PSF and effective eMSIM excitation PSF. In eMSIM excitation, this means there is reduced fluorescence from above and below the focal planes, reducing out-of-focus blur in the final image. This effect can be seen in figures 7.16 and 7.17 where there is significant out-of-focus light due to the high density of mitochondria above and below the focal plane.

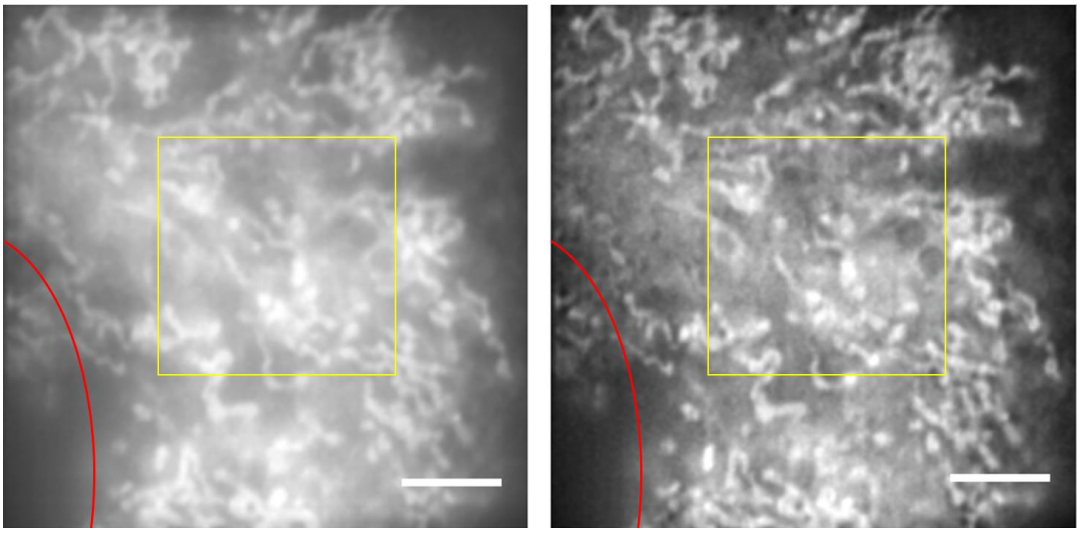

Figure 7.16: eMSIM imaging of peri-nuclear mitochondria.

Left: MSIM image. Right: eMSIM image. The red line indicates border of the cell nucleus and the yellow square denotes the areas magnified in figure 7.18. Scale bar is 5 μm. Cells were excited with 488 nm laser excitation. Emission was collected after a 510 nm long-pass filter Immediately apparent in the image is the increase in contrast over the MSIM image allowing finer structures of the network to be more clearly visualised.

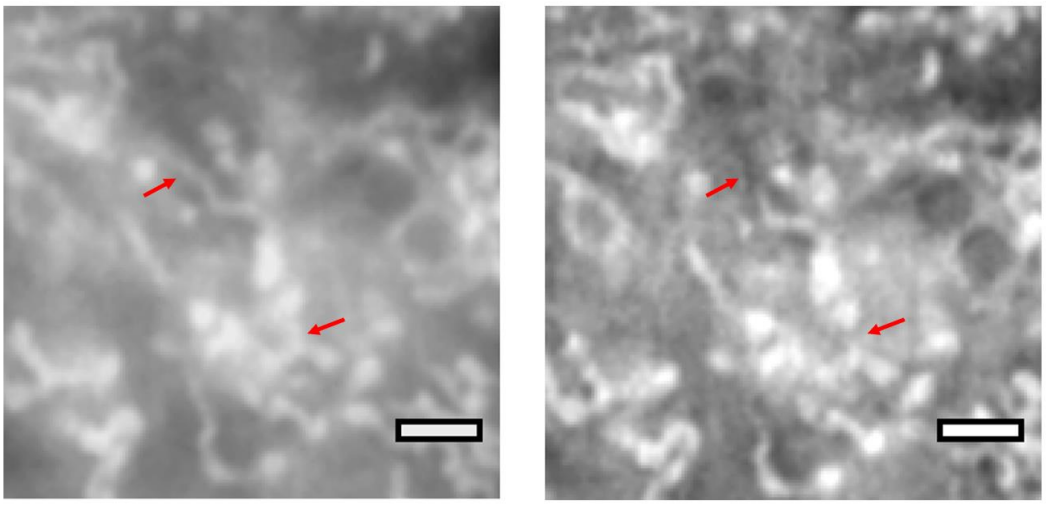

Figure 7.17: Magnified region of figure 7.17.

Left: MSIM image. Right: eMSIM image. Scale bar is 2 μm. The red arrow indicates portions of mitochondria that are no longer apparent in the eMSIM image. This suggests that the eMSIM imaging has removed light from outside the focal plane.

In addition, features of the MSIM image have been removed from the eMSIM image. Since these features that have been removed appear as the same intensity as other features that have not been removed, this suggests that they have been removed from eMSIM image, not by an increase in

contrast, but because they did not lie in the same focal plane. This is distinct from the effect seen where there are large black regions in the image as a result of sample movement.

The value of this improved performance in high-background imaging is apparent when comparing different imaging techniques. Figures 7.18 and 7.19 show a comparison of imaging techniques on similar targets. All images were acquired of mitochondria in live-cells stained with MTG under 488 *nm* excitation. LSCM images were acquired with a 60x 1.4NA objective lens. Striped-pattern SIM images were acquired using a 60x 1.45NA objective lens.

Of all the techniques, the confocal imaging has removed the most out-of-focus light and has the best background noise rejection. The grainy appearance is common in confocal imaging and results from the low light levels gathered from the sample. Even though eMSIM has improved resolution over MSIM, the striped pattern SIM image has the highest apparent resolution with the sharpest edges. While this is in part due to the higher NA of the imaging objective, this effect is greater than would be expected from simply the higher NA. This extra increase in resolution has

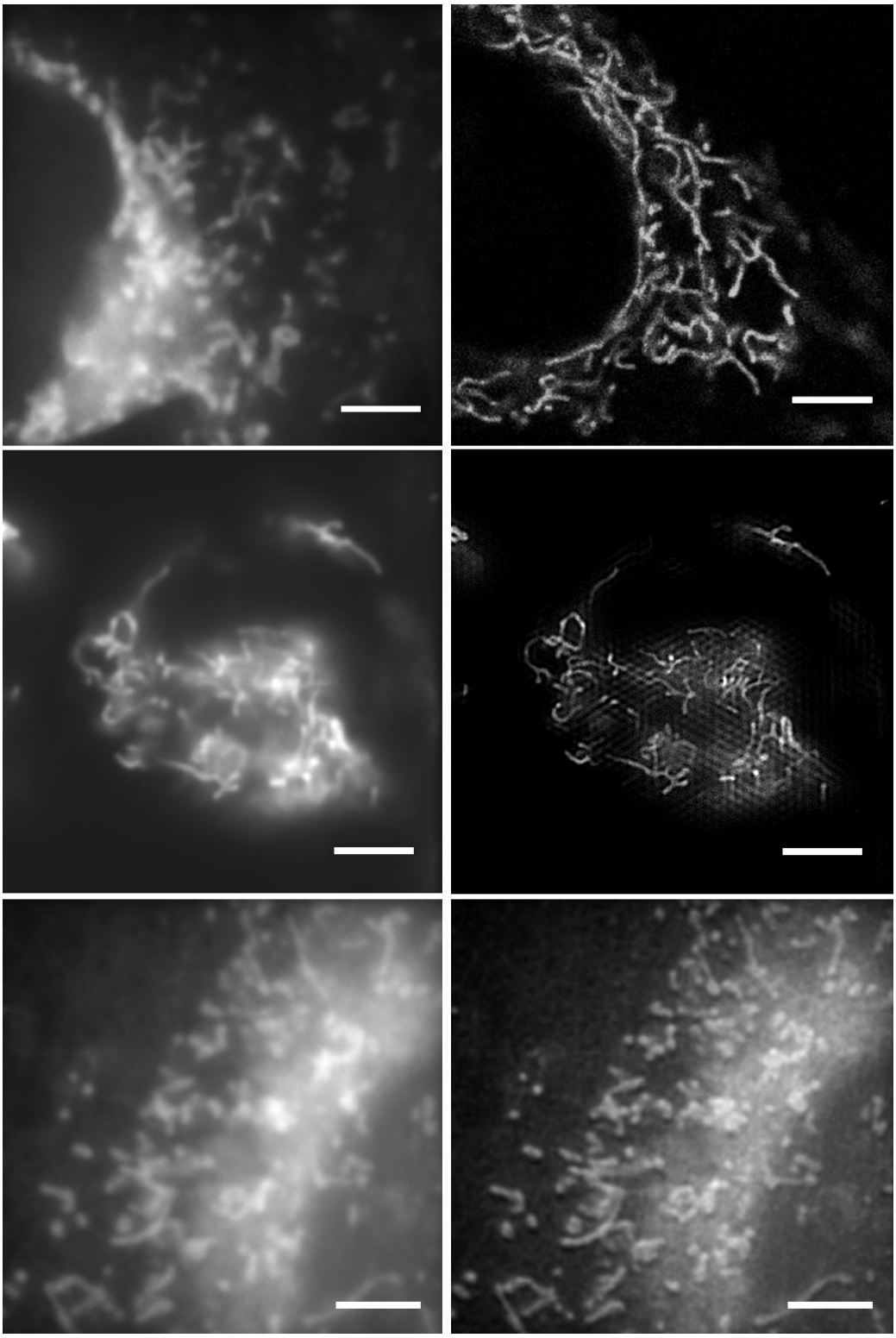

Figure 7.18: Comparison of sectioning imaging techniques.

Top Left: widefield image. Top right: confocal image. Middle left: widefield image for striped pattern reconstruction. Middle right: striped pattern reconstruction. Bottom left: widefield image for eMSIM reconstruction. Bottom right: eMSIM reconstruction. All images were acquired of mitochondria labelled with MTG under 488 nm excitation. Scale bars are 5 μm. eMSIM and striped-pattern fluorescence collected after 510 nm long-pass filter. Confocal emission collected between 500 nm and 550 nm. Confocal image courtesy of Robert Pal. Striped-pattern SIM image courtesy of Katharina Scherer.

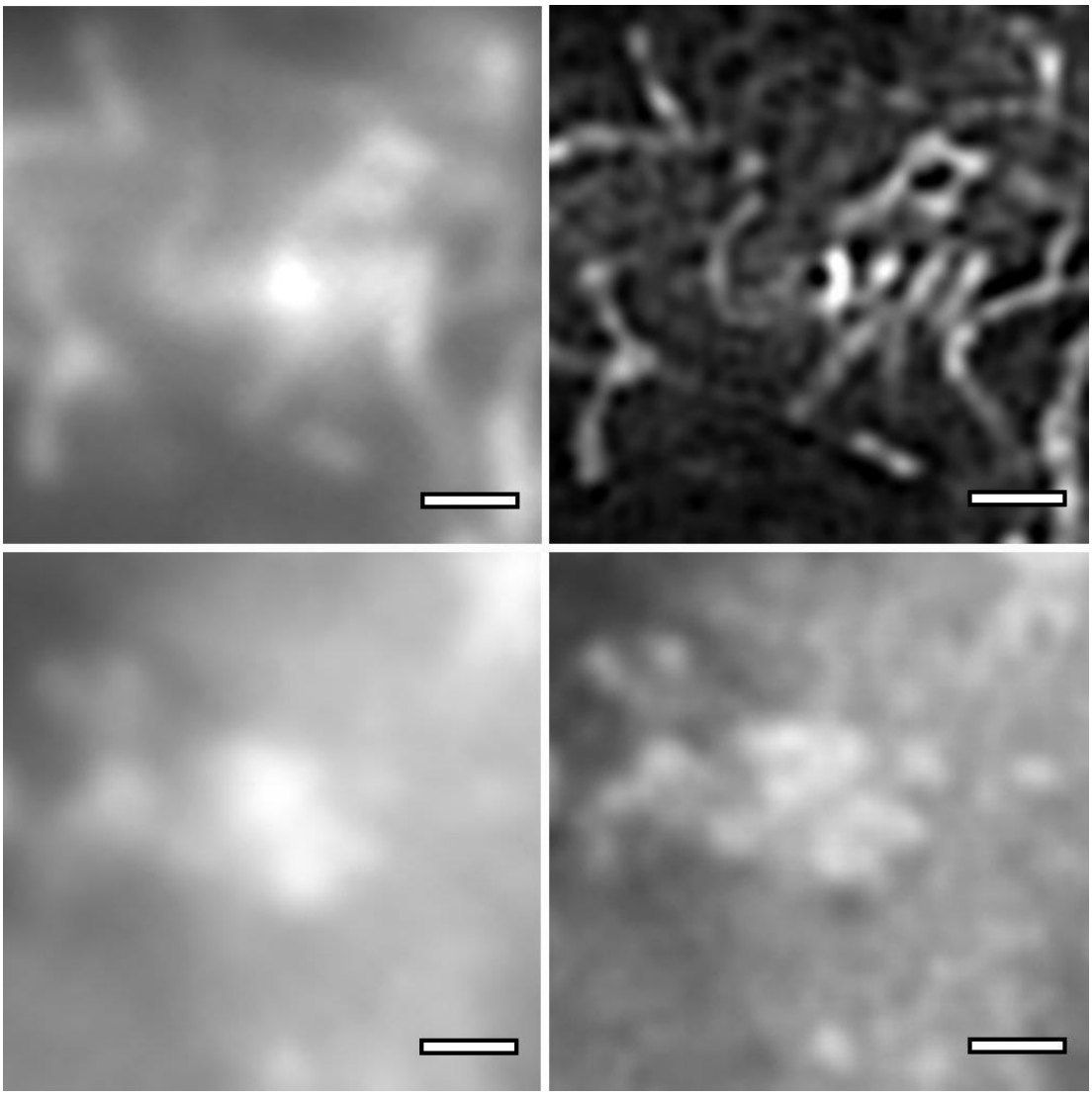

Figure 7.19: Magnified comparison of imaging techniques.

Magnified regions of figure 7.18. Top Left: widefield image for striped pattern reconstruction. Top right: striped pattern reconstruction. Bottom left: widefield image for eMSIM reconstruction. Bottom right: eMSIM reconstruction. Scale bars are 1 μm.

come from the reconstruction method used. For correct comparison with existing SIM imaging, the striped pattern SIM image was deconvolved directly in frequency space – as described in Chapter 2 – as this is almost exclusively used in striped-pattern reconstruction. Fourier-space reconstruction has led to the apparent increased resolution improvement by starting with the assumption that all spatial frequencies that are theoretically recoverable have been collected. Spatial frequencies have then been shifted and amplified in frequency space without consideration of whether they reflect the true structure of the sample. However, looking at the magnified images (figure 7.19) this has introduced significant

reconstruction artefacts. Amplification of spatial frequencies that do not originate from the true structure of the sample has resulted in a 'ringing' of where edges are over-amplified, and structures likely not present in the sample have been introduced. This has drastically reduced reconstruction performance as – although the image may appear to be a higher resolution – it is difficult to determine which structures are real making any interpretation of the information meaningless. One of the main causes for this is that out-of-focus blur has not been accounted for in the intrinsically 2D Fourier space reconstruction method. This contrasts with the eMSIM reconstruction where resolution increase is still apparent, but no artefacts are present. Comparing the widefield images on the left side of the pane, the eMSIM has retained this artefact-free reconstruction despite the background signal being higher than in the striped-pattern SIM. This reflects the difference in the reconstruction approach as for MLD there has been no assumption that all theoretical spatial frequencies have been collected.

7.7 Summary

This chapter has described the key findings results of the imaging studies conducted in the project. In the first half of the chapter, the efficacy of holographic projection for generating MSIM patterns is demonstrated. In addition, the successful reconstruction of these super-resolution images confirms that the pattern estimation and reconstruction algorithms created are also valid.

In the second half of the chapter, eMSIM imaging is performed and compared to MSIM and striped-pattern SIM. In comparison to MSIM, microbeads demonstrate a clear improvement in resolution. However, imaging of the actin cytoskeleton and mitochondrial network highlight the limitations of eMSIM imaging. In the cytoskeleton imaging, there is no clear increase in the resolution of the images, although an increase in contrast is visible. The imaging of the mitochondrial network demonstrates

that the low illumination intensities have not significantly affected the mitochondrial network, suggesting minimal phototoxicity. Finally, imaging the mitochondrial network has shown how the technique is capable of live-cell imaging albeit with a low temporal resolution.

8. Conclusion

Summary: *this chapter contains the conclusions drawn from the work conducted in this project. It will describe to what extent the goals of the project were achieved through comparison with existing imaging methods Finally, it will suggest future directions of the technique and areas of ongoing work.*

8.1 Introduction

Super-resolution microscopy has become an important and valuable tool in the study of biological systems. In the previous chapters the development of novel techniques in super-resolution microscopy has been described. It is important, however, to put these developments in the context of the wider field. To this end, the first part of this chapter compares existing pattern projection and super-resolution methods to those described in previous chapters. In its current form, eMSIM is a technique in development and has great potential for future improvement. The second portion of this chapter details some of these potential improvements.

8.2 Comparison to existing techniques

8.2.1 Pattern projection

As detailed, holographic projection of multi-spot patterns has a number of advantages over existing amplitude-only projection methods. The importance of aberration correction in pattern projection is apparent in figure 4.11 but the further advantages arising from the uniformity of pattern projection are also apparent. In the current holographic projection system, the excitation pattern is confined to a modest portion of the total FOV as it must be shifted away from the bright focal spot resulting from

un-diffracted light passing through the SLM. This meant that imaging was only performed in one corner of the possible FOV. One future improvement in the system would be to incorporate a more sophisticated beam block in the excitation optics that blocked this small focal spot while allowing imaging around the spot. Although this would leave a small portion of the image blank, it would allow for a greatly extended FOV. However, even though this was not done on the existing system, when accounting for differences in magnification, the imaged FOV was still comparable to or larger than existing MSIM setups using amplitude-only SLMs. Although previous studies have reported amplitude-only projection for imaging wider FOVs, in these implementations, significant aberrations and non-uniformity of pattern projection are particularly apparent towards the edges of the images, preventing meaningful imaging outside of the central region of the FOV.

8.2.1 eMSIM imaging

The theoretical tests of eMSIM imaging demonstrated the potential resolution improvement possible over conventional MSIM imaging. This was demonstrated on a variety of structures and was particularly apparent on the simulated point-sources. However, real-world testing of the technique demonstrated that this increased resolution was limited. In comparison to MSIM, explicit resolution increase was only measurable on the micro-bead images. Aside from resolution improvement, eMSIM also appeared to show an increased contrast and depth sectioning capability when compared to MSIM. While this made minimal different to the more sparsely labelled actin cytoskeleton, in the imaging of densely labelled mitochondria, this contrast improvement did allow additional features to be distinguished. In comparison to the more popular striped-pattern SIM, eMSIM showed a reduced resolution improvement although with fewer resolution artefacts in regions of high background fluorescence. For a biologist, whether this trade-off in resolution is worthwhile would depend

heavily on the specimen being observed and the nature of the experiment. For example, when imaging structures close to the coverslip, it is likely that TIRF-SIM using striped patterns would be preferable. However, MSIM is already a popular choice for improving resolution deeper into tissues and, in these situations, it is quite possible that eMSIM might offer a resolution improvement that is worth sacrificing temporal resolution. It is also likely that developments in the field of eMSIM might make this technique even more attractive to biologists and future developments are suggested in the next section.

8.3 Future directions in MSIM and eMSIM

Despite the developments demonstrated in this project, the fields of holographic pattern projection and eMSIM imaging still have great potential for future improvements.

In MSIM with holographic projection one of the key limitations identified was the relatively low temporal resolution. Factoring in exposure time and LC switching time meant total time for each frame was ~100 *ms*. For the 16:1 separation this gave total acquisition times of ~25 *s* for each image. This limited the live-cell capabilities to slow-moving cellular structures as well as limiting the ability to perform z-stacking. If the technique is to be applied to faster moving structures, for example filament assembly or particle tracking, significant improvement in imaging time will be required. While the transmission SLM used was a cost-effective method for phase manipulation, the newer LC SLMs available have significantly reduced switching times, which would greatly improve temporal resolution. The use of improved SLMs would likely also increase performance by offering better phase change characteristics. The transmission SLMs, although partly as a result of the driver circuitry, only offered a 1.75 pi phase change, below that required for optimal holographic projection. A better phase change on the incident beam would result in an improved pattern uniformity and more robust PSF engineering.

Another simpler method to increase temporal resolution would be to choose the hologram spot separation in a more dynamic way. For the imaging conducted, a spot separation of 16:1 was used to reduce excitation spot cross-talk. In reality, this separation was excessive for both the micro-beads and actin filament targets, and likely represents a worst-case scenario for densely labelled samples such as the mitochondria. For more sparsely labelled samples, such as the fluorescent beads or filament networks, a reduced separation could be used. As the number of frames requires scales with the square of the spot separation, reducing the 16:1 ration by only a small amount would result in greatly improved imaging times.

A final method to improve the temporal resolution would be to use a more sophisticated method to send the hologram to the SLM. For example, application extensions written with the OpenGL shader language have demonstrated very significant improvements in SLM refresh by synchronising the hologram display to the refreshing of the SLM.[114] Using this would lower the delay time needed between updating the SLM and triggering the camera.

The effect of these improvements can be approximated through comparison with existing systems. The latest LC SLMs capable of the necessary phase changes typically have refresh times of 10 *ms* for the wavelengths used. With correct synchronisation with SLM control using the OpenGL shaper, SLM update can be achieved every 16 *ms* making this the time-limiting step. With the current exposure times used, and a slightly reduced spot separation (12:1), this means that acquisition time for a single reconstruction could be reduced to ~7 *s,* down from the current ~50 *s*. This is comparable to confocal imaging times on small FOVs and would be faster than confocal imaging over the wider FOVs possible with holographic projection. While 7 *s* is not as fast as striped-pattern SIM, this increased imaging time is a worthwhile sacrifice when imaging deeper into denser tissues where striped-pattern reconstruction would fail.

Another area for improvement in the MSIM/eMSIM technique is the reconstruction process. While MLD offers advantages over direct reconstruction, choosing the reconstruction parameters (i.e. iteration number) is largely qualitative and varies between samples. One promising innovation in biological imaging has been the application of machine learning to image processing. Based on 'neural networks' (figure 8.1), machine learning is a conceptually simple process, but one which can offer remarkable results in image processing. To apply machine learning to image processing, the neural network is trained on a very large database of input data and ideal (or ground-truth) results. This training involves optimising the weighting factors (black lines on figure 8.1) of each neuron until the output result of the neural network closely matches the ground truth. Due to the very high number of connections between neurons, training the network is incredibly computationally demanding even on the most powerful computers and GPUs available.

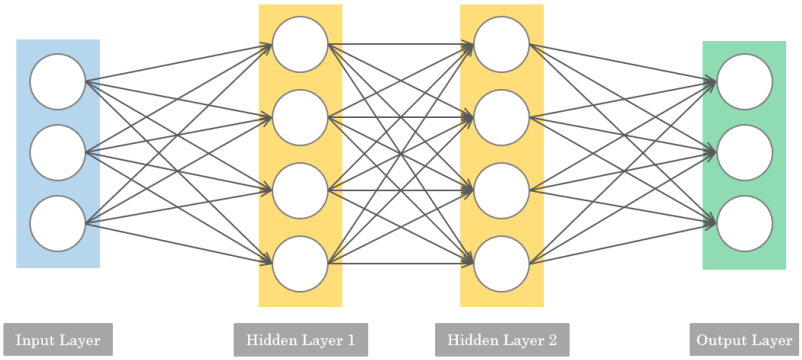

Figure 8.1: Simplified diagram of neural network architecture.

The values of the pixels of the input image are fed forward into a new hidden layer consisting of a set of neurons. The values of the pixels are multiplied by a different weighting factor along each line and then summed to give a value at the next neuron. This process is repeated through several more hidden layers until the values of the output pixels are calculated at the final output layer. Neural networks are trained by refining the weighting factors for each line in the process.

However, once trained, the neural network can output results incredibly quickly, orders of magnitude faster than comparable image processing techniques. So far in optical microscopy, machine learning has been

successfully applied to the de-noising/interpolating of images, as well as the processing of SMLM data-sets.[115] Only very recently has machine learning been applied to post-processing in SIM[116] although not yet to the pattern estimation or deconvolution of SIM/MSIM images. While the techniques developed here for image processing are faster than any previously reported, it is likely that the correct application of machine learning to raw SIM/MSIM data with allow for more versatile and accurate image deconvolution and this is an area of ongoing research.

Another limitation of the projection technique was the method used to determine the aberration correction coefficients. For this work, the aberration correction coefficients were determined qualitatively by analysis of patterns projected onto monolayers. A more sophisticated method would be to automate the process, analysing either images of the monolayer or images of the sample. As with pattern estimation, each of these techniques has its merits. Using a monolayer to determine aberrations would be a very effective method of compensating for aberrations constant in the apparatus. For the current eMSIM system the largest aberration was a radially dependant astigmatism. As the main cause of astigmatism is the focussing off-axis illumination of a lens, the origin of this aberration is likely due to the excitation optics. In the relay system, low-cost 1" spherical convex lenses were used instead of the more common 2" bi-convex lenses. These cheaper lenses are more affected by astigmatism and it is most probably to source of the astigmatism observed. Given this, using a monolayer to estimate the aberrations coefficients was sufficient to correct for the most significant aberrations in the current system. However, if eMSIM is to be used primarily for the rapid imaging of deeper tissues, sample-specific aberrations would begin to detrimentally affect image quality. Correcting for aberrations in the sample however is more challenging, especially when using the DS approach to hologram calculation. To maintain *in vivo* imaging, it is important to rapidly adapted to changes in the sample meaning an iterative approach to estimation is

virtually impossible. A more sophisticated approach would need to be developed to determine the aberrations present in an image and to make full use of the aberration correction capabilities of the system such an approach would have to be capable of determining location-specific aberrations. The development and implementation of a method to perform this complex aberration correction would be incredibly useful to biologists and would represent a very significant improvement over existing systems. As with image reconstruction, machine learning has not yet been extensively studied for determining optical aberrations and it is likely that utilising machine learning in this field will offer new methods to solve these problems.

The final potential improvement to the eMSIM method is the extension to 3D super-resolution. As is seen in the results, there is already reduction in out-of-focus blur in eMSIM, potentially as a result of the 3D natures of the PSFs. In the high fluorescent density mitochondria samples this effect is especially apparent in the region surrounding the nucleus. However, this reduction in out-of-focus light is not, strictly speaking, a super-resolution technique as no new information about the sample is gathered. Indeed, using deconvolution approaches, it is possible to almost entirely remove this out-of-focus light (see Chapter 1). Using PSF engineering however, it is possible to achieve true axial super-resolution by artificially reducing the axial size of the PSF. In eMSIM this would be achieved by replacing the doughnut PSFs in the subtracted pattern with PSFs like those used in 3D STED[117] and 3D FED[118]. As discussed in Chapter 1, these PSFs have an axial structure resulting in a 3D central zero-intensity volume. When applied to eMSIM, this would mean that the initial FED estimate of the sample structure would be a 3D super-resolution image and that the raw data would also contain 3D super-resolution information. Given the 2D nature of the reconstruction algorithm though, it would not be possible to extract 3D SIM information from the image. However, since the raw data

would more closely approximate the ideal 2D imaging model, it is possible that lateral resolution would be further enhanced.

8.4 Final remarks

This project set-out to create a novel and cost-effective method for super-resolution imaging. Building on the SIM principle, it intended to offer further resolution increase in biological imaging without sacrificing the live-cell capabilities. To achieve this, a novel method for pattern projection in MSIM imaging was developed based on holography. This new method was designed to modular and has been tested and proved successful in achieving MSIM imaging. The ability to incorporate aberration correction directly into the pattern calculation, and to compensate for complicated and varying aberrations, makes the technique more versatile than existing methods. While the temporal resolution is limited by the relatively slow speed of the LC SLMs used, it is possible that, with the use of the latest generation of LC SLMs and more sophisticated programming, this issue may be addressed.

In addition to generating a new technique for pattern projection, throughout the course of this project new software has been developed for the rapid processing and simulation of MSIM data. Using the emerging field of GPU processing, the computational cost of pattern estimation and image deconvolution was reduced by an order of magnitude in comparison to existing techniques. This was achieved on a modest, and low-cost, commercial GPU, available to any microscopy lab. It is hoped that these new programs will become of use in biological imaging and image processing.

Finally, a new super-resolution technique, eMSIM, has been demonstrated, both theoretically and practically. In the current implementation, the advantages of eMSIM imaging over MSIM are minimal, especially when considering the extra acquisition time required.

However, the use of the holographic projection techniques developed to incorporate PSF engineering into the MSIM method offers the potential to explore a range of different, modified patterns for MSIM with ease.

Appendix

A.1 Work arising from holographic setup

As a technique to generate patterned light in a sample, holography is a very versatile technique with a number of potential uses outside of optical trapping and SIM. One such use that is currently being explored is the use of patterned light to cure a UV sensitive resin at diffraction-limited resolutions. Cell proliferation and differentiation is a highly sensitive process which can be greatly influenced by the mechanical properties of the growth environment. Currently developing high-resolution structures or surfaces on which to grow cells is a time-consuming and costly process. For biologists, this makes the process of studying how cells interact with their environment particularly challenging. With the increasing popularity of 3D printing, UV curing resins which polymerise to a solid under UV illumination have become both cheap and easily available. By using holography to generate diffraction-limited patterns of UV light, a sample of a UV curable resin can be selectively solidified in precisely controllable fashion. This allows for high-resolution structures to be printed onto the

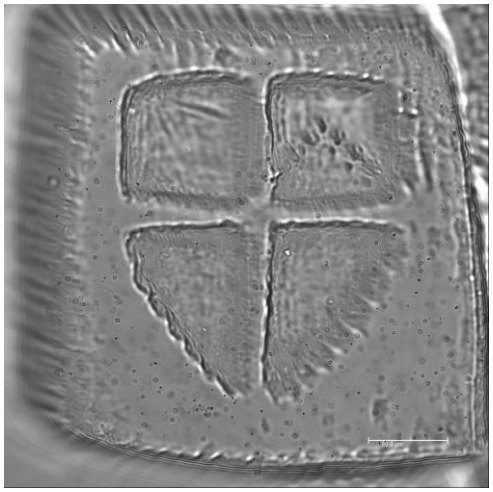

Figure A.1: Durham University crest printed with holography.

Brightfield transmission light image of 3D printed structure. This small structure was printed by selectively curing a thin film of resin spread on a coverslip. Scale bar is 20 μm.

surface of coverslips where the main cost of the process is the coverslip itself. This process was tested on the holographic setup constructed. The cytotoxicity of the printed structures cells was also tested by incubating mammalian fibroblast cells on samples of cured resin. Figure A.1 shows a brightfield image taken of one printed structure. In this early proof-of-concept test, a surface has been printed with structures below 2 μm on the surface. Further tests revealed that these printed structures were not toxic and cultured fibroblast cells were able to adhere to the surface. Current work based on this has involved printing structures for the alignment of bacterial cells. Specifically, imaging the ring complex inside the bacterial cells requires the bacteria to be positioned perpendicular to the coverslip. As the bacteria naturally lie on their side in culture, 3D printed structures are being developed to align the bacteria for imaging. This is shown in figure A.2.

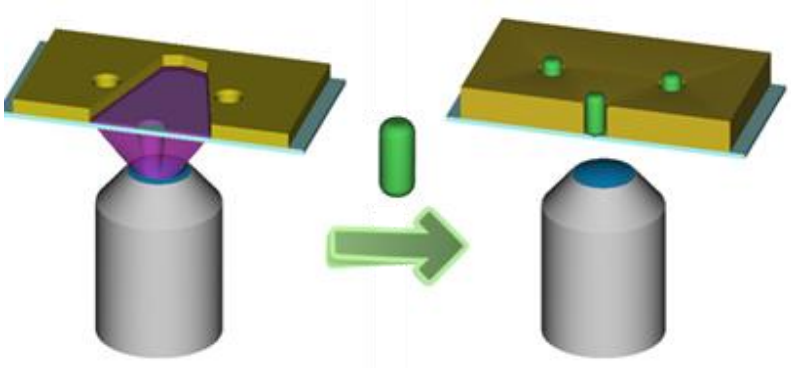

Figure A.2: Bacterial alignment in 3D printed structures.

Left: resin is cured on the surface of the coverslip by UV light. Right: After processing of the surface, bacterial cells grown on the coverslip align along the optical axis of the microscope in the printed pit structures.

A.2 Publications arising from this work

1. E. N. Ward and R. Pal. "Image scanning microscopy: an overview," J. Microsc. 266(2), 221–228 (2017).

2. E. N. Ward, F. H. Torkelsen, and R. Pal. "Enhancing multi-spot structured illumination microscopy with fluorescence difference," R. Soc. Open Sci. 5(3), 171336 (2018).

3. E. N. Ward and R. Pal. “Holographic projection for multi-spot structured illumination microscope,” J. Microsc. (2019) *Accepted manuscript*.

A.3 Other publications

1. 1. A.D. Lynes, C.S. Hawes, E.N. Ward, B. Haffner, M.E. Möbius, K. Byrne, W. Schmitt, R. Pal, T Gunnlaugsson. “Benzene-1,3,5-tricarboxamide n-alkyl ester and carboxylic acid derivatives: tuneable structural, morphological and thermal properties.” CrystEngComm 19, 1427–1438. (2017)

References

1. R. Hooke, *Micrographia, or, Some Physiological Descriptions of Minute Bodies Made by Magnifying Glasses :With Observations and Inquiries Thereupon /by R. Hooke* ... (1665).
2. E. Coons, A. H. Creech, H. J., Jones, N. and Berliner, "The Demonstration of Pneumococcal Antigen in Tissues by the Use of Fluorescent Antibody," J. Immunol. **45**(3), 159–170 (1942).
3. M. Chalfie, Y. Tu, G. Euskirchen, W. Ward, and D. Prasher, "Green fluorescent protein as a marker for gene expression," Science (80-.). **263**(5148), 802–805 (1994).
4. M. Minsky, "Microscopy apparatus," U.S. patent US003013467 (1961).
5. Leica-Microsystems, "Leica HyD | Photon Counter | Hybrid Detector - Product: Leica Microsystems," https://www.leica-microsystems.com/products/confocal-microscopes/details/product/leica-hyd/.
6. S. W. Hell and J. Wichmann, "Breaking the diffraction resolution limit by stimulated emission: stimulated-emission-depletion fluorescence microscopy," Opt. Lett. **19**(11), 780 (1994).
7. S. W. Hell and M. Kroug, "Ground-state-depletion fluorscence microscopy: A concept for breaking the diffraction resolution limit," Appl. Phys. B Lasers Opt. **60**(5), 495–497 (1995).
8. T. A. Klar, S. Jakobs, M. Dyba, A. Egner, and S. W. Hell, "Fluorescence microscopy with diffraction resolution barrier broken by stimulated emission.," Proc. Natl. Acad. Sci. U. S. A. **97**(15), 8206–8210 (2000).
9. X. Hao, C. Kuang, T. Wang, and X. Liu, "Effects of polarization on the de-excitation dark focal spot in STED microscopy," J. Opt. **12**(11), 115707 (2010).
10. S. W. Hell, "Microscopy and its focal switch," Nat. Methods (2009).
11. F. Curdt, S. J. Herr, T. Lutz, R. Schmidt, J. Engelhardt, S. J. Sahl, and S. W. Hell, "isoSTED nanoscopy with intrinsic beam alignment," Opt. Express **23**(24), 30891 (2015).
12. M. Dyba, S. Jakobs, and S. W. Hell, "Immunofluorescence stimulated emission depletion microscopy," Nat. Biotechnol. **21**(11), 1303–1304 (2003).
13. M. Dyba and S. W. Hell, "Focal Spots of Size λ/23 Open Up Far-Field Florescence Microscopy at 33 nm Axial Resolution," Phys. Rev. Lett. **88**(16), 163901 (2002).
14. D. Wildanger, R. Medda, L. Kastrup, and S. W. Hell, "A compact STED microscope providing 3D nanoscale resolution," J. Microsc. **236**(1), 35–43 (2009).
15. D. Wildanger, E. Rittweger, L. Kastrup, and S. W. Hell, "STED microscopy with a supercontinuum laser source," Opt. Express

16(13), 9614 (2008).
16. K. Y. Han and T. Ha, "Dual-color three-dimensional STED microscopy with a single high-repetition-rate laser," Opt. Lett. **40**(11), 2653 (2015).
17. M. Leutenegger, C. Eggeling, and S. W. Hell, "Analytical description of STED microscopy performance.," Opt. Express **18**(25), 26417–26429 (2010).
18. G. Vicidomini, G. Moneron, K. Y. Han, V. Westphal, H. Ta, M. Reuss, J. Engelhardt, C. Eggeling, and S. W. Hell, "Sharper low-power STED nanoscopy by time gating," Nat. Methods **8**(7), 571–573 (2011).
19. E. Betzig, G. H. Patterson, R. Sougrat, O. W. Lindwasser, S. Olenych, J. S. Bonifacino, M. W. Davidson, J. Lippincott-Schwartz, and H. F. Hess, "Imaging intracellular fluorescent proteins at nanometer resolution.," Science **313**(September), 1642–1645 (2006).
20. W. Moerner and L. Kador, "Optical detection and spectroscopy of single molecules in a solid," Phys. Rev. Lett. **62**(21), 2535–2538 (1989).
21. M. Lindén, V. Ćurić, E. Amselem, and J. Elf, "Pointwise error estimates in localization microscopy," Nat. Commun. **8**(May), 15115 (2017).
22. M. J. Rust, M. Bates, and X. Zhuang, "Sub-diffraction-limit imaging by stochastic optical reconstruction microscopy (STORM).," Nat. Methods **3**(10), 793–795 (2006).
23. M. Heilemann, S. Van De Linde, M. Schüttpelz, R. Kasper, B. Seefeldt, A. Mukherjee, P. Tinnefeld, and M. Sauer, "Subdiffraction-resolution fluorescence imaging with conventional fluorescent probes," Angew. Chemie - Int. Ed. **47**, 6172–6176 (2008).
24. D. Baddeley, I. D. Jayasinghe, C. Cremer, M. B. Cannell, and C. Soeller, "Light-induced dark states of organic fluochromes enable 30 nm resolution imaging in standard media," Biophys. J. **96**(2), (2009).
25. a. Loschberger, S. van de Linde, M.-C. Dabauvalle, B. Rieger, M. Heilemann, G. Krohne, and M. Sauer, "Super-resolution imaging visualizes the eightfold symmetry of gp210 proteins around the nuclear pore complex and resolves the central channel with nanometer resolution," J. Cell Sci. **125**, 570–575 (2012).
26. E. A. Mukamel, H. Babcock, and X. Zhuang, "Statistical Deconvolution for Superresolution Fluorescence Microscopy," Biophys. J. **102**(10), 2391–2400 (2012).
27. R. Heintzmann and C. G. Cremer, "Laterally modulated excitation microscopy: Improvement of resolution by using a diffraction grating," in I. J. Bigio, H. Schneckenburger, J. Slavik, K. Svanberg, and P. M. Viallet, eds. (1999), pp. 185–196.
28. M. G. Gustafsson, "Surpassing the lateral resolution limit by a factor of two using structured illumination microscopy.," J. Microsc. **198**(January), 82–87 (2000).
29. E. Mudry, K. Belkebir, J. Girard, J. Savatier, E. Le Moal, C. Nicoletti, M. Allain, and A. Sentenac, "Structured illumination microscopy using unknown speckle patterns," Nat. Photonics **6**(5), 312–315 (2012).

30. S. S. N.Chakrova, B.Rieger, "Studying different illumination patterns for resolution improvement in fluorescence microscopy," Opt. Express **23**(24), 24692–24701 (2015).
31. B. Bailey, D. L. Farkas, D. L. Taylor, and F. Lanni, "Enhancement of axial resolution in fluorescence microscopy by standing-wave excitation," Nature (1993).
32. M. G. L. Gustafsson, L. Shao, P. M. Carlton, C. J. R. Wang, I. N. Golubovskaya, W. Z. Cande, D. A. Agard, and J. W. Sedat, "Three-dimensional resolution doubling in wide-field fluorescence microscopy by structured illumination," Biophys. J. **94**(12), 4957–4970 (2008).
33. M. G. L. Gustafsson, "Nonlinear structured-illumination microscopy: wide-field fluorescence imaging with theoretically unlimited resolution.," Proc. Natl. Acad. Sci. U. S. A. **102**(37), 13081–13086 (2005).
34. F. Wei, D. Lu, H. Shen, W. Wan, J. L. Ponsetto, E. Huang, and Z. Liu, "Wide field super-resolution surface imaging through plasmonic structured illumination microscopy," Nano Lett. (2014).
35. A. Gur, Z. Zalevsky, V. Micó, J. García, and D. Fixler, "The limitations of nonlinear fluorescence effect in super resolution saturated structured illumination microscopy system," in *Journal of Fluorescence* (2011), **21**(3), pp. 1075–1082.
36. Y. Hirano, A. Matsuda, and Y. Hiraoka, "Recent advancements in structured-illumination microscopy toward live-cell imaging," Microscopy **64**(4), 237–249 (2015).
37. E. N. Ward and R. Pal, "Image scanning microscopy: an overview," J. Microsc. **266**(2), 221–228 (2017).
38. C. B. Müller and J. Enderlein, "Image scanning microscopy," Phys. Rev. Lett. **104**(19), 1–4 (2010).
39. C. J. R. Sheppard, "Super-resolution in confocal imaging," Optik (Stuttg). **80**(2), 53–54 (1988).
40. C. J. R. Sheppard, S. B. Mehta, and R. Heintzmann, "Superresolution by image scanning microscopy using pixel reassignment.," Opt. Lett. **38**(15), 2889–92 (2013).
41. A. G. York, S. H. Parekh, D. Dalle Nogare, R. S. Fischer, K. Temprine, M. Mione, A. B. Chitnis, C. a Combs, and H. Shroff, "Resolution doubling in live, multicellular organisms via multifocal structured illumination microscopy.," Nat. Methods **9**(7), 749–754 (2012).
42. J. Bewersdorf, A. Egner, and S. W. Hell, "Multifocal Multi-Photon Microscopy," in *Handbook Of Biological Confocal Microscopy* (Springer US, 2006), pp. 550–560.
43. A. Egner, V. Andresen, and S. W. Hell, "Comparison of the axial resolution of practical Nipkow-disk confocal fluorescence microscopy with that of multifocal multiphoton microscopy: Theory and experiment," J. Microsc. (2002).
44. T. Azuma and T. Kei, "Super-resolution spinning-disk confocal microscopy using optical photon reassignment," Opt. Express **23**(11), 15003 (2015).
45. N. Chakrova, B. Rieger, and S. Stallinga, "Deconvolution methods for

structured illumination microscopy," J. Opt. Soc. Am. A **33**(7), B12–B20 (2016).
46. F. Huang, T. M. P. Hartwich, F. E. Rivera-Molina, Y. Lin, W. C. Duim, J. J. Long, P. D. Uchil, J. R. Myers, M. A. Baird, W. Mothes, M. W. Davidson, D. Toomre, and J. Bewersdorf, "Video-rate nanoscopy using sCMOS camera-specific single-molecule localization algorithms," Nat. Methods (2013).
47. S. Dong, P. Nanda, R. Shiradkar, K. Guo, and G. Zheng, "High-resolution fluorescence imaging via pattern-illuminated Fourier ptychography.," Opt. Express **22**(17), 20856–70 (2014).
48. M. Guizar-Sicairos and J. R. Fienup, *Phase Retrieval with Transverse Translation Diversity: A Nonlinear Optimization Approach* (2008).
49. T. Luke?, P. K???ek, Z. ?vindrych, J. Benda, M. Ovesn?, K. Fliegel, M. Kl?ma, and G. M. Hagen, "Three-dimensional super-resolution structured illumination microscopy with maximum a posteriori probability image estimation," Opt. Express **22**(24), 29805 (2014).
50. M. Ingaramo, A. G. York, E. Hoogendoorn, M. Postma, H. Shroff, and G. H. Patterson, "Richardson-Lucy Deconvolution as a General Tool for Combining Images with Complementary Strengths," ChemPhysChem **15**(4), 794–800 (2014).
51. F. Ströhl and C. F. Kaminski, "A joint Richardson—Lucy deconvolution algorithm for the reconstruction of multifocal structured illumination microscopy data," Methods Appl. Fluoresc. **3**(1), 14002 (2015).
52. Z. Cheng, Y. Zhou, M. Xia, W. Li, K. Yang, and Y. Zhou, "Tight focusing of the azimuthally polarized light beam for a sharper spot," Opt. Laser Technol. **73**, 77–81 (2015).
53. R. Dorn, S. Quabis, and G. Leuchs, "Focusing a radially polarized light beam to a significantly smaller spot size," arXiv Prepr. physics/0310007 (November 2003), 4 (2003).
54. R. Dorn, S. Quabis, and G. Leuchs, "Sharper Focus for a Radially Polarized Light Beam," Phys. Rev. Lett. **91**(23), 233901 (2003).
55. G. Wu, "Propagation properties of a radially polarized partially coherent twisted beam in free space," J. Opt. Soc. Am. A **33**(3), 345 (2016).
56. M. Soskind, R. Soskind, and Y. G. Soskind, "Producing superresolved point-spread functions using a phase modulation technique," in G. G. Gregory and R. J. Koshel, eds. (2010), **7787**, p. 77870T.
57. T. Mu, Z. Chen, S. Pacheco, R. Wu, C. Zhang, and R. Liang, "Generation of a controllable multifocal array from a modulated azimuthally polarized beam," Opt. Lett. **41**(2), 261 (2016).
58. Z. S. Hegedus and V. Sarafis, "Superresolving filters in confocally scanned imaging systems," J. Opt. Soc. Am. A **3**(11), 1892–1896 (1986).
59. F. K. Fatemi, S. E. Olson, M. Bashkansky, Z. Dutton, and M. Terraciano, "Single-beam, dark toroidal optical traps for cold atoms," Proc. SPIE **6483**, 648307 (2007).
60. M. Prasciolu, F. Tamburini, G. Anzolin, E. Mari, M. Melli, A. Carpentiero, C. Barbieri, and F. Romanato, "Fabrication of a three-

dimensional optical vortices phase mask for astronomy by means of electron-beam lithography," Microelectron. Eng. (2009).
61. Y. Shechtman, L. E. Weiss, A. S. Backer, S. J. Sahl, and W. E. Moerner, "Precise 3D scan-free multiple-particle tracking over large axial ranges with Tetrapod point spread functions," Nano Lett. 150505043713001 (2015).
62. S. R. P. Pavani, M. A. Thompson, J. S. Biteen, S. J. Lord, N. Liu, R. J. Twieg, R. Piestun, and W. E. Moerner, "Three-dimensional, single-molecule fluorescence imaging beyond the diffraction limit by using a double-helix point spread function.," Proc. Natl. Acad. Sci. U. S. A. **106**(9), 2995–2999 (2009).
63. C. Kuang, S. Li, W. Liu, X. Hao, Z. Gu, Y. Wang, J. Ge, H. Li, and X. Liu, "Breaking the Diffraction Barrier Using Fluorescence Emission Difference Microscopy," Sci. Rep. **3**(1), 1441 (2013).
64. H. Dehez, M. Piché, and Y. De Koninck, "Resolution and contrast enhancement in laser scanning microscopy using dark beam imaging," Opt. Express **21**(13), 15912 (2013).
65. M. Born and E. Wolf, *Principles of Optics: Electromagnetic Theory of Propagation, Interference* (1999).
66. D. Sage, L. Donati, F. Soulez, D. Fortun, G. Schmit, A. Seitz, R. Guiet, C. Vonesch, and M. Unser, "DeconvolutionLab2: An open-source software for deconvolution microscopy," Methods **115**, 28–41 (2017).
67. R. P. J. Nieuwenhuizen, K. A. Lidke, M. Bates, D. L. Puig, D. Grünwald, S. Stallinga, and B. Rieger, "Measuring image resolution in optical nanoscopy," Nat. Methods **10**(6), 557–562 (2013).
68. G. Tortarolo, M. Castello, A. Diaspro, S. Koho, and G. Vicidomini, "Evaluating image resolution in stimulated emission depletion microscopy," (n.d.).
69. A. Ashkin, "Acceleration and Trapping of Particles by Radiation Pressure," Phys. Rev. Lett. **24**(4), 156–159 (1970).
70. A. Ashkin and J. Dziedzic, "Optical trapping and manipulation of viruses and bacteria," Science (80-.). **235**(4795), 1517–1520 (1987).
71. A. Ashkin, "Forces of a single-beam gradient laser trap on a dielectric sphere in the ray optics regime," Biophys. J. **61**(2), 569–582 (1992).
72. A. Ashkin, J. M. Dziedzic, and T. Yamane, "Optical trapping and manipulation of single cells using infrared laser beams," Nature **330**(6150), 769–771 (1987).
73. P. Shinde, L. Mohan, A. Kumar, K. Dey, A. Maddi, A. Patananan, F.-G. Tseng, H.-Y. Chang, M. Nagai, and T. Santra, "Current Trends of Microfluidic Single-Cell Technologies," Int. J. Mol. Sci. **19**(10), 3143 (2018).
74. F. M. Fazal and S. M. Block, "Optical tweezers study life under tension," Nat. Photonics **5**(6), 318–321 (2011).
75. K. Visscher, G. J. Brakenhoff, and J. J. Krol, "Micromanipulation by “multiple” optical traps created by a single fast scanning trap integrated with the bilateral confocal scanning laser microscope," Cytometry **14**(2), 105–114 (1993).
76. K. Visscher, S. P. Gross, and S. M. Block, "Construction of multiple-beam optical traps with nanometer-resolution position sensing,"

IEEE J. Sel. Top. Quantum Electron. **2**(4), 1066–1076 (1996).
77. G. J. Brouhard, H. T. Schek, and A. J. Hunt, "Advanced optical tweezers for the study of cellular and molecular biomechanics," IEEE Trans. Biomed. Eng. **50**(1), 121–125 (2003).
78. J. E. Molloy, J. E. Burns, J. Kendrick-Jones, R. T. Tregear, and D. C. S. White, "Movement and force produced by a single myosin head," Nature **378**(6553), 209–212 (1995).
79. J. Leach, G. Sinclair, P. Jordan, J. Courtial, M. Padgett, J. Cooper, and Z. Laczik, "3D manipulation of particles into crystal structures using holographic optical tweezers.," Opt Express **12**(1), 220–226 (2004).
80. R. Di Leonardo, F. Ianni, and G. Ruocco, "Computer generation of optimal holograms for optical trap arrays," Opt. Express **15**(4), 1913 (2007).
81. K. D. Wulff, D. G. Cole, R. L. Clark, R. DiLeonardo, J. Leach, J. Cooper, G. Gibson, and M. J. Padgett, "Aberration correction in holographic optical tweezers," Opt. Express **14**(9), 4169 (2006).
82. H. He, M. E. J. Friese, N. R. Heckenberg, and H. Rubinsztein-Dunlop, "Direct Observation of Transfer of Angular Momentum to Absorptive Particles from a Laser Beam with a Phase Singularity," Phys. Rev. Lett. **75**(5), 826–829 (1995).
83. M. Reicherter, T. Haist, E. U. Wagemann, and H. J. Tiziani, "Optical particle trapping with computer-generated holograms written on a liquid-crystal display," Opt. Lett. (1999).
84. J. Liesener, M. Reicherter, T. Haist, and H. J. Tiziani, "Multi-functional optical tweezers using computer-generated holograms," Opt. Commun. (2000).
85. K. Bahlmann, P. T. C. So, M. Kirber, R. Reich, B. Kosicki, W. McGonagle, and K. Bellve, "Multifocal multiphoton microscopy (MMM) at a frame rate beyond 600 Hz," Opt. Express (2007).
86. L. Sacconi, E. Froner, R. Antolini, M. R. Taghizadeh, A. Choudhury, and F. S. Pavone, "Multiphoton multifocal microscopy exploiting a diffractive optical element," Opt. Lett. (2003).
87. J. E. Curtis, C. H. J. Schmitz, and J. P. Spatz, "Symmetry dependence of holograms for optical trapping," Opt. Lett. **30**(16), 2086 (2005).
88. G. Sinclair, P. Jordan, J. Courtial, M. Padgett, J. Cooper, and Z. J. Laczik, "Assembly of 3-dimensional structures using programmable holographic optical tweezers," Opt. Express **12**(22), 5475 (2004).
89. R. W. Gerchberg and W. O. Saxton, "Phase determination from image and diffraction plane pictures in the electron microscope," Optik (Stuttg). **34**(3), 275–284 (1971).
90. J. W. Goodman, *Introduction to Fourier Optics, Third Edition* (Roberts and Company, 2004).
91. C. Hesseling, M. Woerdemann, A. Hermerschmidt, and C. Denz, "Controlling ghost traps in holographic optical tweezers," Opt. Lett. **36**(18), 3657 (2011).
92. M. Woerdemann, C. Alpmann, M. Esseling, and C. Denz, "Advanced optical trapping by complex beam shaping," Laser Photon. Rev. **7**(6), 839–854 (2013).

93. M. Pasienski and B. Demarco, "A high-accuracy algorithm for designing arbitrary holographic atom traps," Phys. Rev. A Phys. Rev. Lett. J.Es eve Opt. EXPRESS **4**(3), (2008).
94. S. Bianchi and R. Di Leonardo, "Real-time optical micro-manipulation using optimized holograms generated on the GPU," Comput. Phys. Commun. **181**(8), 1444–1448 (2010).
95. J. R. Fienup and C. C. Wackerman, "Phase-retrieval stagnation problems and solutions," J. Opt. Soc. Am. A **3**(11), 1897 (1986).
96. P. Senthilkumaran, F. Wyrowski, and H. Schimmel, "Vortex Stagnation problem in iterative Fourier transform algorithms," Opt. Lasers Eng. **43**, 43–56 (2005).
97. H. Lin, B. Jia, and M. Gu, "Dynamic generation of Debye diffraction-limited multifocal arrays for direct laser printing nanofabrication," Opt. Lett. **36**(3), 406 (2011).
98. S. HELL, G. REINER, C. CREMER, and E. H. K. STELZER, "Aberrations in confocal fluorescence microscopy induced by mismatches in refractive index," J. Microsc. (1993).
99. J. Antonello, D. Burke, and M. J. Booth, "Aberrations in stimulated emission depletion (STED) microscopy," Opt. Commun. (2017).
100. S. Deng, L. Liu, Y. Cheng, R. Li, and Z. Xu, "Effects of primary aberrations on the fluorescence depletion patterns of STED microscopy," Opt. Express **18**(2), 1657 (2010).
101. M. Arigovindan, J. W. Sedat, and D. A. Agard, "Effect of depth dependent spherical aberrations in 3D structured illumination microscopy," Opt. Express **20**(6), 6527 (2012).
102. M. Born and E. Wolf, "Principles of optics," Univ. Press. Cambridge (2011).
103. Q. Mu, Z. Cao, L. Hu, D. Li, and L. Xuan, "An adaptive optics imaging system based on a high-resolution liquid crystal on silicon device," Opt. Express (2006).
104. J. D. Schmidt, M. E. Goda, and B. D. Duncan, "Aberration production using a high-resolution liquid-crystal spatial light modulator.," Appl. Opt. (2007).
105. G. Vdovin, O. Soloviev, A. Samokhin, and M. Loktev, "Correction of low order aberrations using continuous deformable mirrors," Opt. Express (2008).
106. S. Bonora, I. Capraro, L. Poletto, M. Romanin, C. Trestino, and P. Villoresi, "Wave front active control by a digital-signal-processor-driven deformable membrane mirror," Rev. Sci. Instrum. (2006).
107. A. J. Wright, B. a Patterson, S. P. Poland, J. M. Girkin, G. M. Gibson, and M. J. Padgett, "Dynamic closed-loop system for focus tracking using a spatial light modulator and a deformable membrane mirror.," Opt. Express (2006).
108. J. M. Girkin, S. Poland, and A. J. Wright, "Adaptive optics for deeper imaging of biological samples," Curr. Opin. Biotechnol. (2009).
109. R. Heintzmann, Q. S. Hanley, D. Arndt-Jovin, and T. M. Jovin, "A dual path programmable array microscope (PAM): Simultaneous acquisition of conjugate and non-conjugate images," J. Microsc. **204**(2), 119–135 (2001).

110. M. Zheng, Q. Wang, Y. Teng, X. Wang, F. Wang, T. Chen, J. Samaj, J. Lin, and D. C. Logan, "The speed of mitochondrial movement is regulated by the cytoskeleton and myosin in Picea wilsonii pollen tubes.," Planta **231**(4), 779–791 (2010).
111. A. D. Edelstein, M. A. Tsuchida, N. Amodaj, H. Pinkard, R. D. Vale, and N. Stuurman, "Advanced methods of microscope control using μManager software," J. Biol. Methods **1**(2), e10 (2014).
112. A. Klauss, F. Conrad, and C. Hille, "Binary phase masks for easy system alignment and basic aberration sensing with spatial light modulators in STED microscopy," (n.d.).
113. E. N. Ward and R. PAL, "Holographic projection for multi-spot structured illumination microscope," J. Mirosc. **Accepted m**, (2019).
114. R. W. Bowman, G. M. Gibson, A. Linnenberger, D. B. Phillips, J. A. Grieve, D. M. Carberry, S. Serati, M. J. Miles, and M. J. Padgett, "“Red Tweezers”: Fast, customisable hologram generation for optical tweezers," Comput. Phys. Commun. **185**(1), 268–273 (2014).
115. E. Nehme, L. E. Weiss, T. Michaeli, and Y. Shechtman, "Deep-STORM: super-resolution single-molecule microscopy by deep learning," Optica **5**(4), 458 (2018).
116. R. F. Laine, G. Gemma, L. J. Young, T. Jon, C. Danielle, D. Oliver, B. Helen, van der Walle Christopher, and C. F. Kaminski, "MiLeSIM: combining super-resolution and machine learning permits high-throughput virus structure analysis," bioRxiv (2018).
117. B. Harke, C. K. Ullal, J. Keller, and S. W. Hell, "Three-Dimensional Nanoscopy of Colloidal Crystals," Nano Lett. **8**(5), 1309–1313 (2008).
118. G. Zhao, Z. Rong, C. Kuang, C. Zheng, and X. Liu, "3D fluorescence emission difference microscopy based on spatial light modulator," J. Innov. Opt. Health Sci. **09**(03), 1641003 (2016).
119. Nobel Media, "Liquid Crystals," http://www.nobelprize.org/educational/physics/liquid_crystals/history/.